DANISH METEOROLOGICAL INSTITUTE

SCIENTIFIC REPORT

00-06

Polar Stratospheric Clouds

Microphysical and optical models

By

Niels Larsen

DMI

COPENHAGEN 2000

Polar Stratospheric Clouds
Microphysical and optical models

Author: Niels Larsen

Scientific Report 00-06

ISBN: 87-7478-411-0
ISSN: 0905-3263
ISSN: 1399-1949 (online)

Danish Meteorological Institute

Danish Meteorological Institute,
Ministry of Transport
Lyngbyvej 100,
DK-2100 Copenhagen Ø,
Denmark

Phone: +45 39 15 75 00
Fax: +45 39 27 10 80
www.dmi.dk

Contents

1. Introduction.

The microphysical model from the Danish Meteorological Institute calculates the time dependent polar stratospheric cloud (PSC) particle size distributions and chemical compositions together with changes in gas phase mixing ratios of water vapor (H_2O) and nitric acid vapor (HNO_3), assuming an initial size distribution of background sulfate aerosols. The model simulates the formation, growth, evaporation, and sedimentation of type 1b PSC particles (supercooled ternary solution, STS); type 1a PSC particles (assumed to be composed of nitric acid trihydrate, NAT), type 2 PSC ice particles, and frozen sulfate aerosol particles, assumed to be composed of sulfuric acid tetrahydrate (SAT). The model applies the basic vapor diffusion equation to calculate the exchange of mass between the gas and condensed phase during particle growth and evaporation. The model comprehends a number of possible pathways for phase changes and the formation of solid type PSC particles. This includes the calculation of homogeneous freezing rates of ice in STS particles to form solid type 2 PSC particles a few K below the ice frost point. The model also allows for heterogeneous nucleation of pre-activated SAT for the formation of type 1a PSC NAT particles in addition to deliquescence of SAT particles during cooling below the STS threshold temperatures and SAT melting at higher stratospheric temperatures. The model is written as an atmospheric box model, facilitating a coupling to chemical transport models, photochemical trajectory models, and optical models.

The associated optical model calculates aerosol volume backscatter coefficients and extinction coefficients at specified wavelengths in the visible and near-infrared, applying Mie scattering theory and using the particles size distributions as calculated by the microphysical model. Composition-dependent refractive indices of sulfuric acid and supercooled ternary solution particles are used for the optical calculations.

This report gives a short overview of the nature of PSC particles and their role for stratospheric ozone depletion in polar regions (chapter 2). Then follows a detailed description of the applied microphysical theory (chapter 3) and a description of the structure of the microphysical simulation models (chapter 4). The associated optical model for calculation of aerosol backscatter and extinction coefficients is described in chapter 5. A number of examples of PSC simulations and an overview of previous usage of the microphysical model are given in chapter 6, followed by a description of the Fortran90 subroutines and computer programs in chapter 7. A list of principal symbols and physical constants is provided in the Appendix.

Acknowledgments.

This work has been performed within the EU projects “Multi-instrument Investigation of Polar Stratospheric Cloud Formation and Heterogeneous Chemistry Involved in Stratospheric ozone Depletion” (POSTCODE, contract ENV4-CT97-0541, 1998-2000) and “Modelling of the impact on ozone and other chemical compounds in the atmosphere from airplane emissions” (AEROCHEM II, contract ENV4-CT97-0621, 1998-2000), funded by the European Commission Environment and Climate programme (4^{th} Framework programme).

Dr. Azadeh Tabazadeh is gratefully acknowledged for useful discussions and for the provision of computer code for calculation of STS equilibrium compositions. Likewise Dr. K. Carslaw, Dr. U. Krieger, and Dr. A. Tsias are gratefully acknowledged for provision of computer codes for calculation of chemical compositions and refractive indices of STS particles and for temperature histories and PSC simulation results of observed PSC particles.

2. The role of PSC in polar ozone depletion.

Heterogeneous chemistry.

It has been recognized for several years that polar stratospheric clouds (PSC) play a key role for strong chemical ozone depletion during late winter and early spring in both polar regions [*WMO,* 1995, 1999]. The influence of the stratospheric particles on ozone depletions is two-fold: **1)** the aerosol and cloud particles provide the surfaces where fast heterogeneous chemical reactions convert inactive halogen reservoir species into potentially ozone-destroying radicals, and **2)** the cloud particles are composed of nitric acid and water; gravitational sedimentation of the particles may lead to a vertical redistribution of these species with irreversible denitrification and dehydration in the altitude range where the particles form, prolonging chemical ozone destruction by reactive chlorine.

The most important heterogeneous chemical reactions in relation to PSC particles [e.g. *Solomon*, 1999] comprise

$$\begin{aligned} ClONO_2 + HCl &\rightarrow Cl_2 + HNO_3 \\ ClONO_2 + H_2O &\rightarrow HOCl + HNO_3 \\ HOCl + HCl &\rightarrow Cl_2 + H_2O \\ BrONO_2 + HCl &\rightarrow BrCl + HNO_3 \\ BrONO_2 + H_2O &\rightarrow HOBr + HNO_3 \\ HOBr + HCl &\rightarrow BrCl + H_2O \end{aligned} \qquad (2.1)$$

and

$$N_2O_5 + H_2O \rightarrow 2\ HNO_3 \qquad (2.2)$$

Photolysis of the products in the first group of reactions (2.1) lead to a release of halogen atoms (Cl, Br) from their reservoir forms ($ClONO_2$, HCl, and $BrONO_2$). The reactive halogen species enter catalytic photochemical ozone destroying cycles in the lower polar stratosphere such as

$$\begin{array}{ll} 2\ (Cl + O_3 \rightarrow ClO + O_2) & Cl + O_3 \rightarrow ClO + O_2 \\ ClO + ClO + M \rightarrow Cl_2O_2 + M & Br + O_3 \rightarrow BrO + O_2 \\ Cl_2O_2 + h\nu \rightarrow Cl + ClO_2 & BrO + ClO \rightarrow Br + ClO_2 \\ \underline{ClO_2 + M \rightarrow Cl + O_2 + M} & \underline{ClO_2 + M \rightarrow Cl + O_2 + M} \\ \underline{\text{net: } 2\ O_3 \rightarrow 3\ O_2} & \underline{\text{net: } 2\ O_3 \rightarrow 3\ O_2} \end{array} \qquad (2.3)$$

These catalytic cycles can only proceed if the concentration of NO_2 is low since the reaction

$$NO_2 + ClO \rightarrow ClONO_2 \qquad (2.4)$$

would transfer the reactive chlorine back to the reservoir form (also the reaction $Cl+CH_4 \rightarrow HCl+CH_3$ transfers Cl, more slowly, back to the reservoir form).

Nitric acid (HNO_3) is the dominant member of the reactive nitrogen family $NO_y=\{HNO_3+NO+NO_2+NO_3+2(N_2O_5)+HO_2NO_2\}$ in the lower stratosphere. Interactions among these species include

$$\begin{aligned} HNO_3 + h\nu &\rightarrow OH + NO_2 \\ HNO_3 + OH &\rightarrow NO_3 + H_2O \end{aligned} \qquad (2.5)$$

where NO_2 is generated and

$$NO_2+NO_3+M \rightarrow N_2O_5+M \qquad (2.6)$$

Dinitrogen pentoxide (N_2O_5) will photolyze in daylight back to NO_2 and NO_3, but may also interact heterogeneously as indicated in the last of the above heterogeneous reactions (2.2).

The condensation of HNO_3 to form the PSC particles implies a lower concentration of reactive nitrogen NO_y and thereby, due to (2.5), to a lower concentration of NO_2 in the gas phase (denoxification). The role of reaction (2.4) to deactivate chlorine would thereby be reduced and the lifetime of reactive chlorine would be prolonged. If the PSC particles, containing HNO_3, fall to lower altitudes an irreversible removal of reactive nitrogen may take place (denitrification) which may prolong the catalytic ozone depletion reactions. At temperatures below the ice frost point, gravitational sedimentation of relatively large type 2 PSC ice particles may also lead to a vertical redistribution of water and dehydration on the layer where the particles form.

The rate of the heterogeneous reactions depend strongly on temperature and the chemical composition and physical phase of the particles as shown for the first of the above heterogeneous reactions (2.1) in Figure 2.1.

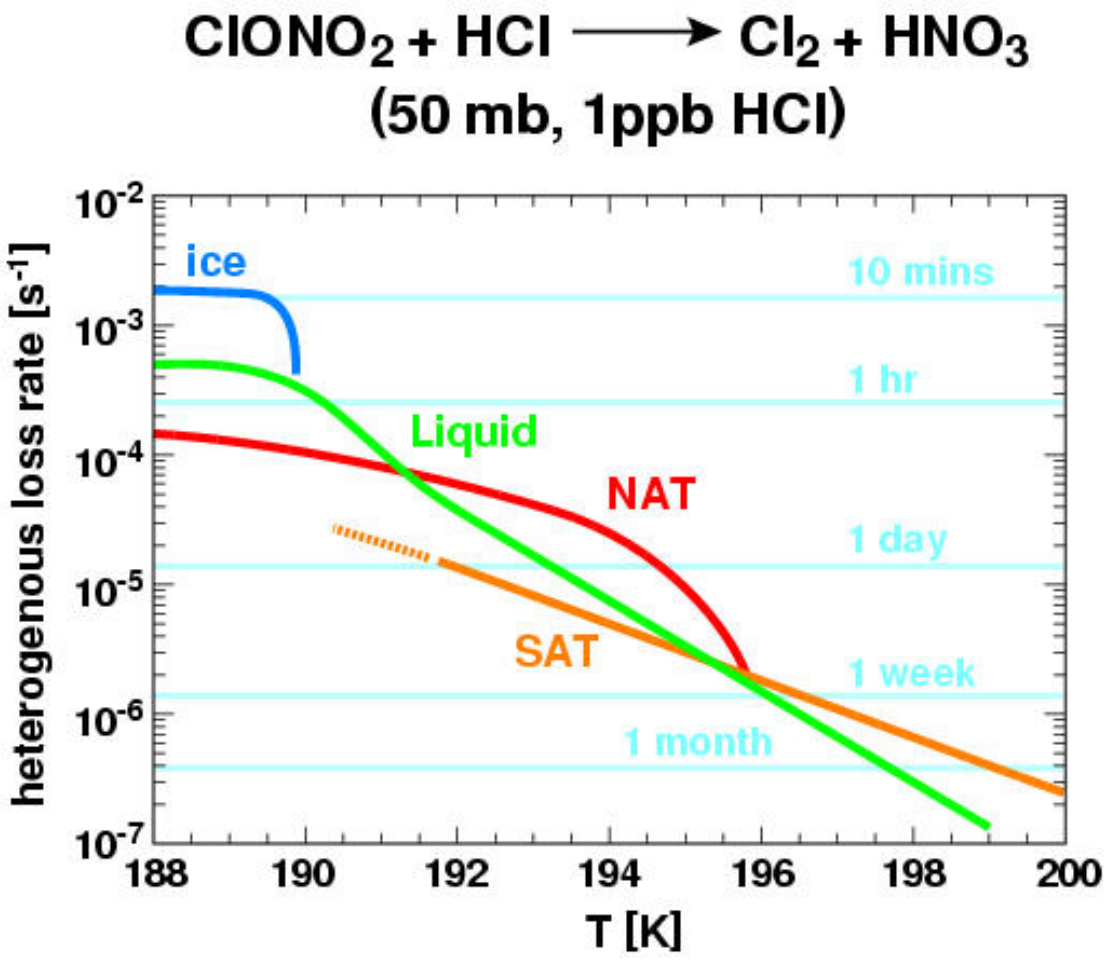

Figure 2.1. Rate of an important heterogeneous chlorine activating reaction, plotted as function of temperature, for liquid (Type 1b), solid (Type 1a NAT and Type 2 ice) PSC particles, and frozen sulfuric acid tetrahydrate (SAT) aerosol particles. The horizontal lines indicate the lifetime of the reaction partners. *Adapted from Carslaw et al*. [1999b]; *courtesy K. Carslaw.*

Stratospheric particles.

In addition to the ubiquitous stratospheric sulfate aerosols, early satellite observations showed that cloud particles form in both polar stratospheres at very low temperatures. Groundbased and airborne lidar backscatter and depolarization measurements have been used to classify the stratospheric particles of relevance for the ozone depletion [e.g. *WMO*, 1999], cf. Figure 2.2 and 2.3. Two types of PSCs forming respectively above (type 1) and below (type 2) the ice frost point temperature (T_{ice}) were originally identified [*Poole and McCormick*, 1988]. The former type was later subdivided into lidar depolarizing (presumably solid) type 1a PSCs (blue symbols in Figure 2.2 and 2.3) and non-depolarizing (liquid) type 1b PSCs (red symbols in Figure 2.2 and 2.3).

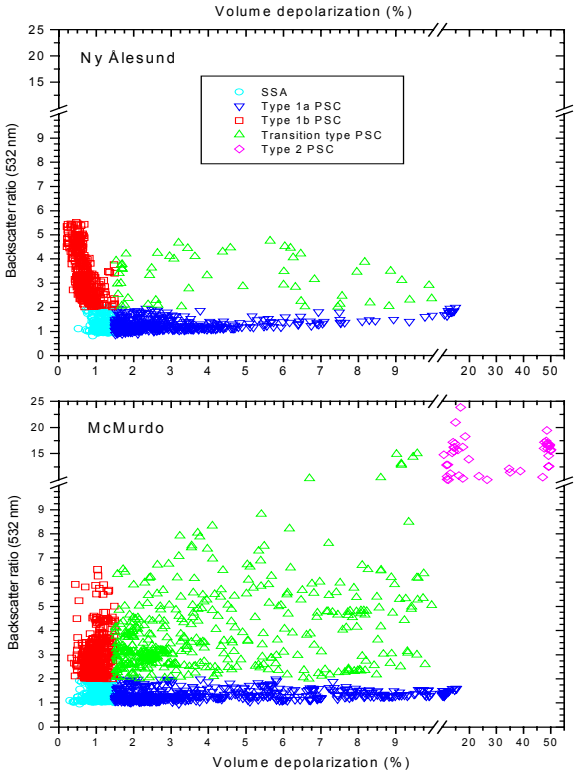

Figure 2.2. Classical categorization of PSC and stratospheric sulfate aerosol particles, based on lidar backscatter and depolarization measurements from Ny Ålesund and McMurdo. *Adapted from WMO*[1999]*; courtesy R. Neuber and A. Adriani.*

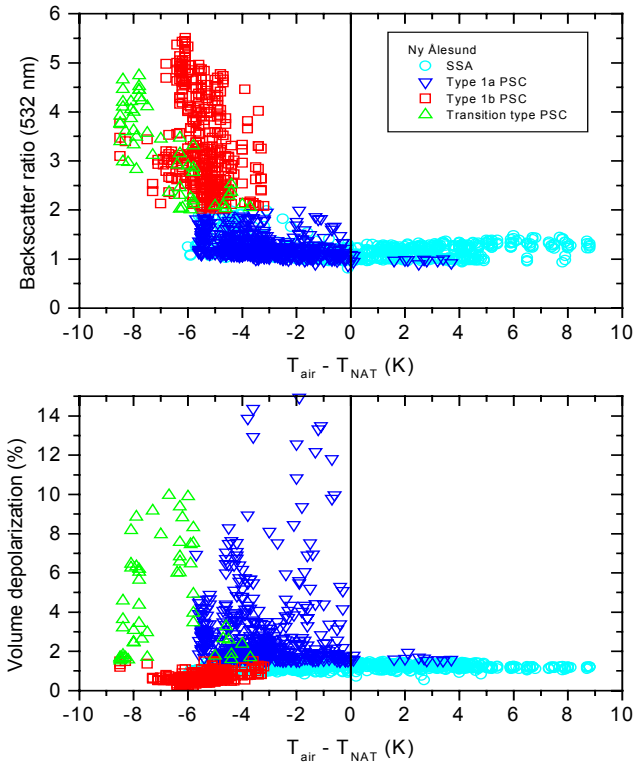

Figure 2.3. The same Arctic aerosol and PSC measurements as in Figure 2.2, plotted against the difference between the air temperature and T_{NAT}. *Adapted from WMO*[1999].

Whereas type 2 PSCs (magenta symbols in Figure 2.2) are composed of water ice particles, it was originally suggested that type 1 PSCs were composed of nitric acid trihydrate (NAT) which is stable at the stratospheric conditions [*Hanson and Mauersberger*, 1988]. However, some type 1 PSCs were observed in the Arctic at high supersaturations with respect to NAT. Airborne particle volume measurements later showed an excellent agreement with models, assuming the particles to be composed of liquid supercooled ternary solutions (STS; $HNO_3/H_2SO_4/H_2O$) [*Tabazadeh et al.*, 1994; *Carslaw et al.*, 1994]. Various lidar observations and airborne and balloonborne measurements are consistent with the description of type 1b PSCs as being composed of STS particles. The composition and, in particular, the formation

of solid type PSCs and their northern hemisphere implications are much more uncertain and has been in focus of European and US research in recent years. Thorough reviews of past stratospheric aerosol and PSC research, leading up to the current level of understanding, have been given, e.g. by *Fiocco et al.* [1997], *Peter* [1997], *Carslaw et al.* [1997], and *WMO* [1999, chapter 3].

The current "standard" picture of stratospheric particles of relevance for ozone depletion comprises the liquid and solid-phase sulfate aerosols and Type 1a, 1b, and 2 PSCs. However, there are observations of so-called transition type PSCs (green symbols in Figure 2.2); this name being given to those particles since they could be of a mestastable solid-phase composition or being observed under non-equilibrium conditions, both indicating a possible transition to a more stable configuration. This will be discussed in more detail below.

Looking first at the "standard" particles, the liquid type 1b PSCs show a compact relationship between e.g. lidar backscatter ratio and temperature (red symbols in Figure 2.3) indicating that the particles undergo a rapid increase in volume at temperatures roughly 4 K below the NAT existence temperature (T_{NAT}), turning into fully developed type 1b PSC slightly above the ice frost point temperature. This is in good agreement with in predictions from the STS equilibrium model as shown in Figure 2.4. The type 1a PSCs are observed at all temperatures below T_{NAT} (blue symbols in Figure 2.3), and at least part of these particles are likely composed of NAT.

Considering possible trends of decreasing temperature and increasing water vapor in the polar stratosphere, it is worth noting that PSCs form in a very narrow temperature range, mainly depending on the water vapor concentrations. Figure 2.4 shows the temperature growth range, assuming variations of ±20% in H_2O and HNO_3 concentrations.

The two temperature-axes in the lower part of Figure 2.4 gives a rough indication at which temperature intervals, relative to T_{NAT} and T_{ice}, that different "standard" type particles could exist. At decreasing temperature the liquid sulfate aerosols will gradually take up nitric acid and water, turning into type 1b PSCs. Extensive laboratory and theoretical investigations have shown that the liquid particles will freeze into ice only at temperatures 3-4 K below T_{ice} [*Koop et al*., 1997a, 1998; *Chang et al.* 1999; *MacKenzie et al.,* 1998]. Once frozen into type 2 PSC ice particles, nitric acid could nucleate into NAT by vapor deposition on these particles. At temperatures above T_{ice} the ice would evaporate, leaving behind type 1a PSC NAT residual particles, which could exist at temperatures below T_{NAT}. At higher temperatures a sulfate remnant in the solid particles could be composed of sulfuric acid tetrahydrate (SAT) which would melt at temperatures above roughly 216 K [*Middlebrook et al.*, 1993]. Many details about the phase transitions are unknown and will be discussed in more detail below. However, it is important to note the temperature hysteresis in the phase transition cycles which require that the temperature history of the particles must be known to give a realistic microphysical simulation of the particle formation, complicating parameterisations of PSC occurrence in larger atmospheric chemistry models.

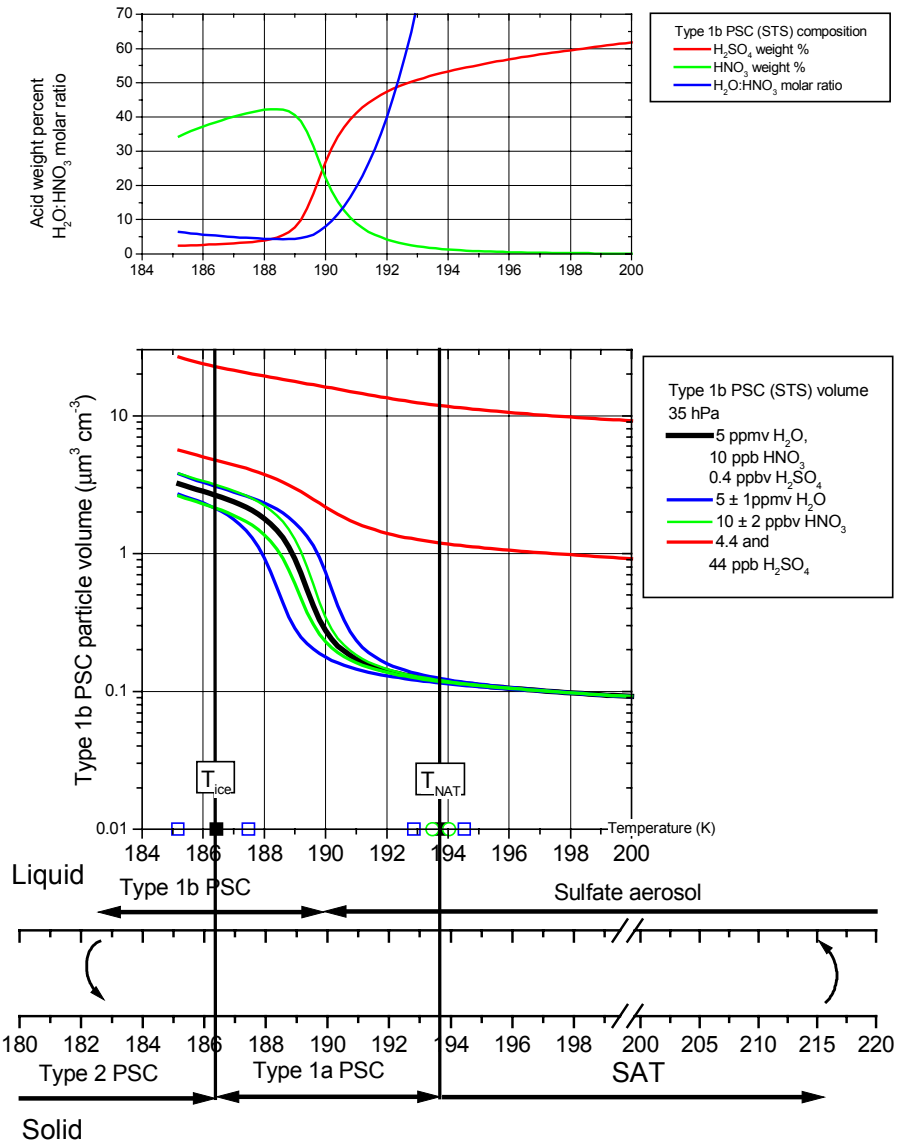

Figure 2.4 Type 1b PSC (STS) particle equilibrium chemical composition (upper panel) and volume (lower panel), calculated as function of temperature [*Carslaw et al.,* 1995] at 35 hPa, assuming 5 ppmv H_2O, 10 ppbv HNO_3, and 0.4 ppbv H_2SO_4 (black curve). The upper panel shows how the chemical composition continuously changes from a nearly binary H_2SO_4 solution through a ternary composition into a nearly binary HNO_3 solution at decreasing temperatures. In the lower panel, the blue curves indicate the volume range assuming 5±1 ppmv H_2O and the green curves assuming 10±2 ppbv HNO_3. The two red curves indicate the particle volumes, assuming 10 and 100 times increase in H_2SO_4, typical for volcanic conditions. T_{NAT} and T_{ice} are indicated on the temperature axis with the H_2O-variation range (blue square symbols) and the HNO_3-variation range (green circle symbols). The temperature axes in the lower part indicate the temperature existence range of different stratospheric particle types, showing the temperature hysteresis with freezing of liquid particles 3-4 K below T_{ice} and melting around 216 K.

The phase transitions are important, both because the heterogeneous reaction rates depend on the chemical composition of the particles (Figure 2.1), and perhaps more importantly because only solid particles could induce a denitrification which may prolong the chemical ozone de-

struction. Growth of type 1b PSCs implies a distribution of the available nitric acid on all particles. In order to obtain a significant fall speed, the available nitric acid must condense on a relatively small number of solid-phase particles for these to grow to sufficient sizes and only type 2 or type 1a PSC could be responsible for denitrification. The question of PSC phase changes is particularly important in the Arctic stratosphere where synoptic minimum temperatures typically hover around the PSC thresholds (Figure 2.4), and complicated phase transitions could take place in individual air parcels. Synoptic temperatures rarely drop below T_{ice} and mesoscale temperature fluctuations may therefore have a more important hemispheric influence here, compared to the SH. The Arctic interannual temperature variability will also introduce a large variability in PSC properties. Only occasionally has denitrification been observed in the Arctic stratosphere in contrast to Antarctica where a nearly complete and regular denitrification takes place each year in the lower stratosphere inside the polar vortex, pointing out the strong influence of lower temperatures on PSC properties and the influence on the gas phase.

Shindell et al. [1998], using a global climate model with simplified ozone chemistry, have predicted that increased concentrations of greenhouse gases may lead to a more stable Arctic vortex with less frequent warmings, 5-10 K lower stratospheric temperatures and increased ozone depletion. *Waibel et al.* [1999] went one step further investigating the effects of denitrification on ozone depletion, both in a recent cold Arctic winter (1994-95) and in a future stratospheric climate with lower temperatures. The applied microphysical model assumes that NAT condenses on a small number of ice particles, which form by freezing of type 1b PSCs at 1.5 K below T_{ice}. Using daily meteorological temperature data to simulate the PSC formation and calculating particle sedimentation in a 3D-transport scheme, it was possible to reproduce the observed denitrification in the 1994-95 winter. Assuming the calculated loss of HNO_3 inside the vortex throughout March, it was possible by a photochemical model also to reproduce the observed ozone depletion, revealing 55% more ozone loss in air parcels with the simulated denitrification around 19 km altitude. The investigations show that the Arctic denitrification is highly sensitive to temperature changes. Reducing the Arctic vortex temperatures by 5 K, predicted to occur in a doubled CO_2 climate, leads to removal of more than 80% of the available NO_y. The simulations show that reducing the inorganic chlorine concentrations to prescribed year-2070-conditions (comparable to 1980) will result in nearly the same ozone depletion as in winter 1994-95, indicating that enhanced denitrification will delay the recovery of the Arctic ozone until late in the 21st century.

Solid type PSC formation and phase transitions.

Microphysical details about the solid type PSC formation have been revealed from airborne lidar measurements in strong mountain leewave events over northern Scandinavia [*Carslaw et al*., 1998; *Wirth et al*., 1999]. By flying nearly parallel to the wind direction over the mountains, quasi-Lagrangian pictures of the evolution in particle formation have been obtained. These “natural laboratory experiments” have shown that essentially all liquid particles, which have formed upwind of the mountains, freeze directly into ice when the air parcels are cooled adiabatically to temperatures at least 3-4 K below the ice frost point. In the subsequent heating most of the particles return to the liquid state. However, some of the observations have shown that by following the airparcels several (hundred) kilometers downwind of the locations where the ice particles formed, a tail of solid particles emerges out of the liquid particles which are left behind after the ice evaporation.

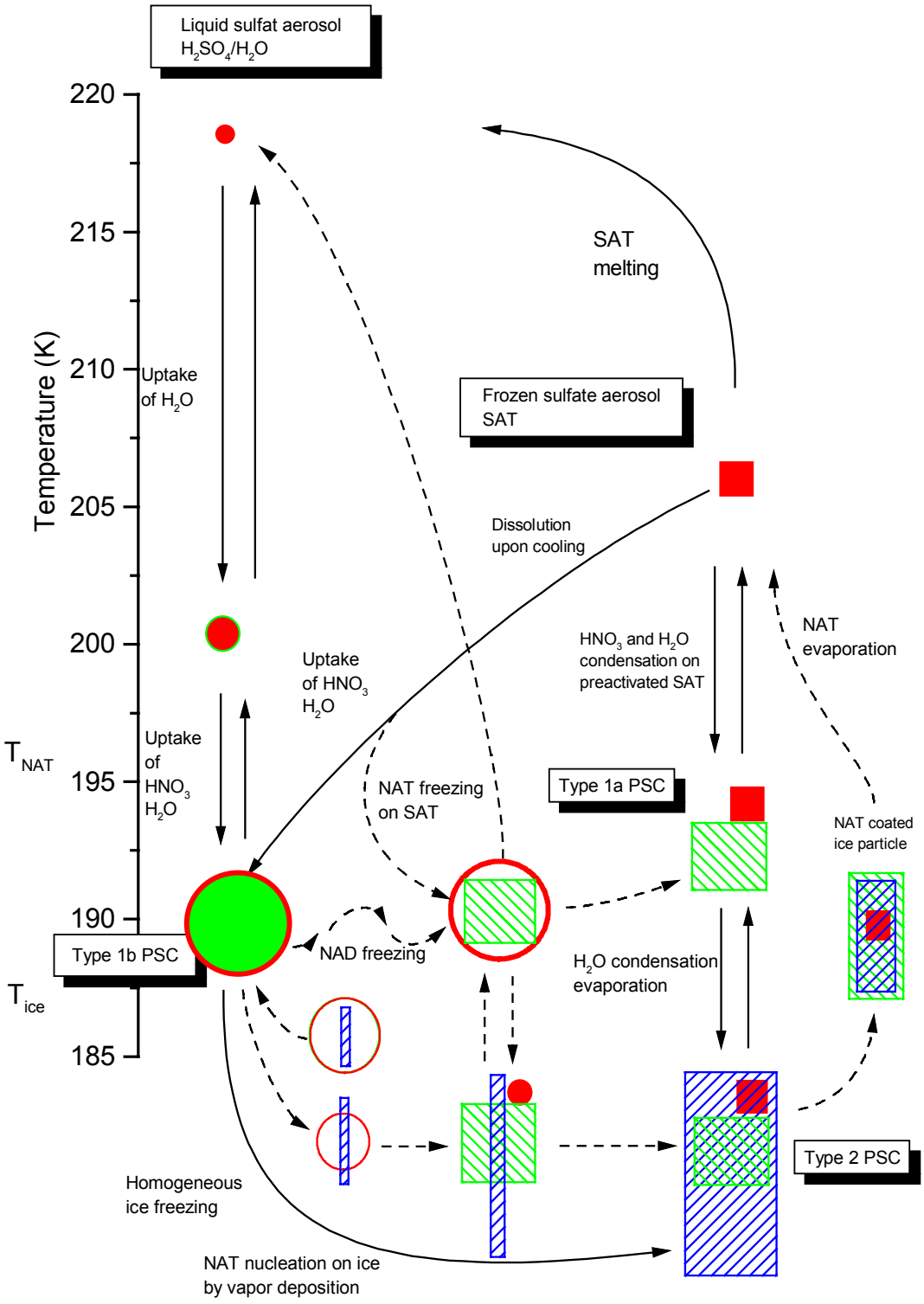

Figure 2.5. Schematic illustration of possible phase transitions between liquid (left-hand side) and solid particles (see text for further explanations). Liquid phases are symbolized by circles, solid phase by boxes. NAT is indicated by green \\\ hatching, ice by blue /// hatching, and SAT by red boxes. Particle sizes not to scale. Boxes with shadows and solid arrows indicate those particle types and processes, respectively, which are included in the present microphysical simulation model.

Apparently the ice particles have induced the formation of a number of nitric acid dihydrate (NAD) or trihydrate particles. The observations show that the presence of liquid type PSCs and the cooling rate prior to the ice formation may have an influence on the number of ice particles serving as sites for hydrate particle formation and how long downwind that hydrate particles emerge. If the air is cooled at high rates (≈70 K h^{-1}) from temperatures above PSC conditions, the particles may not have time to grow significantly and ice will form in relatively small particles and a large fraction of these particles (60%) may serve as sites for nitric acid hydrate nucleation. The solid type 1 PSCs will then appear at short distances from the ice formation region. The situation is different if type 1b PSC have formed prior to the freezing or during more slowly cooling. Then ice will form in larger particles and only a smaller fraction (2%) of the smallest particles will be suited for hydrate nucleation, showing up as type 1a PSCs at much larger distances away from where the ice particles form. *Tsias et al.* [1999] analyzed airborne lidar measurements east of Greenland of a rare solid type PSC, characterized by relatively high backscatter ratios that fall outside the usual type 1a PSC classification. These observations could be explained by assuming that a relative large fraction (50%) of ice particles serve as sites for NAT nucleation in contrast to a much lower fraction to explain the usual type 1a PSCs.

In Figure 2.5 various pathways for phase changes between liquid and solid particles, to be consistent with the observations, will be discussed [cf. *Koop et al*., 1997b; *Carslaw et al.*, 1999a]. Liquid particles, shown in the left-hand side of Figure 2.5, will take up HNO_3 and H_2O at decreasing temperatures, turning into STS type 1b PSC particles, and ice will eventually freeze out 3-4 K below the ice frost point.

Laboratory experiments [*Koop et al.,* 1997a] have shown that NAT and SAT are unlikely to freeze heterogeneously from the ternary liquid surrounding the ice enclosure and these particles might turn into liquid particles after ice evaporation in a subsequent heating. On the other hand, if the surface of the STS film breaks and the ice surface becomes exposed to the gas phase in some of (the smaller) particles, nucleation of NAT by vapor deposition from the gas phase could take place (this may provide a selective nucleation mechanism whereby a small number of relatively large NAT particles may form). It is unclear if the remaining STS solution would freeze into SAT and NAT at this point. This detailed freezing scenario remains to be confirmed from laboratory experiments although some airborne lidar observations of freezing processes in mountain leewaves [*Carslaw et al*., 1998; *Wirth et al*., 1999] could be explained by these freezing assumptions as discussed below.

Other freezing experiments on micron sized binary (H_2SO_4/H_2O) and ternary solution particles [*Koop et al.,* 1998; *Chang et al.,* 1999] have been used to constrain thermodynamic properties (mainly the diffusion activation free energy of water molecules across the ice/solution phase boundary) to be used by classical homogeneous freezing theory to describe the liquid-to-solid phase transition [*Tabazadeh et al*., 1997a, b; 2000]. This theory, which has been applied in the present microphysical model and which will be described in more detail in chapter 3, implies that freezing will be proportional to the particle volume. Freezing will start among the largest particles in the size distribution. Since the freezing rate depends strongly on the water partial pressure, the first formed particles will take up water vapor by condensation and may prevent the smallest particles in the size distribution to freeze.

If temperatures are kept below T_{NAT} a slow (hours to days) transfer of nitric acid will take place from remaining STS liquid particles and liquid film to the solid particles. Below the ice frostpoint type 2 PSC ice particles will form by condensation of both water vapor and HNO_3 on the solid particles. At temperatures above T_{ice} ice will evaporate, leaving behind a type 1a PSC, and eventually NAT will evaporate above T_{NAT}, turning the remaining sulfate particle into a liquid aerosol (this pathway not included in the present model) or a frozen SAT particle that will melt above ≈ 216 K. However, if SAT particles are cooled again, and HNO_3 now remains in the gas phase, thermodynamical model calculations [*Koop and Carslaw*, 1996] have shown that SAT will be unstable and start melting, taking up HNO_3 and H_2O to form ternary solution droplets. During this process NAT may nucleate from the liquid on not-completely dissolved SAT [*Iraci et al.,* 1998], again forming a type 1a PSC particle above the ice frost point. Although SAT has been shown not to be efficient for NAT nucleation by vapor deposition [*MacKenzie et al*., 1995, *Iraci et al.,* 1995], laboratory experiments have shown that SAT, onto which NAT has previously been deposited (pre-activated SAT), has a larger ability for NAT nucleation [*Zhang et al.,* 1996], providing an alternative way to generate type 1a PSC particles above T_{ice}. Presumably it would be difficult from field measurements to discriminate between these two pathways, and only the pre-activated-SAT-pathway or complete dissolution of the SAT particle into a STS particles are included in the present model.

It has been suggested that type 2 PSC ice particles may obtain a coating of NAT that could prevent or slow-down the ice evaporation (this process is not included in the present microphysical model). The prolonged lifetime of large particles with a significant fall speed would provide a mechanism for vertical transport of nitric acid. The NAT coating might form if ice particles fall to lower altitudes into warmer layers with supersaturation with respect to NAT [*Wofsy et al.,* 1990a] or in mountain leewaves when solid particles, composed of ice and NAT, preferentially evaporate the ice leaving behind a NAT coating [*Peter et al.*, 1994]. There has been some observational evidence for the existence of NAT coated ice particles [*Goodman et al.,* 1997]. Laboratory measurements seem to indicate an uncertainty whether the NAT coating would reduce the ice evaporation [*Biermann et al.,* 1998; *Warshawsky et al*., 1999]. However, it is speculated that NAT nucleation on ice that breaks the STS film (cf. Figure 2.5 and the above mentioned freezing mechanism) may cause the whole STS film to crystallize thereby forming a more efficient (less porous) NAT coating of the ice particle [*Biermann et al.,* 1998].

Microphysical simulations of the growth and evaporation of STS type 1b PSC particles in strong mesoscale temperature fluctuations show that only the smallest particles in the size distribution will obtain equilibrium with the gas phase due to slow diffusion of HNO_3 during condensation onto the larger particles [*Meilinger et al*., 1995]. In particular during subsequent fast heating (≈150 K h^{-1}) from temperatures slightly above T_{ice}, the smallest particles may shortly turn into nearly binary nitric acid solutions with HNO_3 weight fractions greater than 58% (2.5:1 H_2O:HNO_3 molar ratio) which may favor a homogeneous freezing into (metastable) NAD [*Tsias et al*., 1997; *Prenni et al*., 1998]. Whether this selective nucleation mechanism, which may operate at temperatures above T_{ice}, has a significant influence in the real atmosphere remains to be investigated. The present microphysical model will simulate the non-equilibrium behavior of the larger particles and the size dependent particle composition; however, the NAD freezing mechanism in not included.

PSC particle volume measurements, obtained during the American AASE 1 campaign 1989, were used to verify the STS model description of type 1b PSC [*Carslaw et al*., 1994; *Taba-*

zadeh et al., 1994]. However, other measurements obtained during this campaign do not show the compact volume-temperature relationship as predicted by the STS model. Some of the measurements were interpreted as being non-equilibrium NAT particles that had insufficient time to grow to full equilibrium sizes [*Peter*, 1997]. Measurements from other days in the same campaign were interpreted as particles being composed of a metastable water-rich HNO_3/H_2O solid phase with a relatively high vapor pressure, compared to NAT [*Tabazadeh and Toon*, 1996]. It was speculated that a few of the metastable particles might transform into stable NAT and grow by slow vapor transfer from remaining metastable particles, thereby providing a selective mechanism for generating a few large solid type 1a PSC particles.

It is quite obvious from the airborne lidar measurements that PSC formation processes in mountain leewaves, where temperature drop below the ice frost point, may lead to a selective nucleation of type 1a PSC particles [*Carslaw et al*., 1998; *Wirth et al*., 1999]. These particles may survive for a long time if temperatures subsequently remain below T_{NAT}. Many observations of PSCs, also on synoptic scales outside typical mountain leewave regions, show the presence of type 1a PSCs. According to the above discussed nucleation mechanisms, temperatures below T_{ice} are required for the formation of solid type PSCs; a constrain which is not very often met by synoptic temperatures in the Arctic. Statistical analyses of synoptic temperature histories have indicated that type 1a PSC particles have experienced longer periods at temperatures below T_{NAT}, compared to type 1b PSCs, but not necessarily experienced synoptic temperatures below T_{ice} [*Larsen et al.,* 1997]. However, this may also imply a larger probability that the solid particles have actually been processed in mesoscale temperature fluctuations. An important scientific question therefore remains to what extend the mountain waves are responsible for the solid particle formation on hemispheric scales in the Arctic. *Carslaw et al.* [1999a] have addressed this question using domain-filling trajectory calculations coupled with a model to describe mountain wave temperature perturbations, showing that indeed the mountains in the Arctic regions could be sources of type 1a PSCs on synoptic scales. These calculations show for the period December 1994 to January 1995 that 1-14% of the air parcels inside the polar vortex (4-60% of the air parcels with temperature below T_{NAT}) on the 475 K isentropic surface might contain type 1a PSC particles formed in leewaves. By including SAT formation and the two associated pathways for NAT formation above T_{ice}, the simulations show a steady increase during winter in airparcels containing SAT particles (up to 40%) and a significant increase in type 1a PSC occurrence.

Observations of SAT particles would be valuable to assess if these particles play a role for additional NAT particles formation and possibly to discriminate between the two suggested pathways (SAT dissolution, or NAT condensation on pre-activated SAT). No climatology has been presented for solid type sulfate aerosol and it is striking that only very few observations exist which have been associated with SAT particles. *Beyerle et al.* [1999] have performed a thorough investigation of groundbased lidar observations from Spitsbergen in winters 1994/95-1998/99, looking for depolarizing stratospheric aerosol that exist at temperatures above T_{NAT}. Although it is demonstrated that the depolarization measurements should be very sensitive to the occurrence of frozen aerosol particles, only four observational cases of solid phase aerosols have actually been identified. It is not clear if this could be taken as a signature of the unlikely formation of SAT particles; on the other hand airparcel temperatures histories of the investigated cases are not inconsistent with the above-suggested freezing mechanisms.

Chemical and optical properties of PSC particles.

The exact chemical composition of PSC particles has been measured [*Schreiner et al.*, 1999] by combined balloonborne mass spectrometer and optical backscatter measurements in weak leewaves over northern Scandinavia. Inside the PSCs these measurements clearly showed enhanced particle-related water and nitric acid signals with H_2O:HNO_3 molar ratios above 10, excluding NAD or NAT compositions of the particles. The particle compositions could be in agreement with predictions of an STS composition [*Schreiner et al.*, 1999]. However, if composed of STS the very dilute chemical compositions indicate that the particle volumes should be relatively small which seems to be in disagreement with the simultaneous optical measurements that seem to indicate a fully developed type 1b PSC [*Larsen et al.*, 2000]. Similar disagreements have been noted in lidar measurements of type 1b PSCs [*Shibata et al.,* 1997]. Cryogenic aerosol chamber experiments are in progress to study the PSC formation processes. In these laboratory experiments, the formation of PSC particles in leewave situations can be simulated, following the chemical composition of the condensed phase in the particles by utilizing the same instrumentation as in the balloonborne experiments, and in addition measuring the gas phase composition together with physical properties and freezing of the particles.

Refractive indices of PSC particle compositions are needed to interpret remote optical measurements of the particles. Theoretical estimates and laboratory measurements of the refractive indices of STS have been presented by *Luo et al.* [1996] and *Krieger et al.* [2000]. *Deshler et al.* [2000] derived refractive indices of PSC particles by combined measurements of size distributions and optical backscatter, revealing an unexpected discrepancy between these measurements and the predicted values for STS particles based on theoretical and laboratory work.

Outstanding issues.

Based on the above discussion a number of outstanding issues can be identified which are needed to be investigated in order to constrain microphysical PSC modeling:

- Measurements of the chemical composition of PSC particles under different meteorological conditions.
- Thermodynamical quantities to calculate homogeneous freezing rates of ice in STS solution droplets; advanced aerosol freezing experiments are currently addressing those issues.
- Better assessments of the role of SAT in processes to generate type 1a PSC particles and if SAT particles actually exist in the atmosphere.
- Observations to assess if freezing into NAD take place in fast temperature oscillations above T_{ice} in the atmosphere.
- Observations to assess if metastable dilute solid solution particles play a role in the formation of type 1a PSC in the atmosphere.
- Laboratory measurements of the refractive indices of various potential PSC compositions.
- New methods to include more a detailed (interactive) simulation of PSC formation and denitrification in larger atmospheric chemistry models.
- Analyses to assess the temporal and geographical scales of PSC formation.
- Further analyses to assess the role of mesoscale and synoptic scale PSC formation processes in different arctic winters, looking for possible tendencies toward Antarctic-resembling conditions.

Various microphysical models have been used to address these issues [*Carslaw et al.*, 1997, 1998; *Drdla and Turco,* 1991; *Drdla* 1996; *Hamill et al.,* 1988, 1996; *Larsen* 1991, 1994; *Meilinger et al.,* 1995; *Panegrossi et al*., 1996; *Peter et al.,* 1991; *Peter* 1997; *Poole,* 1987; *Rizi et al.,* 1999; *Tabazadeh et al.*, 1994; *Toon et al.,* 1989; *Tsias et al.,* 1997, 1999; *Turco et al.,* 1989; *Waibel et al.*, 1999; *Wofsy et al.,* 1990a,b].

The present microphysical PSC model applies basic classical cloud physics processes and thermodynamic properties, and it is flexible both for updated thermodynamic functions and revised pathways for phase changes, derived from comparison with results from laboratory experiments and field observations.

3. **Microphysical processes.**

Several microphysical processes must be considered when modeling the evolution of an ensemble of PSC particles. These processes include:

- *homogeneous freezing* of supercooled solution droplets
- *nucleation* by HNO_3 vapor deposition on pre-activated SAT or H_2O vapor deposition on NAT
- *melting* upon heating, or *dissolution* upon cooling of solid SAT particles
- growth and shrink of liquid STS and solid NAT and ice particles by *condensation* and *evaporation* of vapor
- gravitational *sedimentation*

Solid arrows in Figure 2.5 show those processes comprehended by the present model in addition to sedimentation. Coagulation among stratospheric aerosol and PSC particles is a very slow process [*Larsen,* 1991] and will not be considered in the model. The purpose of this chapter is to indicate the theory used here in modeling the PSC behavior and to present some modeling results of basic microphysical calculations under typical atmospheric conditions where PSC particles form, and to illustrate the very different time scales of various processes. For a thorough general presentation of the cloud physics is referred to the monograph by *Pruppacher and Klett* [1997].

Vapor pressures.

Both the nucleation and condensation processes require that the saturation ratio S of the condensing vapor is greater than unity, whereas already existing particles evaporate, when S is less than unity. The saturation ratio of a specific vapor is defined as

$$S = \frac{P_p}{P_{sat}} \tag{3.1}$$

where P_p is the partial pressure and P_{sat} is the saturation vapor pressure of HNO_3 or H_2O over STS, NAT, or ice. The partial pressure is controlled by the removal or release of vapor during condensation or evaporation. The saturation pressure is a function of the temperature T, of radius r of the particle, for STS also of the chemical composition (HNO_3 and H_2SO_4 acid weight fractions, w_n and w_s), and for NAT also of the water vapor partial pressure ($P_{p,w}$).

The radius dependence of the saturation pressure, known as the Kelvin effect [*Pruppacher and Klett*, 1997, cp. 6] which raises the saturation pressure for the smaller particles, is expressed as

$$P_{sat,r} = P_{sat}(T, w, P_{p,w}) \exp\left(\frac{2M\sigma}{RT\rho r}\right) \tag{3.2}$$

Here, σ is the surface tension, and ρ the density of the condensed substance, M is the molar mass of the vapor, R is the universal gas constant, and $P_{sat}(T,w_s,w_n,P_{p,w})$ is the saturation pressure over a plane surface of condensed material. Thus, a certain supersaturation is required to keep the smaller particles in equilibrium with the vapor phase. In Figure 3.1 is shown the exponential term of the Kelvin expression.

The radiative heating or cooling of the particles will induce small temperature differences between the air and the particles. When the air temperature is used to calculate the vapor pressures, errors

will be introduced for the larger particles. However, *Toon et al.* [1989] found that the radiative effects on the small PSC particles to be insignificant, and the process is not taken into consideration in this model.

The HNO_3 and H_2O saturation vapor pressures over supercooled ternary solution, which depend on temperature and the H_2SO_4 and HNO_3 weight fractions (w_s and w_n), are calculated from the expressions given by *Luo et al.* [1995]. The saturation pressure of HNO_3 over NAT has been calculated from the expression given by *Hanson and Mauersberger* [1988]. The saturation pressures of H_2O vapor over ice and water have been taken from *Jancso et al.* [1970] and *Tabazadeh et al.* [1997c]. Examples of these saturation pressures are shown in Figure 3.2 as functions of temperature.

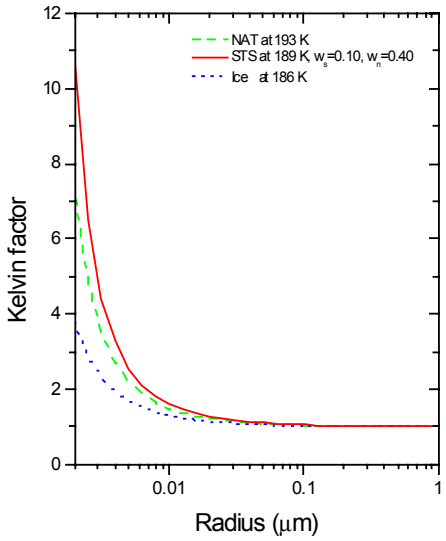

Figure 3.1 Kelvin factor, $\exp(2M\sigma/RT\rho r)$, calculated for NAT particles at 193 K, for STS at 189 K, and for ice particles at 186 K.

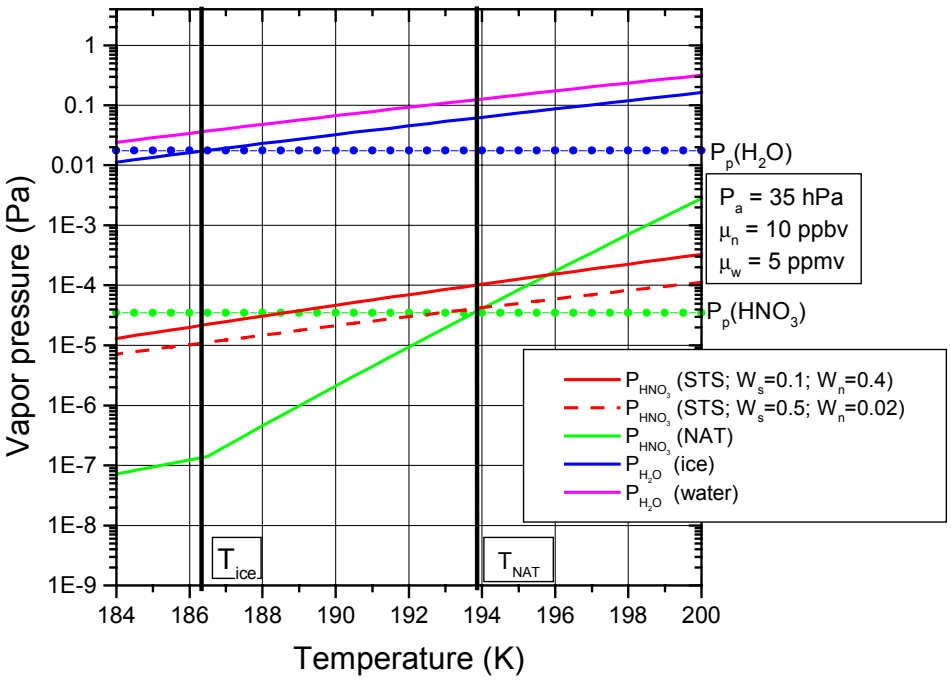

Figure 3.2 Examples of HNO_3 vapor pressures over STS (red) and NAT (green) and H_2O vapor pressures over ice (blue) and water (magenta). Partial pressures of HNO_3 and H_2O at 35 hPa at typical mixing ratios of 10 ppbv HNO_3 and 5 ppmv H_2O are indicated by green and blue dot-lines.

The two HNO_3 vapor pressures over STS are calculated with acid weight fractions (w_s = 0.5, w_n = 0.02, red dashed line) and (w_s = 0.1, w_n= 0.4, red solid line), corresponding approximately to type 1b PSC compositions at the high and low temperature existence range, respectively, cf. Figure 2.4. The saturation pressure of nitric acid over NAT (green), which depend on the water vapor pressure, is calculated in Figure 3.2 for a partial water vapor pressure of 17.5 mPa. This corresponds to a typical water vapor mixing ratio of 5 ppmv at 35 hPa, which is shown as the horizontal dotted blue line. Also a typical nitric acid partial pressure of $3.5 \cdot 10^{-5}$ Pa, corresponding to a mixing ratio of 10 ppbv at 35 hPa, is shown as the dotted green line.

The HNO_3 vapor becomes supersaturated with respect to NAT (i.e. $P_p > P_{sat}$) at the temperature where the green-dotted line lies above the green line in Figure 3.2, and likewise H_2O becomes supersaturated with respect to ice where the blue dotted line lies above the blue line. These temperatures are defined as the NAT (T_{NAT}) and ice (T_{ice}) condensation (or existence) temperatures and marked in Figure 3.2 (and Figure 2.4) by the thick vertical lines. These two important threshold temperatures depend on the pressure altitude and mixing ratios of HNO_3 and H_2O.

If liquid sulfate aerosol particles are present in the air during cooling, the HNO_3 vapor becomes supersaturated with respect to STS roughly at the temperature where the green dotted line lies above the red dashed line in Figure 3.2. HNO_3 is taken up by the STS particles at further decreasing temperatures, reducing the HNO_3 partial pressure to lie between the two red lines in Figure 3.2. This causes the particles to grow and change their composition towards a nearly binary HNO_3/H_2O solution (concurrent with H_2O uptake), see also Figure 2.4. Although the HNO_3 partial pressure is reduced, following more closely the solid red line, the vapor is highly supersaturated with respect to NAT during this process (above the green line in Figure 3.2). Therefore if NAT particles are present together with STS particles, HNO_3 will start condensing on NAT particles. This reduces the HNO_3 partial pressure to follow the green line, and the STS particles become subsaturated and start evaporating. A slow transfer of HNO_3 from STS to NAT particles could therefore take place during such conditions. Condensation of HNO_3 onto STS or NAT particles is accompanied by H_2O condensation, but since the abundance of water vapor is more than two orders of magnitude larger than nitric acid, the mixing ratio and partial pressure of H_2O are nearly not affected. If ice particles form below T_{ice} from homogeneous freezing of STS particles or from nucleation by vapor deposition on NAT particles, the water vapor becomes supersaturated with respect to ice, and the water partial pressure is reduced to follow the blue line in Figure 3.2.

The condensation (or existence) temperature is defined as the temperature where particles, composed either of NAT (T_{NAT}) or ice (T_{ice}), are in equilibrium with the HNO_3 vapor or H_2O vapor respectively. The condensation temperatures as function of air pressure (altitude) for various mixing ratios of HNO_3 and H_2O are shown in Figure 3.3. The three lower black curves in the figure are the condensation temperature for the ice particles. The upper group of colored curves shows the condensation temperature for NAT particles. Dotted curves are for H_2O=4 ppmv, solid curves for H_2O=5 ppmv, and dashed curved for H_2O=6 ppmv, red curves for HNO_3=8 ppbv, green curves for HNO_3=10 ppbv, and blue curves for HNO_3=12 ppbv. Approximate altitudes in km are indicated on the right ordinate, and temperatures in °C on the upper abscissa. As can be seen from the figure, variations of ≈20 % in the mixing ratio of either gas corresponds to slightly less that 1 K in the condensation temperatures.

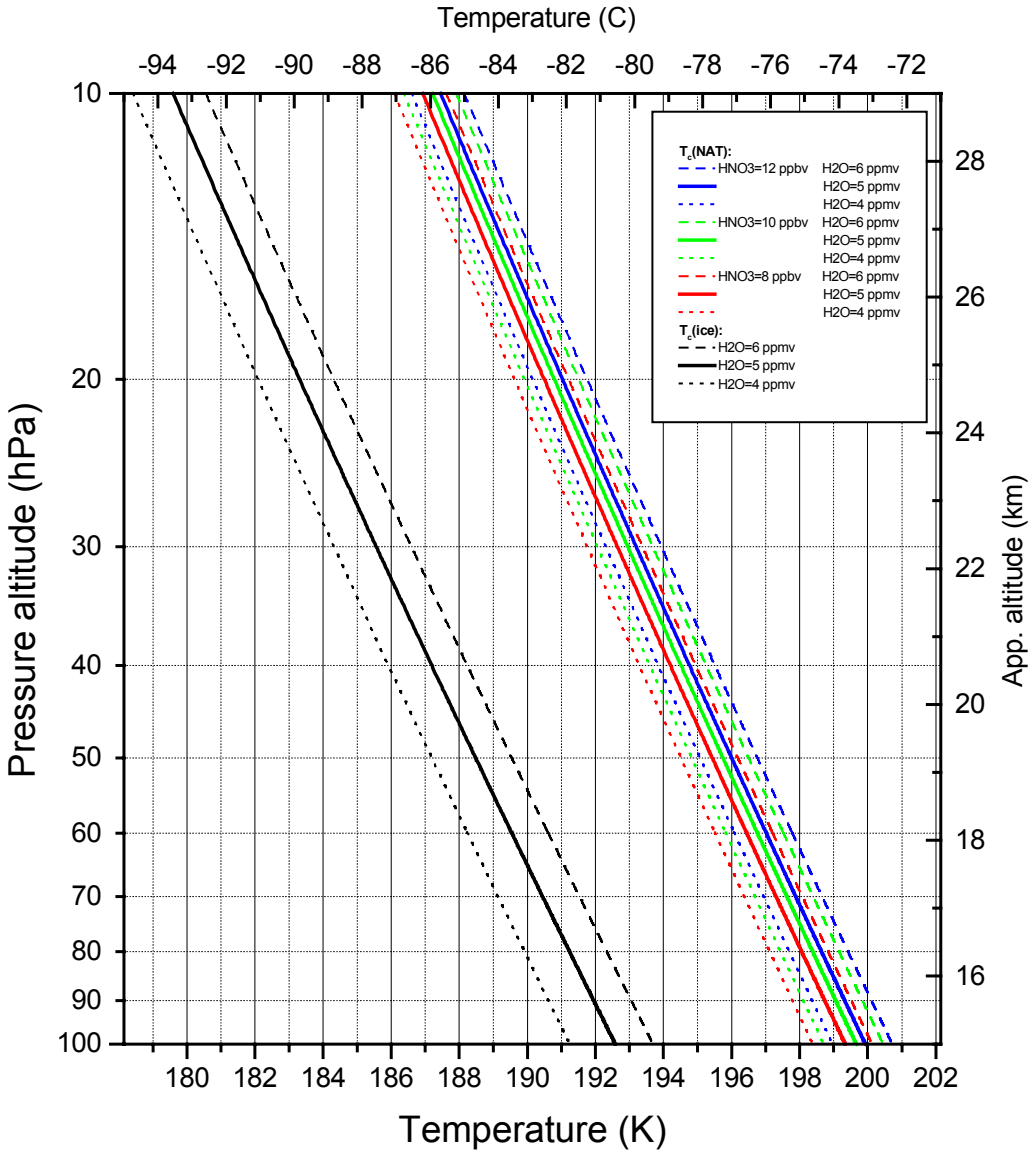

Figure 3.3 Condensation temperatures of NAT (T_{NAT}) and ice (T_{ice}), plotted as function of pressure altitude for different HNO_3 and H_2O gas phase mixing ratios. Dotted, solid, and dashed curves correspond to H_2O=4, 5, and 6 ppmv. Red, green, and blue curves to HNO_3=8, 10, and 12 ppbv. The right hand ordinate gives the approximate geometric altitude and the top abscissa the temperature in °C.

Homogeneous freezing

Classical theory of homogeneous freezing is used to calculate the freezing rates of ice in supercooled ternary solution, cf. *Pruppacher and Klett* [1997, cp. 7]. The freezing rate of a given particle will be proportional to the particle volume. Mainly four factors control the freezing rates: temperature, the H_2O partial pressure, and the assumed values of the diffusion activation energy and the surface tension between the liquid and the ice germs.

The homogeneous freezing nucleation rate (m^{-3} s^{-1}) is calculated from

$$J_f(T,w) = 2N_c\left(\frac{\rho_{sol}kT}{\rho_{ice}h}\right)\sqrt{\frac{\sigma_{sol/ice}}{kT}}\exp\left[-\frac{\Delta F_g}{kT}-\frac{\Delta F_{act}}{kT}\right] \tag{3.3}$$

where N_c is the number of water molecules in contact with a unit area of the ice surface (N_c=5.85•10^{18} m^{-2}), ρ_{sol} and ρ_{ice} are liquid STS solution and ice densities, k and h are the Boltzmann and Planck constants, ΔF_g is the free energy (per molecule) for ice germ formation, and ΔF_{act} is the diffusion activation energy of water molecules across the ice/solution phase boundary. ΔF_g is given by

$$\Delta F_g = \frac{4\pi}{3}\sigma_{sol/ice}(T,w)\,r_g{}^2 \tag{3.4}$$

where the critical germ radius, r_g, is calculated from

$$r_g = \frac{2M_w\sigma_{sol/ice}(T,w)}{\rho_{ice}\left[L_m(T)\ln\frac{T_0}{T}+½R(T+T_0)\ln a_w(T)\right]} \tag{3.5}$$

Here, M_w is the molar mass of water, L_m is the molar latent heat of ice melting, T_0 is the ice melting temperature (273.15 K), R is the universal gas constant, $\sigma_{sol/ice}$ is the surface tension between the STS solution and ice, which depends on the STS composition (w_s, w_n), and a_w is the water activity (relative humidity with respect to pure water, a_w=$P_{p,w}/P_{sat,water}$).

The surface tension $\sigma_{sul/ice}$ between STS solution and ice is calculated by applying Antonoff's rule

$$\sigma_{sul/ice}(T,w) \approx \left|\sigma_{sul/air}(T,w) - \sigma_{ice/air}\right| \tag{3.6}$$

where $\sigma_{sul/air}(T,w)$ is the surface tension between STS solution and air, and $\sigma_{ice/air}$ is the ice/air surface tension (0.105 Nm^{-1}).

The diffusion activation energy of water molecules across the ice/solution phase boundary, ΔF_{act}, is calculated from the expression given by *Tabazadeh et al.* [2000], derived from ice nucleation data from H_2SO_4/H_2O freezing experiments by *Koop et al.* [1998]. Actually, an expression would be needed for the diffusion activation energy in STS solution, which is currently not available. However, freezing experiments in binary H_2SO_4/H_2O and ternary $H_2SO_4/HNO_3/H_2O$ solution show nearly the same freezing properties, e.g. critical ice saturation or critical ice supercooling [*Koop et al.*, 1998; *Chang et al.*, 1999]. Therefore the procedure for calculating the freezing rates for binary sulfuric acid solution as outlined in *Tabazadeh et al.* [2000], (Tabazadeh, personal communication, 1999), has been adopted here, whereby the freezing rate will depend only on temperature (T) and water vapor partial pressure ($P_{p,w}$). First is calculated the equilibrium composition (w_s) that a binary sulfuric acid solution would have, corresponding to a given temperature and water vapor partial pressure [*Tabazadeh et al.,* 1997c]. This value of w_s is used to cal-

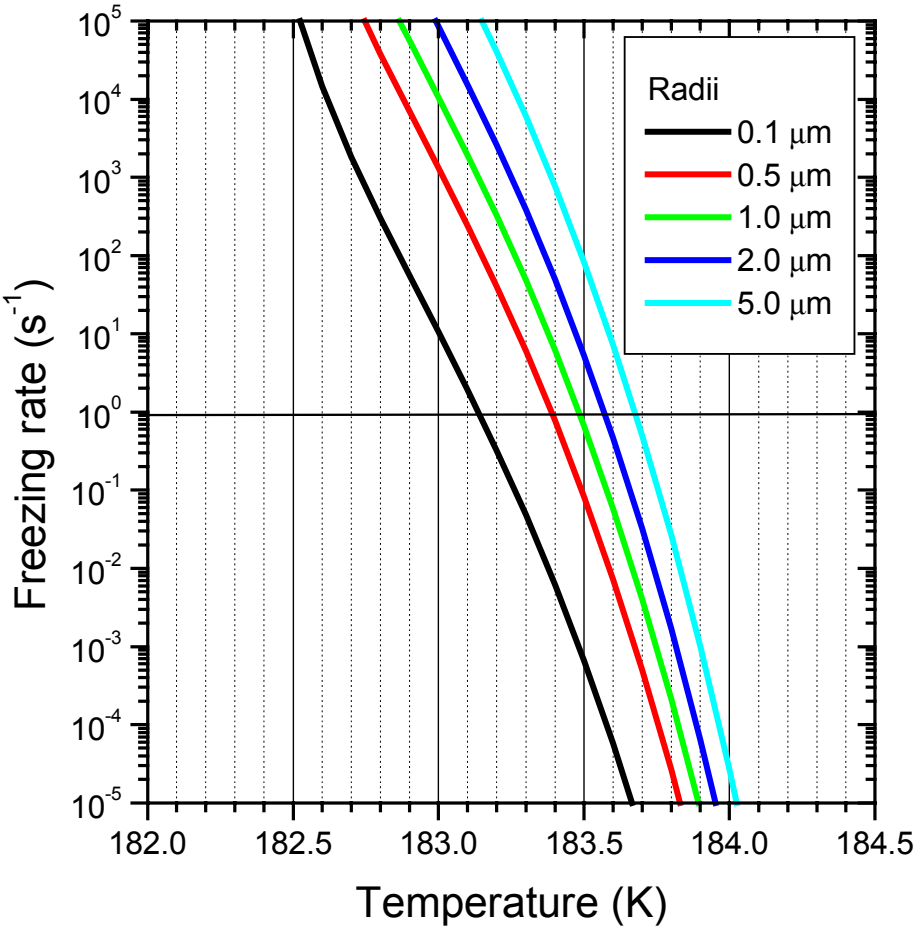

Figure 3.4 Homogeneous freezing rate, $J_f V$, calculated from (3.3) as function of temperature for different particle radii at 35 hPa pressure altitude, assuming 5 ppmv H_2O in the gas phase. The horizontal line at a freezing rate of 1 s^{-1} crossing the curves marks the critical temperatures for droplet freezing.

culate the surface tension between the binary sulfuric acid solution and ice from (3.6) and thereby the free energy for ice germ formation from (3.4) and (3.5). Combined with the value for the diffusion activation energy in binary sulfuric acid solution from the expression given by *Tabazadeh et al.* [2000], the freezing rate for the binary sulfuric acid solution at the actual ambient condition is obtained from (3.3). This value would be nearly equal to the freezing rate of the ternary solution at the same ambient conditions. However, the actual particle volume (V) of the ternary solution droplet is used to calculate if the critical condition, $J_f \cdot V > 1\ s^{-1}$, prevails and freezing into ice will actually take place in the droplet. Actually the condition, $J_f \cdot V \cdot dt > 1$, where dt is the model integration time step, specifies that more than one ice germ will form in the liquid droplet of volume V in dt seconds, whereby the whole droplet is assumed to freeze instantaneously.

Figure 3.4 shows the freezing rates, $J_f \cdot V$, for different particle radii, calculated at 35 hPa pressure altitude, assuming an H_2O gasphase mixing ratio of 5 ppmv. The figure shows the strong temperature dependence and the range of critical freezing temperatures of approximately 0.5-1 K

around 183.5 K for the different typical particle sizes. The largest particles in the size distribution will start freezing during cooling. Once frozen, water vapor will start condensing onto the first frozen particles, lowering the H_2O partial pressure and decreasing the freezing temperature furthermore for the remaining smaller liquid particles. Depending on how fast the cooling is across the critical freezing temperature range, compared to the condensation of water vapor, different fractions of the liquid particle size distribution will freeze.

In Figure 3.5 is shown the model-calculated critical supercooling and critical supersaturation ratio for particles of radius 1.25 μm (black curves). The critical supercooling is the temperature depression below the ice frost point where freezing will take place, i.e. $\Delta T=T_f-T_{ice}(P_{p,w})$, and the critical supersaturation is the saturation ratio with respect to ice at the freezing temperature, i.e. $P_{p,w}/P_{sat,ice}(T_f)$. The model results in Figure 3.5 are calculated by adjusting the water vapor partial pressure $P_{p,w}$ at each temperature value to meet the critical criterion for freezing. Comparison is made to parameterisations of the same quantities from binary HNO_3/H_2O solution (red curves) and STS aerosol freezing experiments with w_s=0.01 (green curves) and w_s=0.05 (blue curves) by *Chang et al.* [1999]. It appears that although the diffusion activation energy and surface tension of binary H_2SO_4/H_2O solution have been used to calculate the freezing rates, the difference in supercooling between the model results and parameterisations from the freezing experiments are less than 0.1 K and even smaller for the ternary solution.

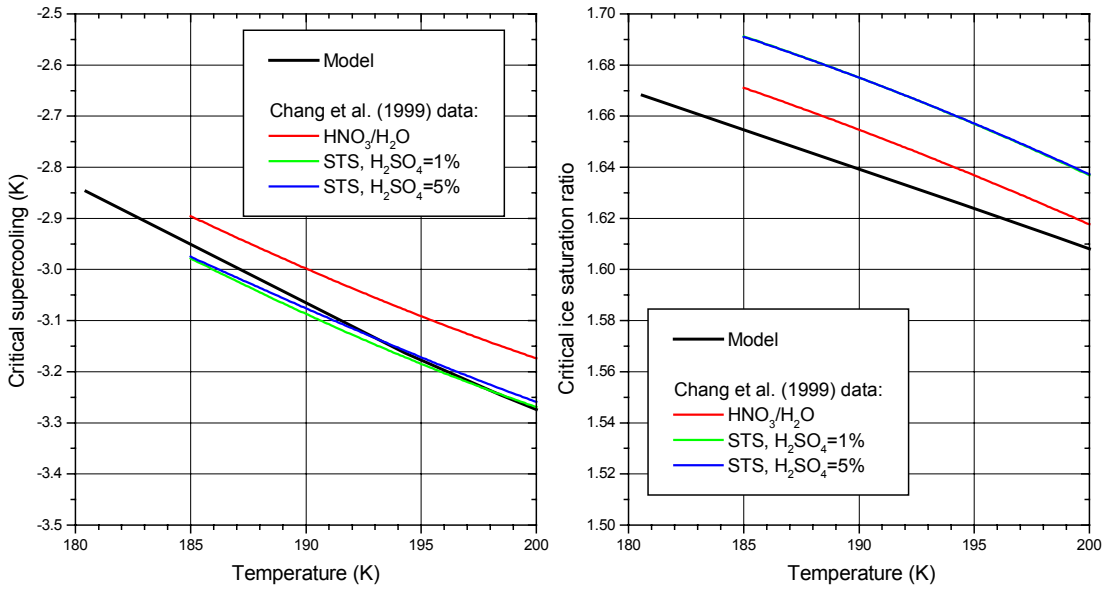

Figure 3.5 Critical supercooling below the ice frost point (left panel) and critical supersaturation with respect to ice (right panel), black curves, calculated for particle radii of 1.25 μm as functions of temperature, and compared with fits to results from freezing experiments of aerosols of the same size, composed of binary HNO_3/H_2O solution (red curves), and STS with H_2SO_4 weight fractions of 1% (green curves) and 5 % (blue curves) [*Chang et al.* 1999].

Nucleation by vapor deposition

Nucleation by vapor deposition is the process in which microscopic quantities of matter in the condensed phase (NAT or ice) are formed from the vapor phase. In the present model configuration, nucleation by HNO_3 or H_2O vapor deposition could take place when cooling SAT particles below T_{NAT}, or cooling NAT particles below T_{ice}, respectively, cf. Figure 2.5. Although theoretical and laboratory investigations have shown that SAT is not suited for NAT nucleation [*MacKenzie et al.*, 1995; *Iraci et al.*, 1995], other laboratory studies have shown that NAT may nucleate onto pre-activated SAT at a NAT-saturation ratio around 7-13 [*Zhang et al.,* 1996]. SAT particles, formed in the present model configuration, have previously been in contact with NAT, cf. Figure 2.5, and thus could be assumed to be pre-activated. The process of nucleation by HNO_3 vapor deposition will compete with the process of SAT dissolution into STS upon cooling which however will take place at a higher NAT-saturation ratio above 15 [*Koop and Carslaw*, 1996].

Adopting classical theory of *homogeneous* nucleation [*Pruppacher and Klett*, 1997, cp. 7], temperature and density fluctuations in the vapor phase above some critical supersaturation will cause molecular clusters to form in the condensed phase.

The number of clusters of a given molecular size, n_g, will follow a Boltzmann distribution, $n_g=\tilde{n}_{sat}\exp[-\Delta F/kT]$, where $\tilde{n}_{sat}$ is the molecular number density in gas phase ("single molecule cluster density), and ΔF is the free energy of cluster formation. The latter quantity consists of two components: the positive energy required to form the surface between the two phases, and the volume term, which is negative under supersaturated conditions, due to the decrease in chemical potential upon the condensation, thus ΔF can be written as

$$\Delta F = 4\pi r^2\sigma - \frac{4\pi r^3 \rho}{3 M} RT \ln(S) \tag{3.7}$$

Under supersaturated conditions this expression shows a maximum (the energy barrier for nucleation) at some critical radius, called the "germ" size, above which the energy of formation of the clusters decreases with increasing size. The germ radius r_g is given from

$$\frac{\partial \Delta F}{\partial r} = 0 \qquad r_g = \frac{2M\sigma}{RT\rho \ln(S)} \tag{3.8}$$

(consistent with the Kelvin law), and the free energy of nucleation ΔF is then given as

$$\Delta F(r_g) = \frac{4\pi}{3} r_g^{\,2} \sigma = \frac{16\pi M^2 \sigma^3}{3\left(RT\,\rho \ln(S)\right)^2} \tag{3.9}$$

The number of germs formed per unit volume per unit time during homogeneous nucleation is given as

$$J_{hom} = n_g\, w\, 4\pi r_g^2\, Z \tag{3.10}$$

where w is the flux of condensing molecules,

$$w = \frac{P_p}{4kT}\sqrt{\frac{8RT}{\pi M}} \tag{3.11}$$

and Z is the Zeldovitch factor, correcting for the effect of evaporation during the nucleation process; the latter is given from

$$Z = \frac{2Mk}{4\pi r_g^2 R\rho}\sqrt{\frac{\sigma}{kT}} \tag{3.12}$$

Nucleation ratios, calculated from the above *homogeneous* process, are too low by many orders of magnitude to account for the observed presence of PSC particles, unless supersaturation ratios will

be in the order of several hundreds in contradiction to observations. Instead, the *heterogeneous* nucleation process, in which the nucleation takes place on the surfaces of already existing particles (cloud condensation nuclei, CCN), must be considered. In this model the pre-activated SAT particles are assumed to constitute CCN for nucleation of the NAT (type 1a PSC) particles, and (the large-size part of) the PSC 1a particles again to serve as nucleation centers for type 2 PSC particles, cf. Figure 2.5.

As above, classical nucleation theory has been used to describe *heterogeneous nucleation* of both type 1a PSC and type 2 PSC particles, assuming germ growth by direct vapor deposition. The nucleation rate J, which gives the number of "germs" formed per CCN of radius r per unit time, is given from the following expression, assuming the particles to be solid and spherical [*Pruppacher and Klett*, 1997, cp. 9]

$$J(r) = C_m r^2 \frac{P_p}{kT}\sqrt{\frac{2\sigma Mk}{R\pi\rho^2}}\exp\left(\frac{-\Delta F}{kT}\right) \tag{3.13}$$

The free energy of germ formation ΔF now has to be corrected by a factor $\Im$ controlling the nucleation over a curved surface as

$$\Delta F = \frac{4\pi}{3} r_g^2 \sigma \; \Im(\mathrm{M}, x) \tag{3.14}$$

where

$$\Im(\mathrm{M}, x) = 0.5\left\{1 + \left(\frac{1 - \mathrm{M}x}{\Phi}\right)^3 + x^3\left[2 - 3\left(\frac{x - \mathrm{M}}{\Phi}\right) + \left(\frac{x - \mathrm{M}}{\Phi}\right)^3\right] + 3\mathrm{M}x^2\left(\frac{x - \mathrm{M}}{\Phi} - 1\right)\right\} \tag{3.15}$$

and

$$x = \frac{r}{r_g}; \quad \Phi = \sqrt{1 - 2\mathrm{M}x + x^2} \tag{3.16}$$

using the expression (3.8) for the germ radius r_g as above.

The value of the prefactor C_m, which accounts for the concentration of single condensing molecules adsorbed on the CCN surface, has been chosen to $C_m = 2 \cdot 10^{23}$ m^{-2}. The exponential term in the expression for J dominates, and errors in C_m have little consequence for the calculated J-values.

Using the above expression for the heterogeneous nucleation rate for a *liquid*, nucleating on a solid sphere, the 'compatibility parameter' M is equal to cosine of the contact angle between the liquid germ cap and the sphere. Here, for the nucleation into a solid material, the compatibility parameter is defined as

$$\mathrm{M} = \frac{\sigma_{ccn/air} - \sigma_{ccn/cm}}{\sigma_{cm/air}} \tag{3.17}$$

where $\sigma_{ccn/air}$, $\sigma_{ccn/cm}$, and $\sigma_{cm/air}$ are surface tensions between the CCN-particle and air, between the CCN-particle and the condensing material, and between the condensing material and air [*Pruppacher and Klett*, 1997, cp. 5 and 9]. These physical quantities have not been measured in laboratory. If M=1, then $\Im$(M=1,x)=0 and ΔF=0, and there will be no energy barrier for nucleation, except for the Kelvin effect of the smaller particles. In this case, when the saturation ratio slightly exceeds unity, nearly all CCN will be nucleated, and the newly formed particles will start a slow growth under low supersaturation ratio conditions. This is in contradiction to the laboratory experiments, at least for HNO_3 deposition on SAT [*Iraci et al.,* 1995]. On the other hand, if M is less than unity, the nucleation barrier requires a larger supersaturation ratio to result in the same nucleation rate; and once the particles are formed in these higher S-conditions, the growth will be faster for the given

cooling rate. According to laboratory experiment of NAT deposition on pre-activated SAT, saturation rations around 7-13 would be needed [*Zhang et al.,* 1996]. This would be consistent with a value of M=0.76, which has also been recommended as an upper limit by other deposition experiments [*Iraci et al.,* 1995]. *Toon et al.* [1989] performed a thorough set of computations for type 2 PSC nucleation, using M-values between 0.9 and 1.0, and recommended M=0.95 as a reasonable guess. These two M-values have been used in the present model. The nucleation rate, calculated from (3.13) and multiplied by the number of condensation nuclei, gives the rate of particle formation of the new type. In Figure 3.6 is shown the heterogeneous nucleation rates, J, for NAT (right-hand side) and ice particles (left-hand side) of different sizes, calculated at 35 hPa pressure altitude as functions of temperature. The figure shows the strong dependence of temperature and gives an indication of the temperature range where a critical nucleation rate (e.g. 1 s^{-1}) is met by particles of different sizes. The most relevant CCN sizes for NAT particle nucleation would be 0.05-0.1 µm (expected sizes of SAT particles) and 0.5-2 µm (typical sizes of type 1a PSC) for ice particle nucleation. At temperatures where a critical nucleation rate is calculated for these particles sizes, the NAT-saturation is around 8-9 and the ice saturation around 1.25-1.35 as shown by the curves with dot and triangle symbols.

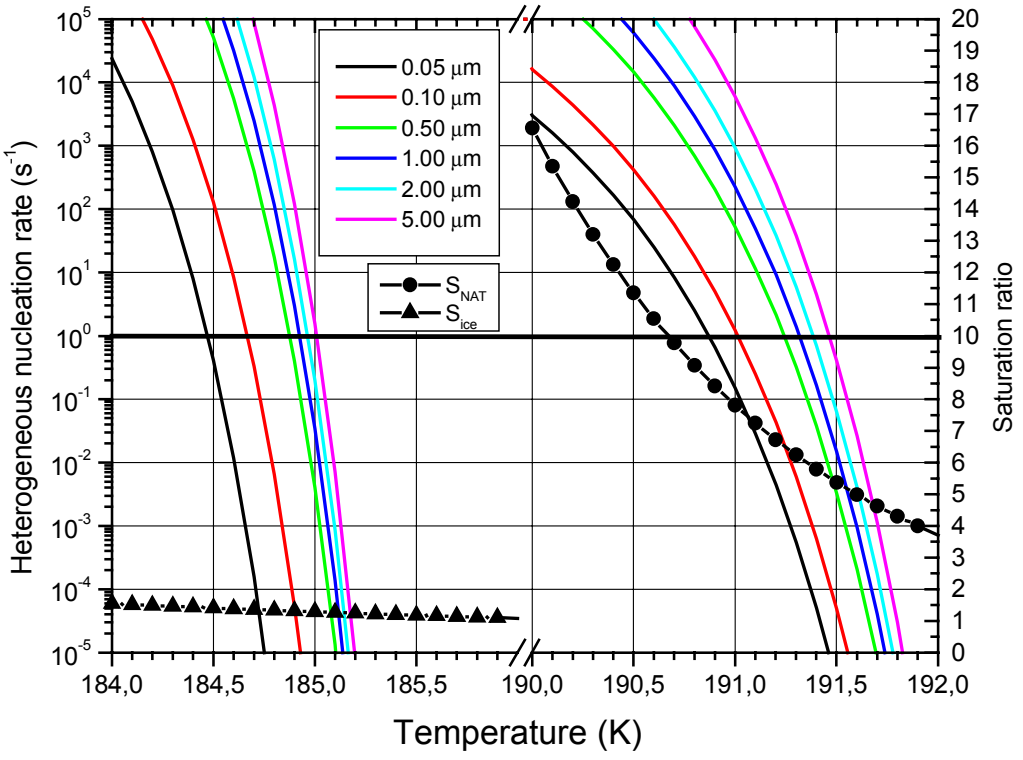

Figure 3.6 Heterogeneous deposition nucleation rates of NAT (right-hand side) and ice (left-hand side) particles of different sizes (see legend), calculated from (3.13) as function of temperature at 35 hPa pressure altitude, assuming 10 ppbv HNO_3 and 5 ppmv H_2O. Also show are the NAT and ice saturation ratios (curves with dot and triangle symbols).

Dissolution and melting of SAT particles.

If SAT particles are cooled in the presence of high concentrations of HNO_3 in the gas phase, thermodynamical calculations have shown that the particles become unstable [*Koop and Carslaw,* 1996]. Dissolution (deliquescence) of the particles will take place, and a film of STS will form on the particle surface by uptake of HNO_3 and H_2O until the particle is completely dissolved and turned into a liquid STS particle. This process requires HNO_3-saturated conditions with respect to STS. Therefore, if NAT particles are present concurrently with the SAT particles and the HNO_3 vapor is in equilibrium with the NAT particles, the HNO_3 partial pressure will be equal to the NAT saturation pressure, and supersaturation with respect to STS will not be possible, cf . Figure 3.2. In the present model, SAS particles will be transformed into equilibrium STS particles (accompanied HNO_3 and H_2O uptake) during cooling if the HNO_3 saturation ratio with respect to NAT is larger than 15. This process may compete with the nucleation by vapor deposition on pre-activated SAT, which will take place at a lower saturation ration, cf. Figure 3.6.

Laboratory investigations show that SAT particles will melt if heated to temperatures higher than approximately 216 K [*Middlebrook et al*., 1993], turning into liquid sulfate aerosol particles. An expression, given by *Tabazadeh et al.* [1994], has been used to calculate the melting temperature as function of water vapor pressure.

Condensation and evaporation.

The liquid and solid particles will grow or shrink due to condensation or evaporation. The gaseous mass flow by vapor diffusion to or from a particle is given from [*Pruppacher and Klett*, 1997, cp. 13]

$$\frac{dm}{dt} = 4\pi f_v C D(\rho_p - \rho_{sat}) = \frac{4\pi f_v C D M}{R}\left(\frac{P_p}{T} - \frac{P_{sat,r}(T_r)}{T_r}\right) \tag{3.18}$$

where ρ_p and $\rho_{sat,r}$ are the partial vapor density and the saturation vapor density at the particle surface, T_r is the temperature at the particle surface, D is the temperature- and pressure dependent diffusion coefficient for the controlling vapor (HNO_3 or H_2O), $C=C_c r$ is the "capacity" of the particle, and f_v is the ventilation factor for diffusion, arising because the particles fall.

For liquid spherical particles the “capacity” is equal to the particle radius (i.e. $C_c=1$). In the condensation/evaporation calculations, both solid type PSC particles (type 1a and 2) are assumed to be hexagonal cylinders, with an aspect ratio A=3 (i.e. ratio between cylinder length and diameter). This assumption is consistent with observations of ice particles [*Goodman et al.*, 1989]. The "capacity" of the cylinders has been approximated by the capacity of a prolate spheroid with axis ratio equal to the aspect ratio. According to *Pruppacher and Klett* [1997, cp. 13] the capacity is given from

$$C = \frac{\sqrt{A^2 - 1}}{\ln(A + \sqrt{A^2 - 1})} r = C_c r \tag{3.19}$$

using A=3, thus $C_c=1.61$ for the solid particles.

The difference between T and T_r, the temperature at the particle surface, exists because of the conductive heat flow, due to the release or absorption of latent heat (q) during condensation or evaporation. The surface temperature T_r can be deduced from the conductive heat transfer equation

$$f_h\left(\frac{dq}{dt}\right) = -L\left(\frac{dm}{dt}\right) = 4\pi f_h C k_a (T - T_r) \tag{3.20}$$

where L is the specific latent heat of evaporation (liquid particles) or sublimation (solid particles), k_a is the thermal conductivity of air, and f_h is the ventilation coefficient for heat transfer. $P_{sat,r}(T_r)$ can be expressed from $P_{sat}(T_r)$, using the Kelvin correction (3.2), and $P_{sat}(T_r)$ can be calculated from $P_{sat}(T)$ using the Clausius-Clapeyron equation

$$\frac{d \ln P_{sat}}{dT} = \frac{M L}{RT^2} \tag{3.21}$$

to give

$$P_{sat}(T_r) = P_{sat}(T) \exp\left(\frac{LM}{R}\left(\frac{T_r - T}{T_r T}\right)\right) \tag{3.22}$$

Combining (3.18), (3.20), (3.22) and (3.2), the vapor mass flow to or from a particle is given from

$$\frac{dm}{dt} = \frac{A_1 (S - A_2)}{1 + A_1 A_2 A_3} \tag{3.23}$$

where

$$A_1 = \frac{4\pi f_v C D M P_{sat}(T)}{RT} \tag{3.24}$$

A_2 is the Kelvin factor

$$A_2 = \exp\left(\frac{2M\sigma}{RT\rho r}\right) \tag{3.25}$$

and

$$A_3 = \frac{\left(\frac{LM}{RT} - 1\right) L}{4\pi f_h C k_a T} \tag{3.26}$$

Both the diffusion coefficient D and the thermal conductivity k_a must be corrected for discontinuity effects near the surfaces of the small particles. Using the vapor diffusion equation (3.18) and the heat transfer equation (3.20) it is assumed that the density and temperature fields are continuous right up to the particle surface. This assumption cannot hold within distances from the particle surface smaller than the mean free path, Λ, of the condensing molecules and corrections are especially important when the particle dimensions are of the same order of magnitude or even smaller than Λ. At distances larger than Λ the transfer processes by diffusion or heat conduction are valid, whereas gas kinetic processes [*Pruppacher and Klett*, 1997, cp. 5] are used to describe the transfer processes for distances smaller than Λ from the particle surface. Thus, according to the recommendations by *Fuchs and Sutugin* [1971] and *Toon et al.* [1989], D is multiplied by $\Gamma(Kn_d,\alpha_d)$, and k_a by $\Gamma(Kn_t,\alpha_t)$, where Γ is a function of the form

$$\Gamma(Kn,\alpha) = \frac{1}{1 + C_c \lambda(Kn,\alpha) Kn} \tag{3.27}$$

and Kn are the Knudsen numbers

$$Kn_d = \frac{\Lambda}{r} \qquad Kn_t = \frac{3 k_a M_a}{\rho_a v_a (C_{p,a} - 0.5R) r} \tag{3.28}$$

Here, v_a is the mean thermal speed of the air molecules

$$v_a = \sqrt{\frac{8RT}{\pi M}} \tag{3.29}$$

$\rho_a = PM_a/RT$ is the density of air, and $C_{p,a} = 7/2\ R$ is the specific (molar) heat capacity of air. The λ-function is given from the sticking coefficient α_d or thermal accommodation coefficient α_t, both assumed to be unity [*Pruppacher and Klett*, 1997, cp. 5], as

$$\lambda(Kn,\alpha) = \frac{1.33 + \frac{0.71}{Kn}}{1 + \frac{1}{Kn}} + \frac{1.33(1-\alpha)}{\alpha} \tag{3.30}$$

The vapor diffusion and heat conduction will be enhanced for falling particles, and the ventilation factors f_v (f_h) give the ratio between the diffusion (heat) transfer for a falling and the motionless particle. Expressions for the ventilation factors have likewise given by *Pruppacher and Klett* [1997, cp. 13] for liquid particles as

$$f_v = 1.00 + 0.108\ X;\ \ X < 1.4 \tag{3.31}$$

$$f_v = 0.78 + 0.308\ X;\ \ X \geq 1.4$$

and for solid particles as

$$f_v = 1.00 + 0.14\ X;\ \ X < 1 \tag{3.32}$$

$$f_v = 0.86 + 0.28\ X;\ \ X \geq 1$$

where $X = N_{Sc}^{1/3} N_{Re}^{1/2}$, and where $N_{Sc}=0.71$ is the Schmidt number, and N_{Re} is the Reynolds number (cf. the next section) of the particles. It is assumed that $f_h = f_v$.

For the co-condensation and co-evaporation of nitric acid and water into/from STS and NAT particles, the controlling vapor is assumed to be HNO_3 since the abundance of this species is roughly 500 times less than H_2O in the lower stratosphere. This means that these particle types are assumed to be in instantaneous equilibrium with the ambient water vapor.

For condensation and evaporation of STS particles, (3.23-3.26) is used to calculate the exchange of HNO_3 between the gas and condensed phase and thereby the mass of nitric acid in the particle (m_n), using the vapor pressure of HNO_3 over STS solution, i.e. $P_{sat} = P_{STS,n}(T,w_s,w_n)$. In order to calculate the accompanying exchange of H_2O, the ambient water vapor is assumed to be in equilibrium with the condensed phase, i.e. $P_{p,w} = P_{STS,r,w}(T,w_s,w_n)$, where the saturation vapor pressure has been corrected by the Kelvin effect, cf. (3.2). Figure 3.7 shows an example of a contour plot of $P_{STS,w}(T=190K,\ w_s,\ w_n)$, calculated at T=190 K, as function of the nitric and sulfuric acid weight fractions. To a good approximation, a linear relationship can be derived at a specific vapor pressure, corresponding to the ambient partial water vapor pressure at the given temperature for each particle size, between the nitric acid and sulfuric acid weight fraction

$$w_s = \alpha\left(P_{p,w}, T, r\right) w_n + \beta\left(P_{p,w}, T, r\right) \tag{3.33}$$

(As an example, at the pressure altitude $P_{air} = 35$ hPa and water vapor mixing ratio of 5 ppmv, the water partial pressure is 17.5 mPa. This is shown as the red straight line in Figure 3.7, giving the linear relation ship between w_n and w_s at this ambient condition).

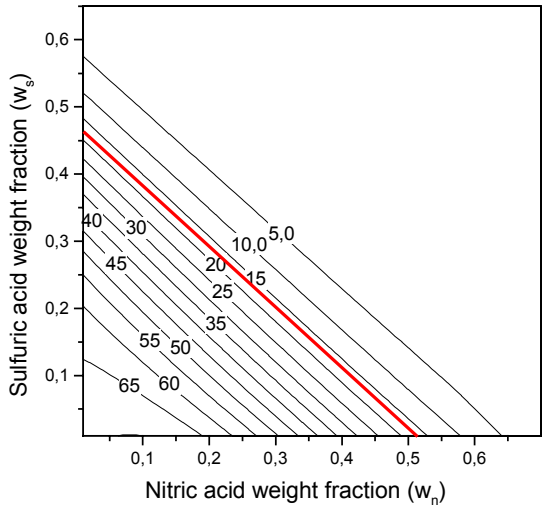

Figure 3.7 Contour plot of saturation vapor pressure of water over STS solution (mPa), calculated at 190 K as function of nitric and sulfuric acid weight fractions. Assuming that the ambient water partial pressure is equal to the vapor pressure at a specific temperature, a nearly linear relationship can be derived between w_n and w_s, shown as an example for $P_{p,w}$ = 17.5 mPa, corresponding to the water partial pressure at 35 hPa pressure altitude at a water vapor mixing ratio of 5 ppmv.

To calculate the mass of water in the particle (m_w), it is assumed that the mass of sulfuric acid in the particle (m_s) is constant. The total mass of the particle, $m_T=m_s+m_n+m_w$, hence

$$m_w = m_T - m_n - m_s = m_T(1 - w_n - w_s) = m_T(1 - w_n - \alpha w_n - \beta) = m_T - m_n - \alpha m_n - \beta m_T \tag{3.34}$$

or

$$m_w = \frac{m_s(1-\beta) - m_n(\alpha+\beta)}{\beta} \tag{3.35}$$

For the condensation or evaporation of NAT type 1a PSC particles, the HNO_3 saturation vapor pressure over NAT in used in equations (3.23-3.26) at the ambient water vapor partial pressure to calculate the HNO_3 mass exchange during condensation and evaporation. Furthermore, it is assumed that the H_2O to HNO_3 molecular vapor flux ratio is 3:1 for calculations of the H_2O exchange. The condensation or evaporation of the STS and NAT particles will only change the water vapor mixing ratio by a very little amount, even if nearly all the gaseous nitric acid is condensed. For the condensation or evaporation of ice type 2 PSC particles the similar parameters for water vapor and ice are used.

In fig. 3.8 are shown the relative mass flows in condensation/evaporation processes of HNO_3 to/from STS and NAT, and of H_2O to/from ice particles, calculated under different saturation conditions as function of particle radius from

$$\frac{1}{\tau_\varphi} = \frac{1}{V}\left|\frac{dV}{dt}\right| = \frac{1}{\rho V}\left|\frac{dm}{dt}\right| \tag{3.36}$$

where the expressions (3.23-3.26) has been used for dm/dt and ρV is the total mass of the particle. The time constants τ_φ (inverse of the relative mass flow values) are the time intervals, required for a

particle to increase or decrease its mass by a factor e by condensation or evaporation under constant saturation conditions.

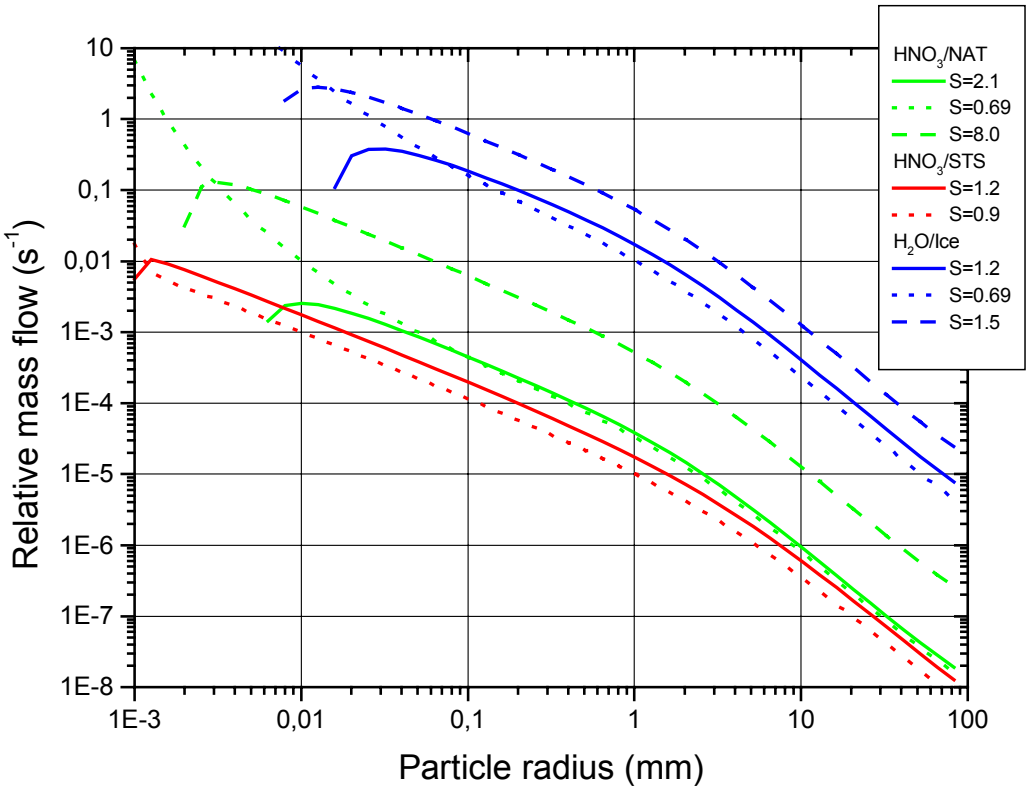

Figure 3.8 Relative mass flows during condensation (solid and dashed curves) and evaporation (dotted curves) for STS (red), NAT (green), and ice particles (blue curves), calculated at different saturation ratios as indicated in the legend. All calculations are performed at pressure altitude of 35 hPa; the condensation (solid curves) and evaporation (dotted) at equilibrium partial pressures at 193 K for NAT, 189 K for STS, and 186 K for ice by decreasing/increasing these temperatures instantaneously by 1K / 0.5 K. The dashed curves show the condensation mass flows at higher saturation ratios where NAT and ice particles are expected to form, assuming 10 ppbv HNO_3 and 5 ppmv H_2O at 35 hPa pressure altitude.

For calculation of the condensation (solid lines in Figure 3.8) and evaporation (dotted lines) relative mass flows, the particles have been assumed to be in equilibrium with the gas phase at 193 K (NAT), 189 K (STS), and 186 K (ice). The condensation curves (solid lines) have then been calculated by decreasing the temperature by 1K below these values. Thereby the saturation ratios increase to 2.1 (NAT), ≈1.2 (STS), and 1.2 (ice). Likewise for the evaporation curves (dotted lines), the temperatures have been increased by 0.5 K above the temperature values, decreasing the saturation ratios to 0.69 (NAT), ≈0.9 (STS), and 0.69 (ice). Finally, two sets of condensation calculations have been performed at the above temperatures for NAT and ice particles at the assumed saturation where the particles form (dashed curves). The ice saturation value around 1.5 in Figure 3.8 has been selected since this is roughly the value where ice type 2 PSC particles are nucleated by homogeneous freezing of STS particles or by water vapor deposition on NAT type 1a PSC, cf. Figures 3.5 and 3.6. The saturation value of S=8 for NAT type 1a PSC particles is the assumed value at nucleation of pre-activated SAT, cf. Figure 3.6.

The low nitric acid partial pressure compared to the water vapor accounts for the slow growth and evaporation rates of the STS and NAT particles, compared to the ice particles. It is also important to note the strong radius dependence of the condensation rates. The smaller STS and NAT particles get into equilibrium very fast while larger particles may take hours or longer to obtain equilibrium. The condensation curves bend downward at the smallest particle sizes and such small particles would actually be evaporating at the indicated saturation ratios in the legend due to the Kelvin effect (3.2). It is important to note that for STS particles, both due to the strong radius dependence of the condensation and evaporation rates, and also due to the Kelvin effects, the chemical composition of these particles will depend on their radius.

It can be seen from Figure 3.8 that e.g. a 10 μm ice particle would double its size in roughly 1000 seconds at S ≈ 1.5, and for larger particles it would take even longer. However the S value would decrease to a value near unity within this time interval, giving the reason why ice particles rarely grow larger than 10 μm ~ 50 μm by condensation. The similar argument holds for the STS and NAT particles which seldom grow larger than 5 μm ~ 10 μm.

Sedimentation.

The cloud particles are basically affected by two forces: gravitation and the frictional resistance to the movement by the air. The former force is given by

$$F_g = \frac{4\pi r^3}{3}(\rho - \rho_a)g \cong \frac{4\pi r^3}{3}\rho g \tag{3.37}$$

where g is the gravitational acceleration. The frictional force, for spherical particles of radius larger than the mean free path of the air molecules (Λ_a), is given by the Stoke's expression (*Fuchs*, 1964, § 7-8) as

$$F_f = -6\pi\eta r U \tag{3.38}$$

where η is the dynamic viscosity of air, and U is the particle terminal fall velocity. When r and ρ_a are of the same magnitude the empirical correction, introduced by Millikan, must be invoked, thus

$$F_f = -\frac{6\pi\eta r U}{1 + 1.246\frac{\Lambda_a}{r} + 0.42\frac{\Lambda_a}{r}\exp\left(-0.87\frac{r}{\Lambda_a}\right)} \tag{3.39}$$

Combining (3.37) and (3.38), the steady terminal fall velocity for the smaller particles (r<~10 μm) is calculated from

$$U = \frac{2\rho r^2 g}{9\eta\kappa}\left[1 + 1.246\frac{\Lambda_a}{r} + 0.42\frac{\Lambda_a}{r}\exp\left(-0.87\frac{r}{\Lambda_a}\right)\right] \tag{3.40}$$

where the dynamic shape factor κ, correcting for the columnar shape of solid particles, has been introduced, using κ = 1.12 as for the prolate ellipsoids with axes ratio of 3 (*Fuchs*, 1964, §12), and κ=1 for liquid spherical particles.

For the larger particles, (r>~10 μm), the Best (or Davies) number of the particles, N_{Be} [*Pruppacher and Klett*, 1997, ch.10] for liquid particles

$$N_{Be} = \frac{32 r^3 (\rho - \rho_a)\rho_a g}{3\eta^2} \tag{3.41a}$$

and for solid particles

$$N_{Be} = \frac{6\sqrt{3}\, r^3 (\rho - \rho_a)\, \rho_a\, g}{\eta^2} \tag{3.41b}$$

is used together with the Beard scheme to calculate the Reynolds number, N_{Re}

$$N_{\mathrm{Re}} = \exp\left(\sum_{j=0}^{3,6} B_j \left(\ln(N_{Be})\right)^j \right) \tag{3.42}$$

(j=0,..,3 for solid particles; j=0,..,6 for liquid particles) to obtain the fall velocity, using the definition of N_{Re}, as

$$N_{Re} = \frac{U\, 2\rho_a r}{\eta} \Leftrightarrow U = \frac{\eta\, N_{Re}}{2\,\rho_a r} \tag{3.43}$$

The following coefficients B_j in the Beard scheme have been used for liquid particles

$$B_0 = -3.18657,\ B_1 = 0.992696,\ B_2 = -0.153193\cdot 10^{-2},\ B_3 = -0.98705910^{-3},\ B_4 = -0.57887810^{-3},$$
$$B_5 = 0.85517610^{-4},\ B_6 = -0.32781510^{-5}$$

The polynomial coefficients B_j in the Beard scheme for solid particles have been calculated by linear tabulation from the values given by *Pruppacher and Klett* [1997, ch.10], using the aspect ratio of 3. The following values are used:

$$B_0 = -1.21590,\ B_1 = 0.97743,\ B_2 = -0.04928,\ B_3 = 0.0009573$$

The actual method of the calculation of the fall velocities is based on the Reynolds number, i.e. the Stokes-Millikan scheme is used for $N_{Re} < 10^{-2}$, and the Best scheme for the larger values. The calculated particle terminal fall velocities are shown in Figure 3.9. It can be seen that only particles of radius larger than ~ 5-10 μm have significant fall velocities.

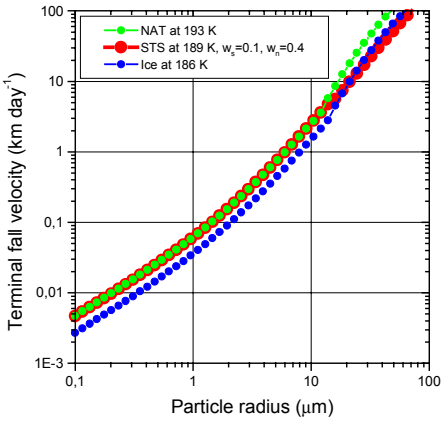

Figure 3.9 Particle terminal velocity, calculated at 35 hPa pressure altitude for NAT particles at 193 K (green curve), STS particles (w_s=0.1, w_n=0.4, green curve) at 189 K, and for ice particles at 188 K (blue curve).

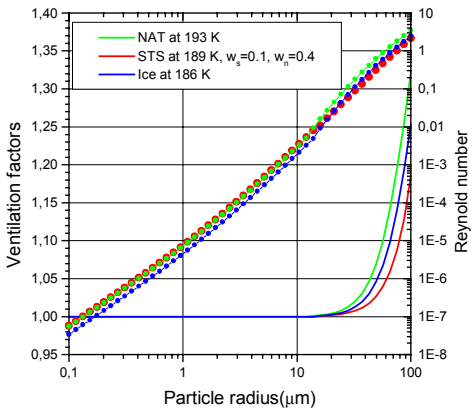

Figure 3.10 Ventilation factors f_v and Reynold number N_{re} (dotted curves), calculated at 35 hPa pressure altitude for NAT particles at 193 K (green curve), STS particles (w_s=0.1, w_n=0.4, green curve) at 189 K, and for ice particles at 188 K (blue curve).

Figure 3.10 shows the corresponding ventilation factors f_v and Reynold numbers N_{Re}, calculated at the same temperature and pressure conditions. Only the larger particles ($r >\sim 10$ μm) have significant ventilation factors; thus f_v will be set to unity for the smaller particles in this model. The Reynold numbers for the larger particles are calculated using the Beard scheme (3.41-3.42), whereas the N_{Re} values for the smaller particles are calculated from the Stoke-Millikan expression for the fall velocities (3.40) and the definition relation for the Reynolds number (3.43). Both f_v and N_{Re} decreases scarcely with decreasing pressure, and the temperature dependence is weak, thus the particle fall velocity of the larger particles is nearly independent of altitude.

Equilibrium composition of liquid supercooled ternary solution.

In certain applications within the PSC box model it is useful to calculate the bulk equilibrium composition of STS at a given ambient state. As temperatures decreases the liquid solution continuously change from a nearly binary sulfuric acid solution thorough STS into a nearly binary nitric acid solution by uptake of nitric acid (cf. Figure 2.3). In this process the gas phase HNO_3 partial pressure is reduced at the same time. The solution is assumed to be in equilibrium with the water vapor partial pressure. Assume we know the STS composition (w_s,w_n) at a certain temperature T and nitric acid partial pressure $P_{p,n}$ and want to calculate the composition (w_s',w_n') and partial pressure $P_{p,n}'$ of HNO_3 at a slightly different temperature T′. In the following, partial and saturation pressures refer to nitric acid. The available moles of HNO_3 per kg of air (Δn/kg air), available for condensation (evaporation), is given by

$$\frac{\Delta n}{kg\,air} = \frac{P_p - P_{sat}(T', w_s', w_n')}{RT'\rho_a(T')} \tag{3.44}$$

On the other hand, letting γ denote the number of moles in the condensed phase

$$\frac{\Delta n}{kg\,air} = \frac{\gamma_n'}{kg\,air} - \frac{\gamma_n}{kg\,air} = \frac{\gamma_s'}{kg\,air}\frac{\gamma_n'}{\gamma_s'} - \frac{\gamma_s}{kg\,air}\frac{\gamma_n}{\gamma_s} = \frac{\gamma_s}{kg\,air}\frac{M_s}{M_n}\left(\frac{w_n'}{w_s'} - \frac{w_n}{w_s}\right) \tag{3.45}$$

where M is the molar mass, and where we have used that γ_s'/kg air = γ_s/kg air, i.e. the number of H_2SO_4 moles in the condensed phase per kg air is constant. Noting that γ_s/kg air =μ_s/M_s, where μ_s is the mass mixing ratio of H_2SO_4, i.e. kg of condensed H_2SO_4 per kg air, we get

$$\frac{\Delta n}{kg\,air} = \frac{\mu_s}{M_n}\left(\frac{w_n'}{w_s'} - \frac{w_n}{w_s}\right) \tag{3.46}$$

or

$$P_p - P_{sat}(T', w_s', w_n') = P_a M_a \frac{\mu_s}{M_n}\left(\frac{w_n'}{w_s'} - \frac{w_n}{w_s}\right) \tag{3.47}$$

where P_a is the air pressure. In combination with (3.33), $w_s' = \alpha w_n' + \beta$, which expresses the water vapor equilibrium, equation (3.47) can be solved by iteration to get w_n'.

In Figure 3.11 is shown an example of a calculation of the equilibrium STS composition as function of temperature using the above expressions (solid curves). As in Figure 2.4, STS particles are cooled from 200K to 185 K at 35 hPa pressure altitude, assuming 10 ppbv HNO_3 and 5 ppmv H_2O in the gas phase. Comparison is made to the STS models of *Tabazadeh et al.* [1994] (dashed curves) and *Carslaw et al.* [1995] (dotted curves). At temperatures roughly below 190 K, where STS particles start developing in this example, the present model results roughly lie between the results of the two other models. At higher temperatures the present model calculates slightly

lower HNO_3 weight fractions than the other two models. The scatter plot of calculated H_2SO_4 versus HNO_3 weight fractions (right panel) show nearly the same results for all three models.

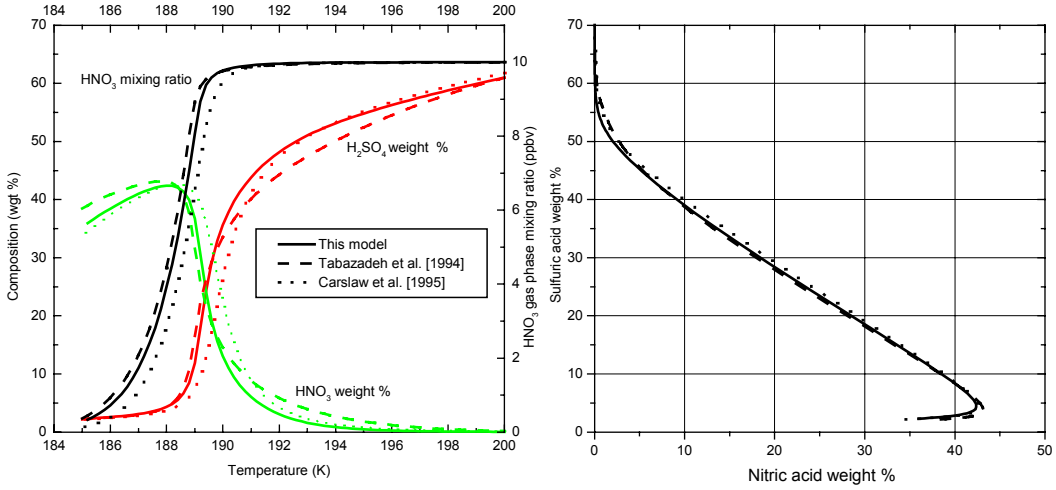

Figure 3.11 Equilibrium composition of STS particles, calculated using the present model during cooling from 200 K to 185 K at 35 hPa pressure altitude, assuming HNO_3=10 ppbv, H_2O=5 ppmv, and H_2SO_4=0.4 ppmv as in Figure 2.4. The solid curves show the results of the present model, compared to the STS models of *Tabazadeh et al.* [1994] (dashed curves) and *Carslaw et al.* [1994, 1995] (dotted curves). The red and green curves in the left panel show the H_2SO_4 and HNO_3 weight percent and the black curves the HNO_3 gas phase mixing ratio. The right-hand side panel shows a scatter plot of H_2SO_4 versus HNO_3 weight percents.

Thermodynamical and physical properties.

Various thermodynamical and physical properties of **(A)** the relevant vapors (HNO_3 and H_2O) and the air, and **(B)** the condensed substances (STS, NAT, and ice), have been used, together with **(C)** some parameters in the formulae in the above sections to describe the microphysical processes. A few references to sources of information on these properties have been given above, but for clarity the complete set of references will be given in this section.

A. Vapors and air.

As mentioned the HNO_3 and H_2O saturation vapor pressures over supercooled ternary solution, which depend on temperature and the H_2SO_4 and HNO_3 weight fractions (w_s and w_n), are calculated from the expressions given by *Luo et al.* [1995]. The saturation pressure of HNO_3 over NAT has been calculated from the expression given by *Hanson and Mauersberger* [1988] and the saturation pressures of H_2O vapor over ice and water have been taken from *Jancso et al.* [1970] and *Tabazadeh et al.* [1997c]. The HNO_3 specific latent heat of evaporation (STS) and sublimation (NAT) have been calculated from the Clausius-Clapeyron equation (3.21). The specific heat of water sublimation has been calculated from the tabulation given by *List* [1951, p. 343].

The temperature and pressure dependent molecular mean free path of air molecules Λ_a has been calculated from the expression given by *Pruppacher and Klett* [1997, cp. 10]. In order to calculate

the effective mean free path of the of the condensing molecules Λ_k (i.e. Λ_n for HNO_3 vapor, and Λ_w for H_2O vapor) the following expression is used [*Hamill et al.*, 1977]

$$\Lambda_k = \frac{\sqrt{\frac{M_a + M_k}{M_a}}}{\frac{\pi}{4}(d_a + d_k)^2 n_a} \tag{3.48}$$

where d_k is the molecular diameter and M_k is the molar mass of the condensing molecules; the a-indexed symbols are the same quantities for air molecules, and n_a is the number density of air molecules. Thus,

$$\Lambda_k = 2\sqrt{2}\,\frac{\sqrt{\frac{M_k + M_a}{M_a}}}{\left(\frac{d_k + d_a}{d_a}\right)^2}\,\Lambda_a = \Theta_k\,\Lambda_a \tag{3.49}$$

Using the molecular diameters d_a=3.65 Å, d_n=5.2 Å, and d_w=4.0 Å (T. Pedersen, private communication, 1990) the following correction factors are calculated: Θ_n=0.857, and Θ_w=0.820.

The temperature and pressure dependent diffusion coefficient D_w for water vapor has been calculated from the expression given by *Pruppacher and Klett* [1997, cp. 13]. Using the relationship $D_n = v_n \Lambda_n / 3$ between the diffusion coefficient D_n, the mean thermal speed v_n (3.29), and the mean free path Λ_n of the condensing HNO_3-molecules, then

$$D_n = \sqrt{\frac{M_w}{M_n}}\,\frac{\Theta_n}{\Theta_w}\,D_w = 0.559\,D_w \tag{3.50}$$

Both the sticking coefficients α_d, and the thermal accommodation coefficients α_t have been set to unity for both vapors [*Pruppacher and Klett*, 1997, cp. 5]. Formulae for the thermal conductivity of air k_a are given by *Pruppacher and Klett* [1997, ch. 13], and for the dynamic viscosity of air by *List* [1951, p.394].

B. Condensed substance.

The bulk density of STS is calculated from an expression given by *Luo et al* [1996]. An expression for the density of binary sulfuric acid solution has been derived from the tabulations by *Perry* [1963, p. 3-79, 3-80]. The density of NAT is assumed to be $\rho_{NAT}=1.62\cdot10^3$ kg m^{-3} [*Taesler et al.* 1975], density of SAT to be $\rho_{SAT}=1.59\cdot10^3$ kg m^{-3} [*Kjälman and Olovson,* 1972], and an expression from *Pruppacher and Klett* [1997, cp. 4] has been used to calculate the density of ice.

The surface tension between binary sulfuric acid solution and air is calculated from an expression given by *Tabazadeh et al.* [2000], which is based on laboratory measurements by *Myhre et al.* [1998]. The surface tension between binary nitric acid solution and air is calculated from the expression given by *Granzhan and Laktionova* [1975] and the surface tension between STS and air is calculated from a molality-weighted average of the two binary acid surface tensions. The expression given by *Drdla and Turco* (1991) is used for surface tension between NAT and air, and the surface tension between ice and air is assumed to be 0.105 Nm^{-1} [*Pruppacher and Klett*, 1997, cp. 5].

The latent heat of ice melting is calculated from *Pruppacher and Klett* [1997, cp. 4]. The SAT melting temperature is calculated from the expression given by *Tabazadeh et al.* [1994] and the diffusion activation energy of water molecules in binary sulfuric acid solution across the solution/ice phase boundary is calculated from *Tabazadeh et al.* [2000].

C. Parameters.

Various parameters have been used to describe the microphysical processes; values of these parameters have been stated above in the respective sections, but as an overview a table of these values is given below:

Prefactor of the rate of homogeneous freezing	$N_c=5.85\cdot10^{18}$ m^{-2}
Prefactor of the rate of nucleation by vapor deposition	$C_m = 2\cdot10^{23}$ m^{-2}
Compatibility (contact) nucleation parameter (SAT/NAT)	$M = 0.76$
Compatibility (contact) nucleation parameter (NAT/ice)	$M = 0.95$
Prefactor of solid particle "capacity"	$C_c = 1.61$
Aspect ratio of solid particles	$A = 3$
Dynamic shape factor of solid particles	$\kappa = 1.12$

4. PSC simulation models.

PSC box models have been developed to describe the temporal development of particle size distributions in ensembles of sulfate aerosols, type 1a and 1b PSC, and type 2 PSC cloud particles, respectively, at a single point (trajectory air parcel or grid point) due to changes in temperature, pressure, and gaseous mixing ratios of HNO_3 and H_2O in the ambient air. Basic microphysical processes are incorporated in modeling the development of the particles: homogeneous freezing of liquid particles, heterogeneous nucleation by vapor deposition, condensation/evaporation by vapor diffusion, SAT particle melting and dissolution, and sedimentation as described in chapter 3. The PSC box models have been designed to facilitate an incorporation in grid points within a larger atmospheric chemistry models, the box models can be coupled to (photochemical) trajectory calculations, or box models can be stacked to form a 1-dimensional column model.

The box model may interact with stratospheric chemistry models, describing the uptake of chlorine and bromine species on the surfaces of the particles, and the heterogeneous chemical reactions that convert the inactive halogen compounds into reactive forms (chapter 2). This requires a time dependent modeling of the particle surface area densities as provided by the box model. The other coupling to the chemistry is due to the fact that the formation of the nitric acid (STS and NAT) and ice particles removes HNO_3 and H_2O from the gas phase, where especially the nitric acid would otherwise enter the set of gas phase (photo) chemical reactions. The flow of vapor between the gas and condensed phase is needed in the chemical continuity equations of HNO_3 and H_2O; as shown in chapter 3 this vapor flow by condensation/evaporation depends on the size of the particles. Sedimentation of the particles may lead to denitrification and dehydration, and it has also been shown, that the fall velocities depend strongly on the particle radius; knowledge of the particle size distribution is therefore required in order to simulate the sedimentation effects properly.

Finally, the box models facilitate a coupling to an optical model (chapter 5) to calculate aerosol backscatter ratios or extinction coefficients at different wavelengths, based on Mie scattering theory. The optical model takes as input the particle size distributions and chemical compositions as produced by the PSC box models.

Lagrangian and Eulerian model versions.

In principle the change in particle size distributions due to particle growth/shrink by condensation/evaporation could be calculated in two ways:

A) From the initial sulfate aerosol size distribution, particles representing the whole size range are selected. The individual selected particles each represent a fixed number of particles per kg of air which all behave like *the selected representative*. For each individual selected representative, it's mass, chemical composition, and radius are calculated from equations (3.23-3.26). Thereby the calculations follow the same individual representatives in radius space. This model version will be designated the "Lagrangian" version (in radius space).

B) The initial size range is divided into a number of fixed size bins. The initial size distribution specifies the number of particles per kg of air in each size bin. For each time step the change in mass, chemical composition, and thereby the new radius is calculated for parti-

cles in each size bin from equations (3.23-3.26). A number of particles are shifted to the neighbor size bin, depending on the relative change in calculated radius compared to the span of the individual size bins. Thereby the calculations are performed at fixed radii and particles are moved up and down between size bins. This model version is designated the "Eulerian" version (in radius space).

It should be noticed that the two model versions apply the same microphysical and thermodynamical calculations. The difference in calculating the size distributions in the two model versions is illustrated in Figure 4.1. It is important to note the "Lagrangian" or "Eulerian" calculations relate to radius space and not how the box model moves around in air space.

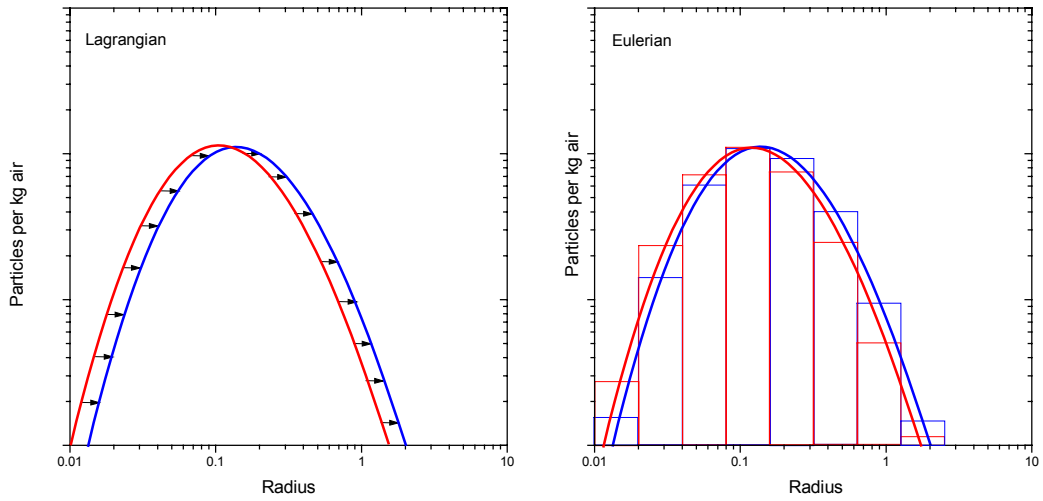

Figure 4.1 Schematic illustration of the "Lagrangian" and "Eulerian" method for calculating changes in particle size distributions during condensation/evaporation. The red and blue curves illustrate the particle size distributions in two consecutive time steps during particle growth. In the Lagrangian model version (left panel) the growth of individual particles, each representing certain number of particles per kg of air, is followed as illustrated by the arrows. In the Eulerian version particles are shifted between fixed size bins, the small-size bins loose particles and the large-size bins increase the number of particles during the time step.

There are a number of advantages/disadvantages in the two model versions. The Lagrangian version applies a straightforward calculation of changes in radius, mass, and composition due to condensation/evaporation from the basic microphysical and thermodynamical equations. This model version will perform an exactly reversible calculation of size distributions. This means that if particles from a given initial size distribution are cooled to low temperatures and subsequently heated to the initial temperature, the initial size distribution will be generated at the end of the simulation (even if phase transitions occur throughout the simulation). In the Eulerian model version numerical diffusion between size bins will induce minor deviations between the initial and final size distribution, the error depending on the number of chosen size bins. The Lagrangian version is also suited for non-equilibrium simulations of PSCs in rapidly changing temperature conditions, e.g. in mountain leewaves. In the Eulerian model version, the STS type 1b PSC particles are assumed to be in equilibrium with the gas phase HNO_3 and all liquid particles in the size distribution to have the same composition at a given time. This will speed up the calculations significantly and integrated particle properties, e.g. total particle surface area or volume densities do not deviate much from the Lagrangian calculations. In addition to computa-

tional speed, the advantage of the Eulerian model lies in the possibility to build a vertically layered model and perform sedimentation simulations between layers, e.g. in a one-dimensional column model or in grid points within larger atmospheric 2-D or 3-D models.

In both model versions the fluxes of nitric acid and water vapor to and from the particles due to condensation/evaporation are calculated and thereby the gas phase concentrations of these species.

Structure of PSC particles.

At high stratospheric temperatures (> 216 K) the presence of a background of liquid, nearly binary, sulfuric acid aerosols with a prescribed size distribution in equilibrium with the ambient water vapor partial pressure will be assumed. Thereby the sulfuric acid weight fraction of the particles is given, and thereby also the mass of H_2SO_4 in individual particles of a given size. This H_2SO_4-mass is assumed to be constant throughout the simulations in both model versions. By prescribing the initial particle size distribution, the total mass of H_2SO_4 in all particles is fixed (the H_2SO_4 mass mixing ratio, or mass of sulfuric acid in the particles per kg of air).

As temperature decreases the liquid sulfate aerosol gradually takes up nitric acid and water, continuously turning into fully developed liquid STS type 1b PSC particles, cf. Figures 2.3, 2.4, 3.11, and 4.2. The models only comprehend one type of liquid particles, and discrimination between liquid sulfate aerosol at warm temperatures and liquid STS type 1b PSC particles at low temperature is solely based on the calculated chemical compositions. The particles will eventually transform into solid particles by homogeneous freezing of ice in the particles, typically at temperatures a few K below the ice frost point (cf. Figures 2.4 and 3.5). It is assumed that the whole droplet will freeze in this process. Under these conditions the particles typically have a chemical composition of ≈ 35% HNO_3 and ≈ 3 % H_2SO_4 with an H_2O:HNO_3 molar ratio around 6-8 (cf. Figure 2.4). During the freezing process, it is assumed that each H_2SO_4 molecule in the particle combines with 4 H_2O molecules, forming an inclusion (core) of sulfuric acid tetrahydrate (SAT) and that the each HNO_3 molecule combines with 3 H_2O molecules, forming nitric acid trihydrate (NAT). After a number of the water molecules in this way have been bound to the available H_2SO_4 and HNO_3 in the droplet there will still be unbound water molecules available to form water ice. This water, which is neither bound to H_2SO_4 as SAT, nor to HNO_3 as NAT, will be designated as “excess ice”.

In the Lagrangian model version the condensed mass of HNO_3 and H_2O in the particle representatives constitute the integration variables, calculated using the basic microphysical equations as described in chapter 3. The chemical composition and radii of the particle representatives are calculated from the mass of HNO_3, H_2O, and H_2SO_4. A particle-type flag is assigned to each particle representative indicating the particle type and the actual physical phase (liquid or solid) of the particle. This particle-type flag will change when processes involving phase changes take place. The amount of excess ice or NAT determines which of the three solid type particle the representative belongs to.

In the Eulerian model version the solid type particles will be regarded as composed of a core of SAT, surrounded by a shell of NAT (type 1a PSC), and an additional shell of excess ice (type 2 PSC).

Water in excess ice will condense on/evaporate from the solid particles, depending on the water vapor saturation ratio with respect to ice. Water molecules which are bound in NAT will con-

dense/evaporate to/from the solid particles in a 3:1 molar ratio of the HNO_3 condensation/evaporation rate, depending on the HNO_3 saturation ratio with respect to NAT. Water molecules, which are bound to SAT, will remain constant as long as the particle remains in the solid state. Above the SAT melting temperature, or below the threshold for eventual SAT dissolution, the SAT particles turn into liquid particles. Thereby the water content in the particles adjusts to become into equilibrium with the ambient H_2O partial pressure. The H_2SO_4 mass in the particles is assumed to be constant.

Structure of the PSC models.

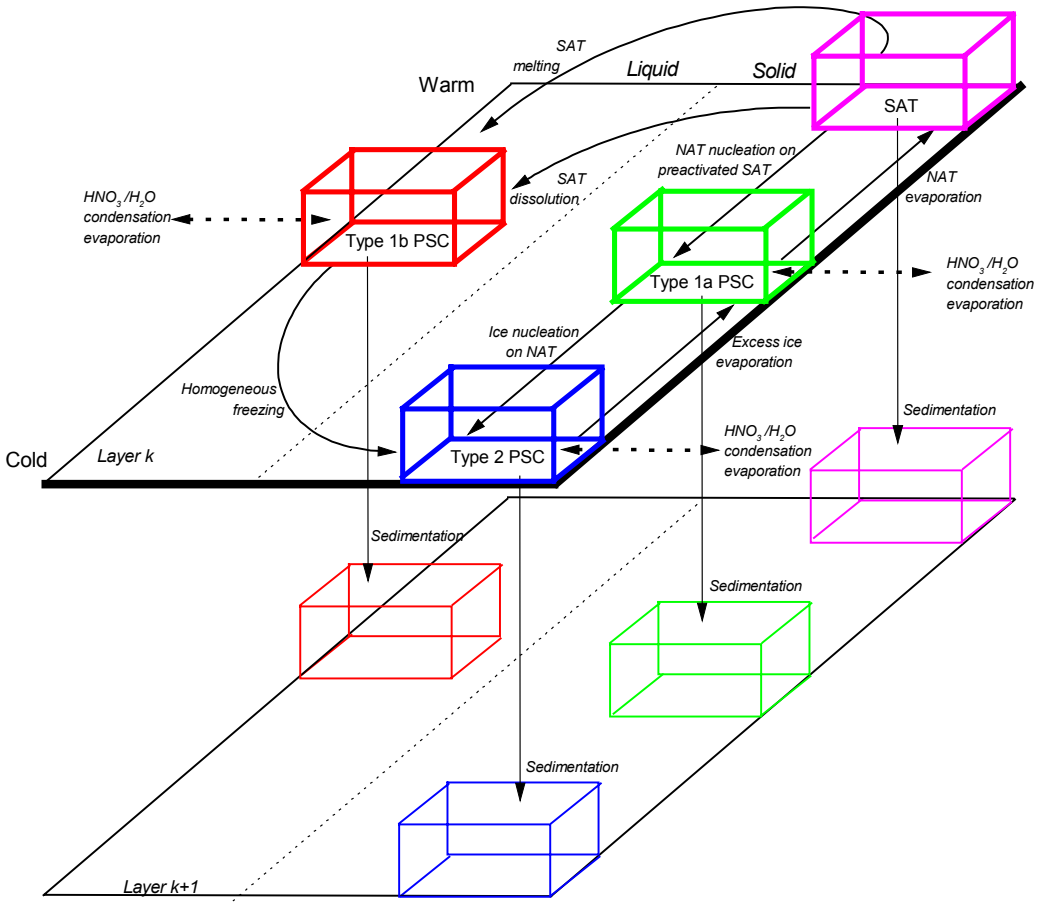

Figure 4.2 Structure of the PSC box model. At each layer in the vertical direction the size distributions are calculated for four types of stratospheric particles, indicated by the colored boxes. Changes in size distributions due to condensation/evaporation are calculated using either the "Lagrangian" or "Eulerian" approach. Arrows indicate the different microphysical processes taken into account, cf. chapter 3. Calculation of sedimentation between layers is only possibly using the Eulerian approach.

The layout of the box model is shown in fig. 4.2. In the Lagrangian model version only one size distribution is calculated and the particle-type flag indicates the particle type. In the Eulerian model at layer nº *k* in the vertical direction, the particle size distributions will be calculated individually for the four particle types: sulfate aerosols or type 1b PSC, type 1a PSC (NAT), type 2 PSC (ice), frozen sulfate aerosol particles (SAT) using either the Lagrangian or Eulerian method. The size distributions of the particles are indicated by the boxes in fig. 4.2 together with the basic microphysical processes (arrows in the figure), that may change the size distributions, cf. also Figure 2.4.

In the Eulerian model version the particles of a given particle type are transferred to higher radius bins within the size distribution due to growth by vapor condensation. As the temperature increases, the particles will again shift to lower radius bins due to evaporation. This process is calculated individually for each PSC particle type. Processes involving a phase transition (homogeneous freezing of STS particles, melting or dissolution of SAT particles) may lead to a transfer of particles to another particle type as indicated in Figure 4.2. Likewise the complete evaporation of excess ice and NAT will lead to a transfer from type 2 to type 1a, and from type 1a to SAT, respectively. This process will be designated “core return”. NAT nucleation on pre-activated SAT and ice nucleation on type 1a NAT PSC will transfer particles in the opposite direction. Particles are transferred between different particle types having the same radius value during the transfer.

In the Eulerian model version the fall-out of particles by sedimentation from layer *k* to layer *k+1* below is calculated, and the fall-in of particles from the layer *k-1* above is included in the calculation of the size distribution of the actual layer.

The size range of each particle type distribution in the Eulerian model version is discretisized into a number N of size bins. Because the particle sizes span several orders of magnitudes, a geometrically increasing volume scale has been chosen [*Turco et al.*, 1979; *Toon et al.*, 1988]. The geometric volume scale is defined as

$$V_{i+1} = f\,V_i\,; \qquad V_i = f^{i-1} V_1 \tag{4.1}$$

where V_i is the particle volume in bin *i* ($1 \le i \le N$), and f is the ratio of volumes of adjacent bins, f>1. The central radius r_i of bin *i,* the corresponding radius bin width (Δr_i), and volume bin width (ΔV_i) are given by

$$r_i = r_1\, f^{\frac{i-1}{3}} \tag{4.2}$$

$$\Delta r_i = r_i \left(\frac{2}{f+1} \right)^{1/3} (f^{1/3} - 1) \tag{4.3}$$

$$\Delta V_i = 2\,\frac{f-1}{f+1} V_i \tag{4.4}$$

The relations between the minimum radius (r_1), maximum radius r_N, f, and N are given by

$$r_N = r_1 f^{\frac{N-1}{3}} \quad \Leftrightarrow \quad f = \exp\left(\frac{\ln \frac{r_N}{r_1}}{\frac{N-1}{3}} \right) \qquad N \approx \frac{3 \ln \frac{r_N}{r_1}}{\ln f} + 1 \tag{4.5}$$

Using a size scale of N=50 bins, f=2, and a minimum particle radius of r_1=0.001 µm of the first bin, the radius of the 50th bin will be r_{50}=82.6 µm. This size range covers the typical radius values of

sulfate aerosols and PSCs of both types, and will be used as the standard scale in the model. Equation (4.2) is also used to define the radii of the particle representatives in the initial state in the Lagrangian model version.

The four boxes in Figure 4.2 represents the size distributions of the four types of particles in the Eulerian model version, and the boxes should be regarded as divided into N small boxes, each representing the individual bins on the volume scale.

The particle volume value V_i (and radius, and surface area) of each bin is fixed in the Eulerian model version, and it is assumed that all particles in a given bin have the same size. As the particles grow by condensation, the particles are transferred to higher bin numbers, hence the number density of particles in each size bin n_i constitute the integration variables of this model version, together with the average shell and core volumes of condensed substance of the solid type particles in the individual size bins.

In the Eulerian model version the calculation of change in size distribution of the liquid particles due to condensation/evaporation have been simplified to increase the speed of calculation. Only the smallest particles will be in equilibrium with the gas phase HNO_3 during fast temperature changing conditions and in principle the composition of the liquid particles will depend on their radius. To represent these effects requires the usage of the Lagrangian model version, which however is computational demanding. In the Eulerian model, all liquid particles are assumed to be in instantaneous equilibrium with the HNO_3 and H_2O gas phase, and all particles to have the same equilibrium composition at a specific ambient state. The method to calculate the change in size distribution due to changes in temperature, pressure, and gas phase mixing ratios closely follows the method suggested for binary sulfate aerosol by *Steele and Hamill* [1981] and for ternary solution particles by *Hamill et al.* [1996]. The method assumes that the mass of H_2SO_4 in a given particle is constant, i.e.

$$m_s = \frac{4\pi}{3} r^3 \rho(T, w_s, w_n)\, w_s = const \tag{4.6}$$

The ratio between particle volumes in two consecutive atmospheric states, the new state indicated by marked (′) symbols, is calculated from

$$V \rho(T, w_s, w_n) w_s = V' \rho(T', w_s', w_n') w_s' \tag{4.7}$$

or

$$V' = \frac{\rho(T, w_s, w_n) w_s}{\rho(T', w_s', w_n') w_s'} \quad \Leftrightarrow \quad V' = \tau V \tag{4.8}$$

On the geometrically increasing volume scale (4.1), $V_i = V_1 f^{i-1}$, and (4.8) is used to calculate the change in bin index *i* between the two states as

$$\ln V_i' = \ln(\tau V_i) \qquad \ln V_1 + (i'-1)\ln f = \ln \tau + \ln V_1 + (i-1)\ln f \tag{4.9}$$

or

$$i' = i + \frac{\ln \tau}{\ln f} \tag{4.10}$$

where $i < i' < i+1$ for particle growth and $i-1 < i' < i$ for shrink, i.e. $i' - i$ gives the shift of the size distribution measured in bin number units. The shifted distribution of number concentrations n_j is calculated by cubic spline interpolation in the distribution n_i corresponding to original state.

The general flow pattern of particles into and out of a single size bin in the Eulerian model version is illustrated in Figure 4.3 in the case of growth by condensation (during evaporation the flows between adjacent bins are reversed). Not all flows will actually carry particles at the same time; thus

the in-going nucleation flow of new particles and core return from the same particles cannot take place simultaneously. Further, not all the flows represented in the figure apply to the STS, SAT, or and the type 2 PSC particle bins. For STS particles there are no core return flows. For the SAT particles only the outgoing nucleation flow and the ingoing core return flow (to and from the type 1a PSC) are considered. For the type 2 PSC particles the outgoing nucleation flow and in-going core return flow are not present. For the type 1a PSC bins all the indicated flows are considered.

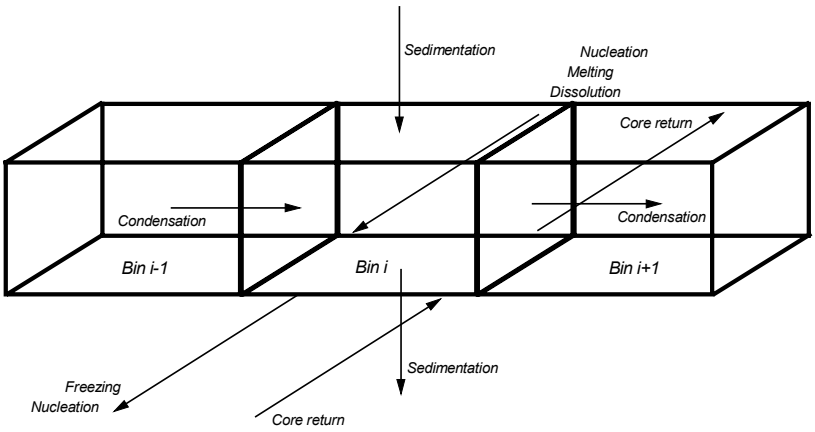

Figure 4.3 Schematic illustration of flows of particles to and from bin number *i*.

The continuity equation for the number density of particles n_i in bin *i* of a PSC 1 bin is given by

$$\frac{dn_i}{dt} = (\nu_i^{in} + \varphi_i^{in} + \psi_i^{in} + \omega_i^{in}) - (\nu_i^{out} + \varphi_i^{out} + \psi_i^{out} + \omega_i^{out}) \tag{4.11}$$

where ν is the nucleation flow, φ is the condensation/evaporation flow, ψ is the sedimentation flow, and ω is the core return flow.

For the outgoing homogeneous freezing flow from STS particles, the condition, $J_{f,} \cdot V_i \cdot dt > 1$, specifies if all particles in bin *i* will transferred to the type 2 PSC bin. The homogeneous freezing J_f rate is calculated from (3.3). The outgoing nucleation flows from SAT or type 1a PSC particle bins are given by

$$\nu_i^{out} = J(r_i)\, n_i \tag{4.12}$$

where J is the nucleation rate, given by (3.13), using the temperature and partial pressure of layer *k*. For the outgoing nucleation flow from SAT particles (i.e. the nucleation into type 1a PSC particles) the partial pressure of HNO_3 is used; for the nucleation into type 2 PSC the partial pressure of H_2O is used.

The outgoing condensation flows for STS particles are calculated as explained above using equation (4.10). The solid type outgoing condensation/evaporation flow is calculated from

$$\varphi_i^{out} = \frac{1}{V_i}\left|\frac{d\,V'_i}{dt}\right| = \frac{1}{\rho\,V_i}\left|\frac{dm_i}{dt}\right| n_i \tag{4.13}$$

where $V'_i=n_iV_i$ is the total volume of all particles in the bin, ρ is the density of the surface condensate (NAT or ice), and dm_i/dt is the vapor flow to or from a single particle by condensation or evaporation, calculated from (3.26)-(3.26), using the temperature and the saturation ratio of the controlling vapor in layer *k*. In the type 1a PSC case of co-condensation of HNO_3 and H_2O into NAT dm_i/dt must be corrected by a molar mass factor $(M_n+3M_w)/M_n$.

The outgoing sedimentation flow of layer *k* is calculated from the particle fall velocity U_k of layer *k* as

$$\psi_{i,k}^{out} = \frac{U_k}{\Delta h_k} n_i \tag{4.14}$$

where Δh_k is the vertical thickness the layer, assuming the particle in the layer to be well mixed. The fall velocities U_k are calculated from (3.40) or (3.43).

The in-going flows are calculated in the same way, using the appropriate variables of the bins and layers from where the flows originate, and the in-going flows are equal to the outgoing flows of the bins from where the flows originate, conserving particle number densities. Because n_i are calculated as the number of particles per unit air mass, the correction factor $\rho_{a,k-1}/\rho_{a,k}$ of the ratio between air densities in layer *k-1* and *k* must be applied to calculate the in-going sedimentation flow, thus

$$\psi_{i,k}^{in} = \frac{\rho_{a,k-1}}{\rho_{a,k}} \psi_{i,k-1}^{out} \tag{4.15}$$

Each type 1a PSC particle in bin *i* carries a SAT core volume, and the type 2 PSC particles carry both a SAT core volume, and also an inner NAT shell volume. These volumes are initially specified, when the particles are created by homogeneous freezing in bin *i*. The *average* core and inner shell volumes of the solid type PSC particles in bin *i* are defined as the *internal bin-volumes*. The internal bin-volumes will change, due to the flows of particles between bins, and the rate of change is calculated from the particle bin flows, assuming that all particles in one bin carries the same average core and inner shell volumes.

The change in the internal structure of type 1a PSC particles during condensation growth is schematically illustrated in fig. 4.4.

Assume from time t_0 onward the particles grow, flowing to higher bins along the down-slanting lines, carrying along the SAT core volume, and increasing the thickness of the NAT shell. The particle volume in each bin is fixed, thus the core volume in the individual bins will take up a progressively smaller part of the total particle volume during condensation, corresponding to an increasing volume of the condensed substance in the surface shell. A similar, but more complex, diagram could be drawn for the evolution of the type 2 PSC particles, the difference being that the interior of the particles are composed of a SAT core and an inner NAT shell.

When the solid type PSC particles are evaporating and flowing to lower bins (upward along the slanted arrows), the shell volume decreases until the point, when the core volumes fill out the whole bin volume in the individual bins. At this point, the surface shell has evaporated completely, and the particles in bin *i* are transferred to bin *i* of the lower particle category (i.e. type 2 PSC to type 1a PSC, or type 1a PSC to SAT particles).

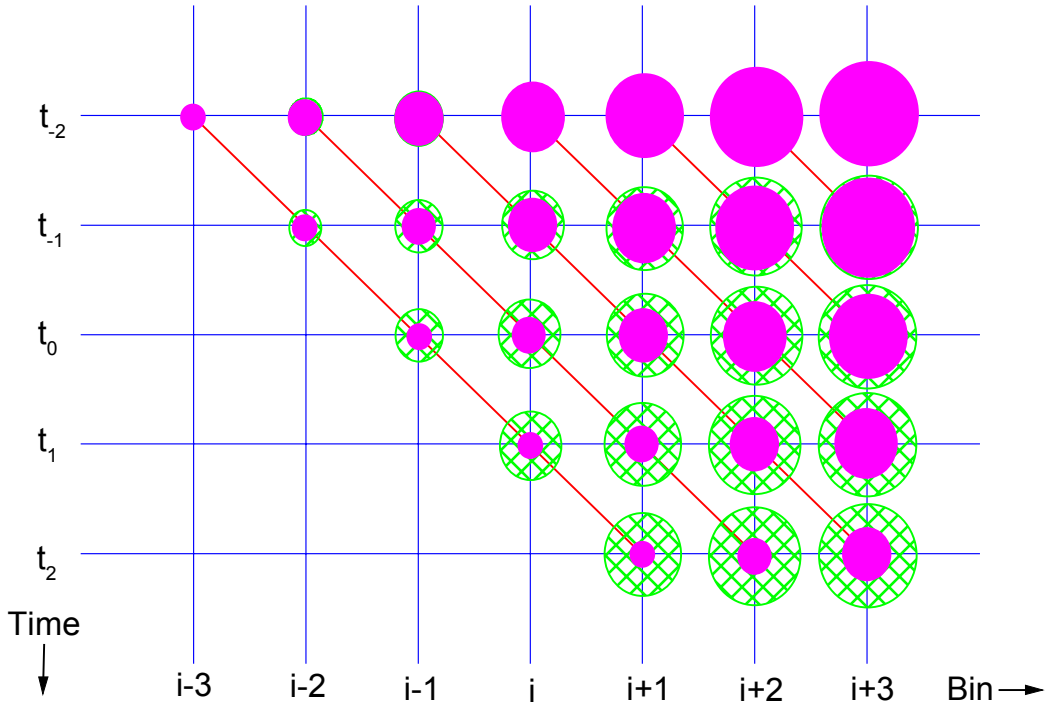

Figure 4.4 Schematic illustration of the internal structure of a type 1a PSC particle during condensation or evaporation in the Eulerian model version. The magenta dots illustrate the SAT core volumes, surrounded by a NAT shell as shown in green. Consider a particle in bin *i* at time t_0. During HNO_3 and H_2O condensation the NAT shell volume increases and the particle moves to bin *i+1* at time t_1 along the down-sloping red line, pertaining it's core volume and increasing the total volume, corresponding to volumes in bin *i+1*. Particles in a given bin always have the same total volume. As time progresses during NAT condensation, particles move in from lower bin numbers with gradually smaller core volumes. During evaporation particle move upward along the red lines, gradually decreasing the NAT shell volumes. When the particles loose the entire NAT shell and the SAT core volume corresponds to the bin volume as show in the upper row a "core return process" occurs, converting the particle from a type 1a PSC to a SAT particle. A similar diagram can be constructed for type 2 PSC particles, holding a SAT core, an inner NAT shell, and an outer ice shell.

Both box models calculate the particle size distributions in discrete time steps, alternating with the calculations in the surrounding (calling) model, which may utilize the generated particle surface area densities. The box model will take as input at the start of a time step the ambient temperature and pressure, the partial pressures of HNO_3 and H_2O, and the current number density n_i. For the Lagrangian model version in addition the mass of H_2SO_4, HNO_3, and H_2O in the particles, and for the Eulerian version the internal bin-volumes of the particles in each bin, and the inflow by sedimentation of particles from the layer above. At the end of the time step, in which the temperature is assumed to be constant, the box model will return the new values of n_i, acid masses or internal bin volumes, the outflow of particles by sedimentation to the layer below, and the new values nitric acid and water vapor partial pressures. In order to simulate the vertical transport in a column, the point-wise calculations using the Eulerian version have to be performed in a sequence from the top-layer (with the assumption of no sedimentation input flow from above) to the bottom layer, where the net-flow of particles out of the column is calculated.

5. Optical PSC and aerosol model.

Models of stratospheric aerosol size distributions.

Many optical models of size distributions have been used to describe the aerosols at different altitudes and under different atmospheric conditions [*Russel et al.*, 1981]. Among these models the lognormal size distribution [*Pinnick et al.*, 1976]

$$n(r) = \frac{N_t}{\sqrt{2\pi}\, r \ln\zeta} \exp\left[-\frac{1}{2}\left(\frac{\ln(r/r_m)}{\ln\zeta} \right)^2 \right] \tag{5.1}$$

is probably the most commonly used model for the stratospheric aerosols under non-recently volcanic situations. Here, N_t is the total number of particles per unit air volume (or per kg of air), r_m is the median or mode radius dividing the particle ensemble into two parts of which half of the particles have radii smaller than r_m and the other half have larger radii; ζ is the geometric standard deviation, and n(r) gives the number of particles of radius r per unit air volume per unit radius (differential size distribution). The total surface area density A_t and total aerosol volume V_t of a particle ensemble, described by a lognormal distribution, are given by

$$A_t = \int_0^\infty 4\pi r^2 n(r) dr = N_t 4\pi r_m^{\,2} \exp\left[2(\ln\zeta)^2\right] \tag{5.2}$$

and

$$V_t = \int_0^\infty \frac{4\pi}{3} r^3 n(r) dr = N_t \frac{4\pi}{3} r_m^{\,3} \exp\left[\frac{9}{2}(\ln\zeta)^2\right] \tag{5.3}$$

From in situ optical particle counter measurements of the integral size distributions *Pinnick et al.* [1976] recommended the typical parameter values for background sulfate aerosols as N_t=10 cm^{-3}, r_m=0.0725 μm, and ζ=1.86, corresponding to a surface area density of A_t=1.43 $\mu m^2 cm^{-3}$.

Using the geometric volume scale, (4.1)-(4.3), the number of particles n_i in each size bin per unit air volume (or per kg air) is

$$n_i = n(r_i)\Delta r_i = \frac{N_t \left(\frac{2}{f+1} \right)^{1/3} \left(f^{1/3} - 1 \right)}{\sqrt{2\pi}\ln\zeta} \exp\left[-\frac{(\ln r_i - \ln r_m)^2}{2(\ln\zeta)^2} \right] \tag{5.4}$$

Based on balloonborne optical particle counter measurements after major volcanic eruptions *Hofmann et al.* [1983] concluded, that a bimodal lognormal size distribution would better fit the observed distributions, characterized by an increased number of larger particles. *Hofmann and Rosen* [1983] discussed the development of the bimodal distributions, where the background particles start growing into the large mode by condensation of sulfuric acid/water vapor after the injection of sulfur compounds to the stratosphere. At the same time homogeneous nucleation from the gas phase creates new very small particles, which grow by coagulation into the observed small mode. The loss of particles from the large mode by gravitational sedimentation seems to be compensated by continuous condensational growth from the small mode for several months after the eruptions. *Jäger and Hofmann* [1991] presented an 8-year temporal evolution in the bimodal lognormal parameters N_t and r_m; the bimodal distributions were also observed on occasions in 1991 at Laramie, Wyoming, shortly after the Mt. Pinatubo volcanic eruption by *Deshler et al.* [1992].

Refractive indices.

The refractive index is given by $m(T,w_s,w_n,\lambda)=m_R(T,w_s,w_n,\lambda)+i\ m_I(T,w_s,w_n,\lambda)$ as function of temperature, chemical composition, and wavelength of the light λ. The imaginary part m_I is almost vanishing and has been set to 10^{-7} in all calculations. In order to calculate the refractive index at an arbitrary temperature the Lorentz-Lorenz formula must be used [e.g. *Steele and Hamill*, 1981]

$$m_R(T,w_s,w_n,\lambda)=\sqrt{\frac{1+2A\rho(T,w_s,w_n)}{1-A\rho(T,w_s,w_n)}} \tag{5.5}$$

where A is the refractivity of the solution and ρ is the density. For binary sulfuric acid solution particles the measured values, at 300 K, of the real and imaginary parts of m are tabulated by *Palmer and Williams* [1975] at different wavelengths and sulfuric acid weight fractions, thus

$$A=\frac{m_R^{\,2}(T=300K,w_s,\lambda)-1}{[\,m_R^2(T=300K,w_s,\lambda)+2]\ \rho(T=300K,w_s)} \tag{5.6}$$

In the following optical calculations for the liquid particles of binary and ternary composition, the refractive index model by *Luo et al.* [1996] and *Krieger et al.* [2000] have been used, valid in the range $0.05 < w_s+w_n < 0.7$, $185\ K < T < 370\ K$, $350\ nm < \lambda < 2000\ nm$. In this model, the refractivity of the solution is calculated as a linear superposition of molar refractivities of sulfuric acid, nitric acid, and water. In Figure 5.1 is shown an example of refractive indices of STS particles at 189 K and a typical lidar wavelength λ=532 nm.

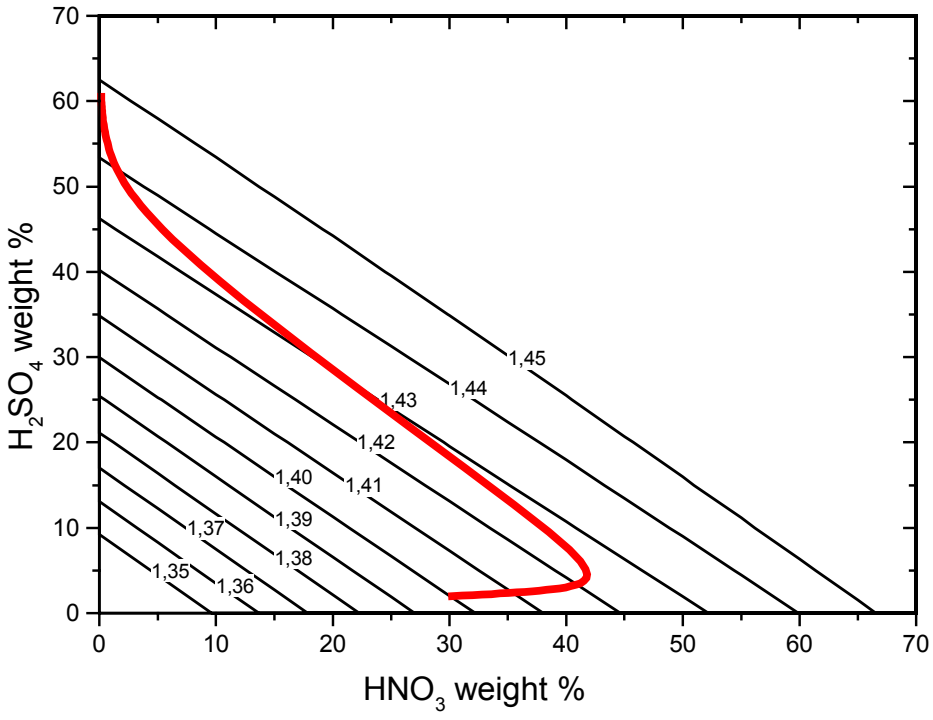

Figure 5.1 Contour plot (black curves) of the real-part refractive index of STS, calculated by the *Krieger et al.* [2000] model at T=189 K, λ=532 nm. For comparison is shown as the red curve the composition of STS particles in the temperature range 185-200 K as also displayed in the right panel of Figure 3.11.

Aerosol backscatter ratio and extinction coefficients.

The sulfate aerosols and type 1b PSC particles are assumed to be supercooled sulfuric acid or ternary solution liquid droplets of *spherical* shape, which allows Mie scattering theory to be applied. An often used quantity for comparison between microphysical simulations and optical measurements by lidar and backscatter sondes is the backscatter ratio $\Re$, i.e. the ratio between the total volume backscattering coefficients from particles (B) and air molecules (B_{Ray}) to the molecular backscatter

$$\Re = \frac{B + B_{Ray}}{B_{Ray}} \tag{5.7}$$

The molecular, or Rayleigh, volume backscattering coefficient [$m^{-1}sr^{-1}$], is calculated from

$$B_{Ray} = n \frac{d\sigma}{d\Omega_{Ray}} = \frac{P_a}{kT} \frac{d\sigma}{d\Omega_{Ray}} \tag{5.8}$$

where $d\sigma/d\Omega_{Ray}$ is the Rayleigh differential scattering cross section, n is the number density of air molecules, P_a the air pressure, T the air temperature, and k Boltzmann's constant. An expression for $d\sigma/d\Omega_{Ray}$ is given by *Nicolet et al*. [1982]

$$\frac{d\sigma}{d\Omega_{Ray}} = \frac{2.346\ 10^{-33}\ m^2\ sr^{-1}}{\lambda^{4+x}} (1 + \cos^2\theta)$$

$$x = 0.074 + \frac{0.05}{\lambda} - 0.084 \tag{5.9}$$

where λ is the incident light wavelength (in μm), and θ is the backscatter angle from the forward direction (180° for the lidar, and 173° for the University of Wyoming backscatter sonde).

The volume backscattering coefficient B of an ensemble of particles [$m^{-1}sr^{-1}$], characterized by a differential size distribution n(r), is calculated from [*Bohren and Huffman*, 1983]

$$B = \int_0^\infty n(r)\, \pi r^2\, Q_b(r, \lambda, \theta, m[T, w_s, w_n, \lambda])\, dr$$

$$= \int_0^\infty n(r) \frac{d\sigma_b}{d\Omega}(r, \lambda, \theta, m[T, w_s, w_n, \lambda])\, dr \tag{5.10}$$

where Q_b is the Mie backscattering efficiency factor, which is dependent on particle radius r, incident light wavelength λ, backscatter direction θ, and the refractive index $m(T,w_s,w_n,\lambda)$ of the particles; this quantity itself being dependent on the temperature, particle composition, and wavelength as explained above. The Mie particle backscattering differential cross section $d\sigma_b/d\Omega$ [m^2sr^{-1}] is defined as $d\sigma_b/d\Omega = \pi r^2\, Q_b$.

Likewise, the aerosol extinction coefficient E [m^{-1}] of an ensemble of particles, characterized by a differential size distribution n(r), is calculated from

$$E = \int_0^\infty n(r)\,\pi r^2\,Q_e(r,\lambda,m[T,w_s,w_n,\lambda])\,dr$$

$$= \int_0^\infty n(r)\,\sigma_e(r,\lambda,m[T,w_s,w_n,\lambda])\,dr \qquad (5.11)$$

where Q_e is the Mie extinction efficiency factor and σ_e is the extinction cross section [m^2], $\sigma_e=\pi r^2 Q_e$.

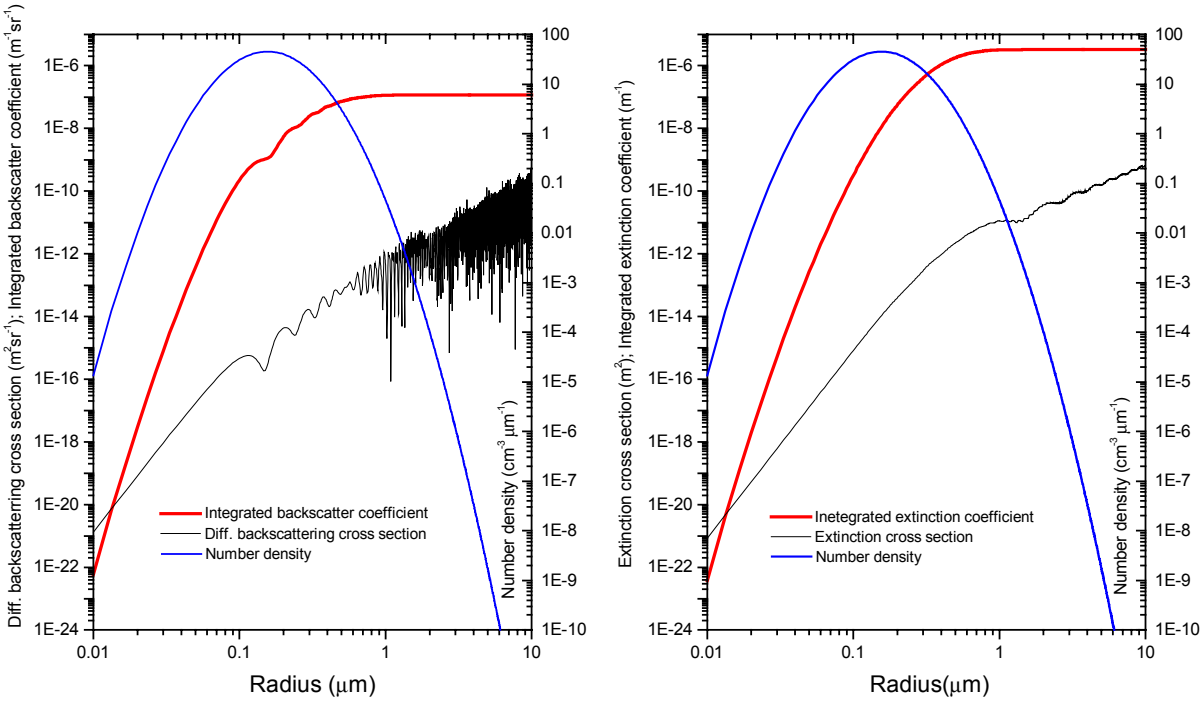

Figure 5.2 Differential backscattering cross section $d\sigma_b/d\Omega$ at 532 nm, 180°, and extinction cross section σ_e at 1000 nm as functions of radius (black curves, left and right panel), calculated for STS particles (w_s=0.1, w_n=0.4) at T=189 K. The blue curve shows a typical differential lognormal size distribution n(r) (N_t=10 cm^{-3}, r_m=0.2 µm, ς=1.65) which has been used to calculate the integrated volume backscattering coefficient B(r) and extinction coefficient E(r) (where r is the upper integration limit in (5.10) and (5.11)) (red curves, left and right panel).

Figure 5.2 shows examples of calculated backscatter (λ=532 nm, 180°) and extinction (λ=1000 nm) coefficients, calculated for STS particles described by a lognormal size distribution (blue curve). The black curves show the differential backscatter cross section and extinction cross section and the red curves the backscatter B(r) and extinction coefficient E(r), calculated as functions of the upper integration limit in (5.10) and (5.11). From these curves it can be seen, that mainly the particles in size range from ~ 0.2 µm to ~ 1 µm contribute to the backscattering and extinction. For reference, the optical calculations for this example give $E=3.28\cdot10^{-6}$ m^{-1} and $B=1.18\cdot10^{-7}$ $m^{-1}sr^{-1}$ using (λ=1000 nm, m_R=1.4181) and (λ=532 nm, m_R=1.4340), respectively. At T=189 K, P_a=35 hPa, λ =532 nm, and θ=180°, $B_{Ray}=8.11\cdot10^{-8}$ $m^{-1}sr^{-1}$ whereby the backscatter ratio $\Re_{532nm}$=2.45.

6. Microphysical and optical model calculations.

Fixed cooling rate simulations.

A few simulation results will be presented to display basic features of the microphysical and optical models and to compare the Lagrangian and Eulerian model versions. In these simplified simulations particles at 35 hPa are cooled linearly in time from 225 K to 185 K and subsequently heated again to 225 K. This temperature span will induce phase changes among the particles. An initial lognormal size distribution (5.1) of sulfate aerosols at 225 K with N_t= 10 particles/cm^3, r_m=0.0725 μm, and ς=1.86 has been assumed together with H_2O=5 ppmv and HNO_3=10 ppbv in the gas phase. 500 size classes or size bins have been used in these simulations.

Figures 6.1 and 6.2 (and 6.3) are of the same type, showing various model-calculated variables in 6 panels, using respectively the Lagrangian and Eulerian model version. The **upper left panel** shows the temperature (black), NAT condensation temperature (green), and ice frost point temperature (blue). The condensation temperatures are calculated corresponding to the actual gas phase concentrations. When condensation takes place and removes HNO_3 and H_2O from the gas phase, T_{NAT} and T_{ice} decrease and become equal to the air temperature when NAT, respectively ice particles, are in equilibrium with the gas phase. The **middle left panel** shows the backscatter ratio ℜ at 532 nm (red) and the extinction coefficient E at 1000 nm (black), and the **lower left panel** shows the gas phase mixing ratios and total mixing ratios of HNO_3 (green), H_2O (blue), and H_2SO_4 (red). The **upper right panel** shows the radius of particles in each size class, red curves for liquid and blue curves for solid particles (Lagrangian model), or the mean radii of the different particle types (Eulerian model). The **middle right panel** shows the volumes of different types of particles: red: STS type 1b PSC (sulfate aerosols); green: solid type 1a PSC; blue: solid type 2 PSC, magenta: solid SAT particles, and black: total volume. The **lower right panel** shows the nitric acid weight fractions in the different size classes (black) (only the Lagrangian version), the volume averaged nitric acid weight fraction (blue), and volume averaged sulfuric acid weight fraction (red) in all particles.

It should be noticed that the optical calculations are not reliable for solid particles since Mie scattering theory has been applied for the calculations, assuming spherical particles. The 'noise' in the backscatter calculations in the Lagrangian model reflects the inhomogenity in particle compositions being dependent on radius in contrast to the Eulerian model.

In the Lagrangian model (Figure 6.1) the STS particles start growing when the temperature drops below the STS threshold. The Kelvin barrier prevents the smallest particles ($r < \approx 0.008$ μm) from growing (upper right panel). For the smallest among the activated particles show a fast increase in size, quickly obtaining equilibrium with the gases phase while the larger particles increase their size more slowly. At temperature roughly 3 K below T_{ice} (upper left panel) ice particles (type 2 PSC) freeze out among those particles larger than ≈ 1 μm, growing to radii larger than 10 μm and volumes larger than 100 μm^{3}cm^{-3} (middle right panel). When temperature increases the excess ice evaporates and type 1a PSC particles with radii of a few μm are leased. Further temperature increase leads to an evaporation of NAT, and SAT particles appear with very small volumes. The SAT particles exist until temperatures are above ≈ 210 K when these particles melt. The lower right panel shows that nearly all gas phase HNO_3 is taken up by the solid particles and

also a substantial fraction of the H_2O in ice particles. When small STS and solid particles co-exist right after the formation of type 2 PSC particles, the liquid particles become subsaturated and start evaporating, transferring HNO_3 to the solid type particles. The evaporation is fastest among the smallest liquid particles. The lower right panel shows that the smallest liquid particles obtain the highest HNO_3 weight fraction during cooling. When type 1a PSC particles exist, the HNO_3 weight fraction of these particles corresponds to the NAT weight fraction of 0.538.

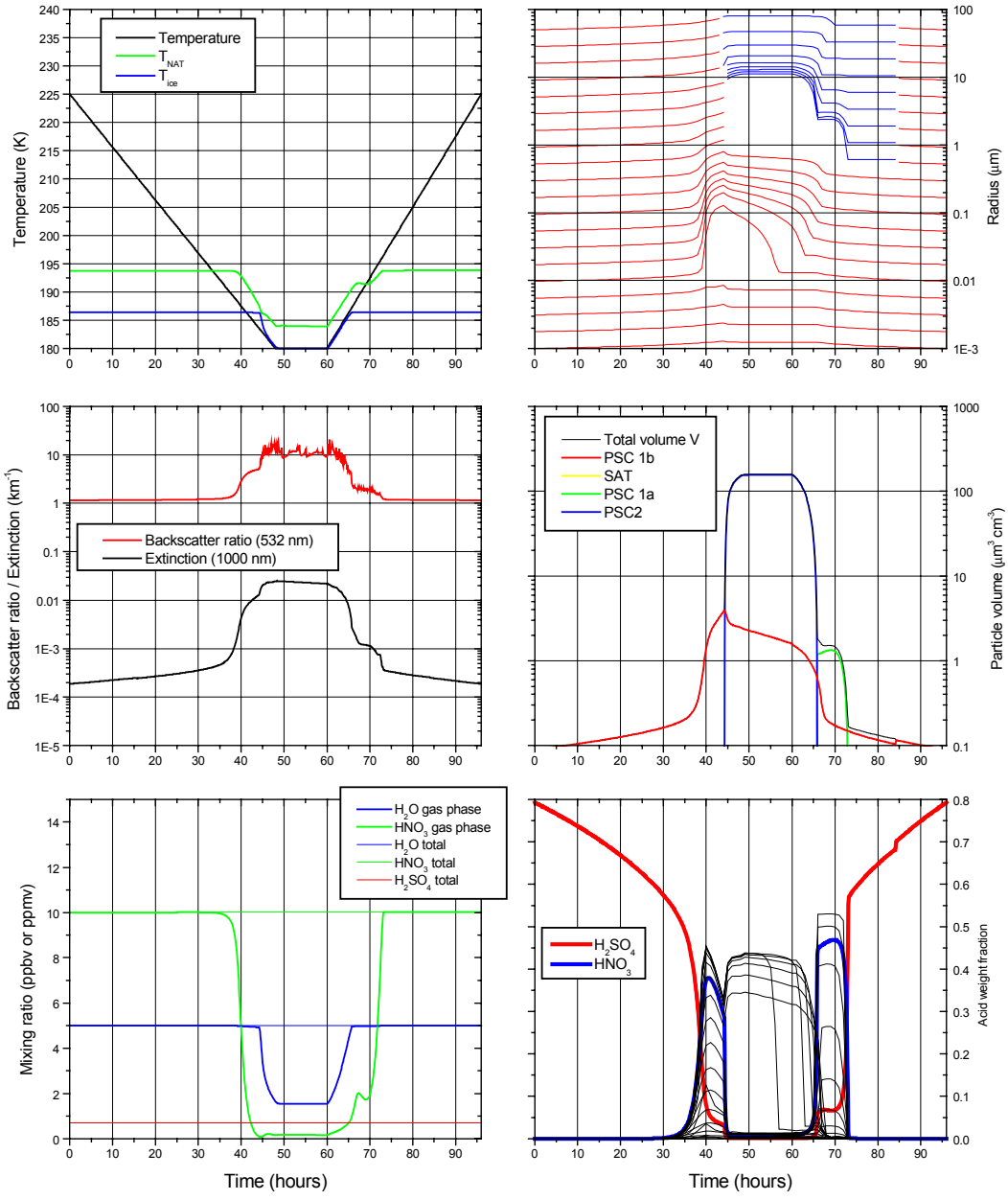

Figure 6.1 Lagrangian model results for the idealized linear cooling/heating simulation. See text for further description of the results in the six panels.

.

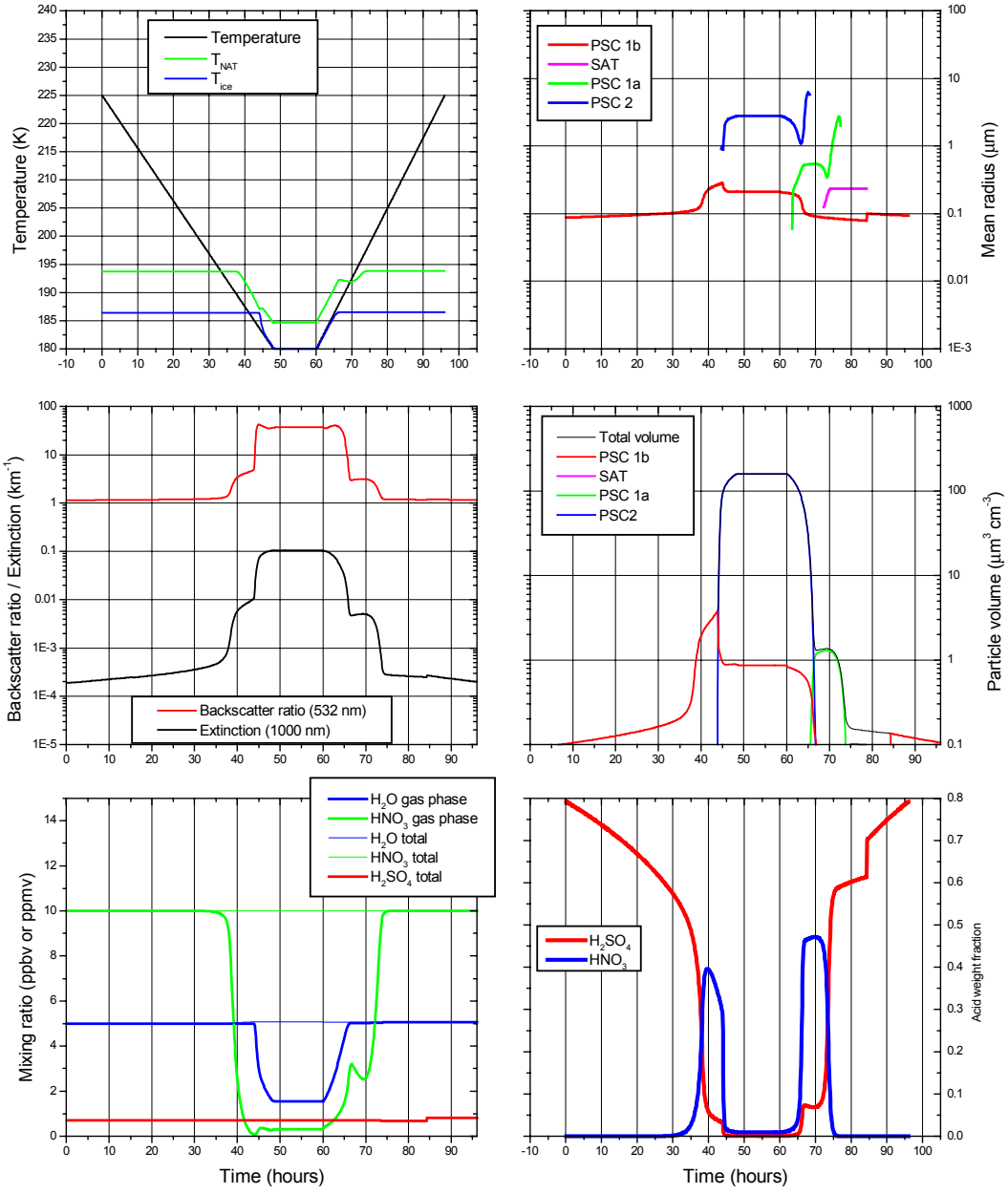

Figure 6.2 Eulerian model results for the idealized linear cooling/heating simulation. See text for further description of the results in the six panels.

Results from the same simulation using the Eulerian model version is shown in Figure 6.2. It appears from the two plots that the two model versions calculate nearly the same integral properties (particle volumes, average particle compositions, and gas phase mixing ratios). The main difference is the behavior of the liquid particles after the ice particle formation. In this model version the liquid particles are assumed to obtain instantaneous equilibrium with the gas phase which is the reason for the fast drop in liquid particle volume (middle right panel). The reason for the increase in mean particle radius among the type 1a and type 2 PSC particles just before their disappearance is that the smallest particle loose their NAT and excess ice shells first, and only

the largest particles in the distribution will remain for the longest time (this can also be seen in the upper right panel in Figure 6.1).

Airparcel trajectory calculations.

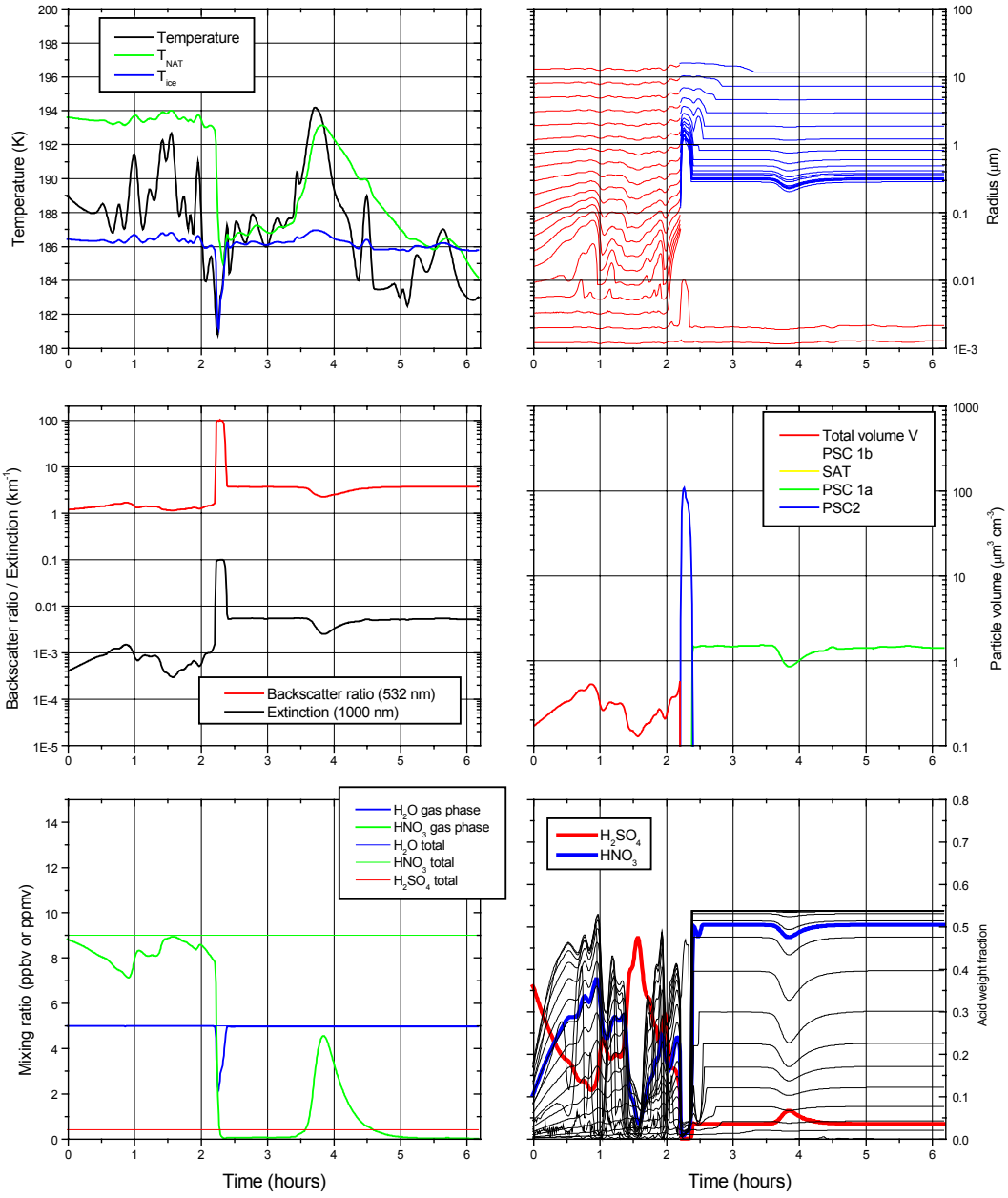

Figure 6.3 Same as Figure 6.1 except that an isentropic PSC simulation (Lagrangian model) has been performed using the temperature data from *Carslaw et al.* [1998, their Figure 2].

An example of an isentropic (constant potential temperature) airparcel trajectory simulation is shown in Figure 6.3 (Lagrangian model version). The temperature history has been adopted from *Carslaw et al.* [1998], derived from "semi-Lagrangian" airborne lidar measurements of PSC formation in leewaves over the Norwegian mountains. Very strong temperature fluctuations were observed where the temperature at time 2.25 hours dropped more that 5K below the ice frost point (upper left panel in Figure 6.3). In this model version this causes nearly all activated STS particles to freeze into ice (upper right panel). Subsequently the temperatures increase above T_{ice} but remain below T_{NAT} for nearly the rest of the simulation. This will cause the release of a large number of small type 1a PSC particles.

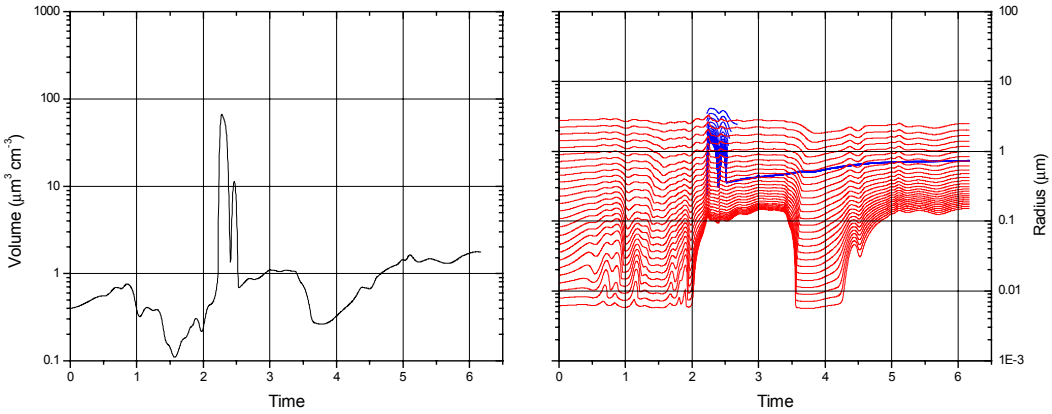

Figure 6.4 Model results of the same air parcel temperature history as in Figure 6.3 by the *Carslaw et al.* [1998] model (A. Tsias, private communication 1998). Left panel is the total particle volume (compare with Figure 6.3 middle right panel), right panel the liquid (red) and solid (blue) particle radii in 25 size bins (compare with Figure 6.3, upper right panel).

Figure 6.4 shows for comparison the same simulation by the *Carslaw et al.* [1998] model. The main difference between the two models is the freezing of STS particles and subsequent NAT nucleation. In the Carslaw et al. model nearly all liquid particles have been assumed to freeze as the temperature drops below T_{ice} around time 2.25 hours. However, after the temperature subsequently increases, nearly all frozen particles are returned to the liquid state and only 2% of the ice particles are assumed to serve as sites for NAT nucleation (cf. Figure 2.5 and the related discussion in Chapter 2 about the breaking of the STS film surrounding the ice enclosure). Before freezing the two models simulate nearly the same behavior of the liquid particles and the two models generate nearly the same ice particle volumes.

Synoptic scale PSC calculations.

The Eulerian model version been used for large-scale (hemispheric) simulations of PSC. In these simulations the temperature development is taken from airparcel trajectories in a given winter (the cold NH-winter 1995/96 has been used), based on ECMWF analysis. The PSC model is run in a large number of boxes (app. 15000 trajectories, distributed over 9 altitude levels where PSCs could occur). The trajectories have been calculated in the following way: backward and forward trajectories have been initiated, starting in mid-winter (23 January) on a regular grid inside the polar vortex

at each of the 9 vertical levels. On each level app. 1600 boxes are evenly distributed within the polar vortex on 23 Jan. Going backward (to beginning of December 1995) and forward in time (to beginning of March 1996) these boxes spread out somewhat, but still remain fairly evenly distributed inside the polar vortex. Each box is initialized in the beginning of December with gas phase HNO_3 and H_2O mixing ratios, assuming at this time that the particles are in the liquid phase (stratospheric sulfate aerosols or type 1b PSC). The trajectory temperatures are used as input to the microphysical box model to calculate PSC properties (e.g. size distributions, surface areas, gas phase concentrations of HNO_3 and H_2O) in each box throughout the winter. Thereby, a mapping is generated of e.g. surface area on an uneven grid (corresponding to the actual positions of each box), but still forming a fairly well filled-out area inside the vortex throughout the winter.

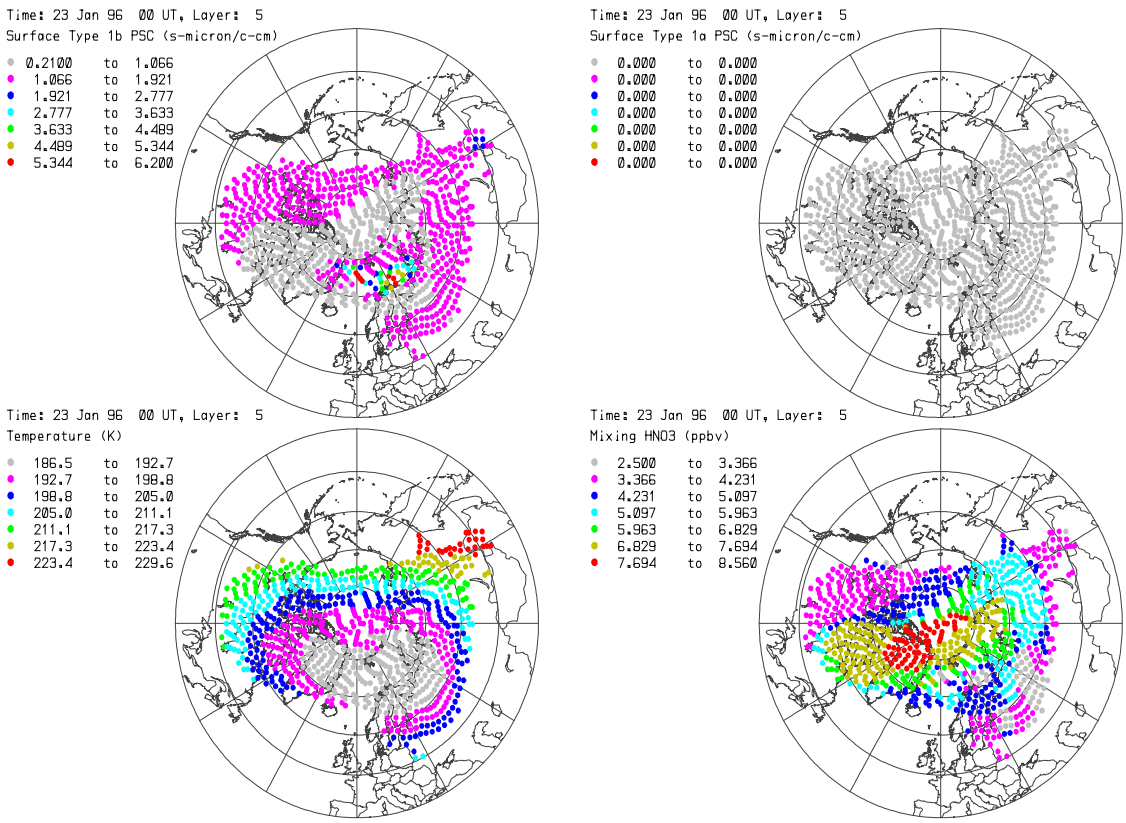

Figure 6.5 Calculated surface area densities of type 1b PSC (upper left panel) together with gas phase HNO_3 (lower right) on 23 January 1996, 12.00 UT at model level 5. The lower left panel shows the temperature field.

An example of the hemispheric simulation is show in Figure 6.5 above, giving the temperature and gas phase HNO_3 fields together with the calculated surface areas of type 1b PSCs on 23 January 1996 at a specific model level (app. 510 k potential temperature).

The intention of this model development is two-fold. First, a direct comparison can now be made between model calculated large-scale PSC and gas phase features and satellite measurements. Secondly, PSC observations from a specific location can be simulated throughout a give winter season.

Previous usage the PSC simulation models.

The PSC and aerosol microphysical and optical simulation models have been used (coupled to larger atmospheric chemistry models), cf. *Dahlback et al.* [1994], *De Rudder et al*., [1996], *Floisand et al*., [1996], *Fonteyn and Larsen* [1996], *Lutman et al*., [1994, 1997]. *Larsen* [1994], *Larsen et al*., [1994, 1997, 2000], *Rivière et al.,* [2000], *Tie et al*., [1996, 1997], *Tourpali et al*. [1997], and *Vaughan et al*. [1994].

7. Description of the Fortran 90 computer code.

Structure of the computer codes.

This chapter gives a description of the Fortran90 computer codes holding the PSC microphysical and optical models. The two model versions, the Lagrangian and the Eulerian models, are described separately below. Both versions are box models, each provided as a single Fortran subroutine (SUBROUTINE PSCBOX) to be called at each time step by the surrounding driving atmospheric model. The calling model is assumed to specify how temperature and pressure change with time, affecting the box in which the aerosol and PSC particles form. The surrounding model will also calculate any heterogeneous chemical reactions taking place on the particle surfaces, derived from the particle size distributions, provided by the PSC box model. The driving model may also call a single subroutine (SUBROUTINE SAOPT), which is common for both the Lagrangian and Eulerian versions, to calculate aerosol backscatter and extinction coefficients if needed. The optical model (SUBROUTINE SAOPT) is described separately below.

The box model subroutines are provided together with all necessary microphysical, thermodynamic, and optical subroutines and functions in a single file (PSCBOX.FOR), all written in standard Fortran90.

The examples of PSC simulations in chapter 6 have been calculated by a driving program, called PSCMODEL. This is an independent program, specially designed to perform relatively simple simulations of PSC formation, and the program calls (drives) the SUBROUTINE PSCBOX. Basically, PSCMODEL can be used to set up different temperature and pressure developments to simulate and study how PSC and aerosol particles form and develop. Optical calculations can also be performed in connection with PSCMODEL runs, but no heterogeneous chemical reactions are calculated by PSCMODEL. The simulations to be performed are specified in a simple self-explaining ASCII input file, described below. PSCMODEL is provided in a single file (PSCMODEL.FOR). PSCMODEL is also written in standard Fortran90 and should be able to be compiled (together with the routines from PSCBOX.FOR) to run on any computer. PSCMODEL provides output as ASCII files, which can be analyzed by any graphics program package capable of plotting column styled data files.

It should be noticed that PSCMODEL is not used when the PSC box model is incorporated in larger atmospheric chemistry or trajectory models.

Executable versions of PSCMODEL can also be provided, running under Microsoft Windows95 or WindowsNT. The exe versions utilize a graphical menu driven interface whereby the progress of the simulation can be viewed. An independent executable program, also running under Windows95 or WindowsNT, can be used to analyze output files, produced by PSCMODEL.

Lagrangian PSCBOX model version

```
SUBROUTINE PSCBOX(
                      DTIME,
                      NBINS,NWORK,
                      TAIR,PAIR,PPWV,PPNA,
                      ND,PAR_TYPE,
                      MCS,MCN,MCW,
                      PTSIZE,WORK)
*****************************************************************************


     Input/output variables:

     INTEGER NBINS,NWORK,PAR_TYPE(NBINS)
     REAL(KIND=4)
             DTIME,TAIR,PAIR,PPWV,PPNA,
             ND(NBINS),
             MCS(NBINS),MCN(NBINS),MCW(NBINS),
             PTSIZE(NBINS,3),WORK(NBINS,NWORK)

     Input:
         DTIME:    (s)             Integration time step
         NBINS:                    Number of particle radii bins
         NWORK:                    2nd dimension of work array WORK
         TAIR:     (K)             Ambient air temperature
         PAIR:     (Pa)            Air pressure
         ND:       (part./kg air)  Number density of aerosol particles

     Input/output:
         PPWV:     (Pa)            Partial water vapor pressure
         PPNA:     (Pa)            Partial nitric acid vapor pressure
         PAR_TYPE                  Particle type identifier:
                                   0:  Liquid sulfuric acid or
                                       supercooled ternary solution particle
                                       (sulfate aerosol or STS type 1b PSC)
                                   1:  Solid sulfuric acid tetrahydrate particle;
                                       i.e. no HNO3 or excess water (SAT particle)
                                   2:  Solid nitric acid trihydrate particle;
                                       i.e. HNO3 (NAT) but no excess ice (type 1a PSC)
                                   3:  Solid ice particle; i.e. holding excess ice
                                       (type 2 PSC)
         MCS:      (kg/part.)      H2SO4 condensed mass per particle
         MCN:      (kg/part.)      HNO3  condensed mass per particle
         MCW:      (kg/part.)      H2O   condensed mass per particle
         PTSIZE:   (m,m**2,m**3)   Particle radii, surface, volume

     Work array:
         WORK:                     Work array (allowed to be changed)


     This subroutine calculates the particle size distributions and chemical
     composition in an ensemble of liquid and frozen stratospheric aerosols
     and polar stratospheric clouds (PSC) in a SINGLE point in space (box) and time.
     Individual box models can be placed in grid-points of a larger model,
     or used in airparcel trajectory calculations.
     The placement of the box-model within a larger calling
     model (geographical/vertical) is referred to as the location of the
     box-model.

     Basically, two types of stratospheric particles are modeled by this
     subroutine:      liquid and solid particles.

     The liquid particles are stratospheric sulfate aerosol particles which,
     at low temperatures, take up HNO3 and H2O, changing the composition into
     supercooled ternary solutions (STS; HNO3/H2SO4/H2O), also referred to as
     type 1b PSCs. The subroutine allows for simulation of non-equilibrium uptake
     of HNO3 in fast cooling/heating events (e.g. mountain lee-waves), emplying
     a radius dependent chemical composition of the particles.

     The solid particles are grouped into three categories, depending on the
     chemical composition. The available water in each solid particle is assumed
     to be bound by 4 H2O molecules to each one H2SO4 molecule, forming sulfuric
     acid tetrahydrate (SAT), and by 3 H2O molecules to each one HNO3 molecule,
     forming nitric acid trihydrate (NAT). Any H2O molecules left not bound in
     hydrates, are assumed to form water ice (excess ice).

     Particles with excess ice are classified as type 2 PSCs.
     Particles with no excess ice but holding HNO3 (NAT) are
               classified as type 1a PSCs.
```

```
Particles with no excess water and no HNO3 (NAT) are
          classified as solid stratospheric aerosols (SAT particles).

The variable PAR_TYPE gives on exit the particle type for each radius class.

At each location the box model takes as input the ambient air state variables:
temperature (TAIR), pressure (PAIR), partial pressure of water vapor (PPWV),
and partial pressure of nitric acid vapor (PPNA). The partial pressures are
changed on exit according to the evaporation/condensation taking place.

The subroutine calculates the time dependent radius (PTSIZE) and physical
phase (PAR_TYPE) of each particle, holding the number of particles per kg. air
(ND) in each radius class fixed (Lagrangian approach in radius space).
The mass of condensed H2SO4, HNO3, and H2O per particle (chemical composition)
is calculated in each radius class due to condensation/evaporation, assuming
a constant H2SO4 content (MCS, MCN, and MCW).

The subroutine uses adjustable array dimensions of all arrays. The parameter
NBINS and the arrays in the argument list of the subroutine must be set and
dimensioned (cf. above) in the calling program. Notice that arrays ND, PTSIZE,
MCS, MCN, MCW and PAR_TYPE must be declared, initialized (and advected) for
each location of the box within a larger model.

The particle size array (PTSIZE) can be initialized on a geometrically
increasing volume scale, using subroutine SETBIN by specifying the initial
minimum and maximum radius values and the number of radius classes (NBINS).
The number density array (ND) can thereafter be initialized with e.g. an
initial lognormal size distribution using subroutine LGNDST or subroutine
INITSP. The arrays of condensed mass (MCS, MCN, MCW) can be initialized for
liquid aerosol equilibrium composition using subroutine MTAINI.

The array WORK can be used by the calling program unit between calls
of the subroutine, and the same array WORK can be used at all locations.
```

Lagrangian PSCMODEL version

```
MAIN PROGRAM PSCMODEL_L (PSCMODEL_L.FOR)
     Program used to drive the PSC-box model (Lagrangian version).

     Main program used to run the PSCBOX model in the Lagrangian-radius-space
     version.
     The program file PSCMODEL.FOR must be linked to PSCBOX.FOR holding the
     microphysical, thermodynamical, and optical subroutines of the PSC box model.

     A few lines of code in this program must be changed, depending on
     the computer (operative system) to be used and where input/output files
     are stored. The statements of the program, which have to be changed, are
     preceded by a comment line, starting with 'CMP'.  All instructions in
     comment lines, starting with 'CMP', should be invoked, before compiling
     and running the program. Comment lines starting with 'CMP' are only found
     in this main program file.


     Input/Output files:
     -------------------

     The program uses a simple self-explaining ASCII input file, stored in
     the associated input file directory. The input file can have any name
     with extension '.INP'. Output file names are generated from the applied
     input file name, all with extension .DAT and stored in the associated
     output file directory. The input/output directories must be specified
     in the main program before compiling (cf. CMP comment lines).

     Computing control:
     ------------------

     Two numbers can be set in the input file to control the integration
     of the PSC-model:
         Maximum integration step size (s)

         Integration start and stop time (Days, Hours, Minutes, Seconds);
             when the integration has reached the stop time, the program
             is terminated (in batch mode), or control is transferred to
             the interactive routine (using the interactive mode on PC).

     Output control:
     ---------------

     A number can be set in the input file to control the frequency
     of output from the PSC-model (Days, Hours, Minutes, Seconds).

     Simulation control:
     -------------------

     By changing the input parameters in the input file, various numerical
     experiments regarding the PSC formation can be set up:

     Temperature:
     ------------

     The temperature is calculated from a function of time as

         TAIR(time) = RAMP-function(time)

     The RAMP-function is a continuous piece-wise linear function, specified
     by 4 coordinate pairs: { (ramp time i, temperature i); i=1..4 };
     i.e. the graph of this function is made up of 3 straight line segments
     between the 4 coordinate points. For time values less than ramp time 1,
     the function is constant equal to temperature 1, and for time values
     greater than ramp time 4, the function is constant equal to
     temperature 4. The 4 coordinate pairs are specified in the input file.
     If the RAMP temperature function is to be used, the temperature calculation
     method flag in the input file must be specified as 0 (zero).

     Alternatively, the temperature history may be specified from a
     time table of the temperature. The table must be stored in the input directory
     as an ASCII file with two columns (time,temperature (K)).
     Cubic spline interpolation will be used between the table entries.
     Time values in the table must be strictly increasing.
     The name of this table file is specified in the input file, residing
     in the input directory. If the temperature table is to be used,
     the temperature calculation method flag in the input file must be
     specified as 1 (one). An input table giving three columns
     (time,temperature(K), pressure (Pa)) can also be used, specified by the
```

```
temperature calculation method flag set to 2 (two).

If a temperature input file is used the ramp temperature information in the
input file is ignored. If a ramp temperature function is used the
specification of a temperature table file name is ignored.

The temperature calculations as described above may be overlayed
by adding a sinusoidal temperature oscillation. Amplitude and period
specified in the input file. If no oscillations are to  be used,
specify amplitude AND period equal to zero. To apply a constant temperature
correction, specify the amplitude, and set the period equal to zero.

The units (Days, Hours, Minutes, Seconds) of the time specifications in
the input file and the temperature table file can be set in the input file.
These units are also used for output.

Pressure/Altitude:
------------------

The altitude H (km) and/or potential temperature THETA (K) are specified
in the input file with the following influence:

If H > 0  and  THETA < 0:
    Calculations at constant pressures; pressures are calculated
    using a constant scale height, HSCALE, of 6.5 km, i.e.
                          P = P0 exp(-H/HSCALE),
    where P0 is the surface pressure, and H is the altitude of the
    layer. Value of THETA is ignored (except for the sign of THETA).
If H > 0 and THETA > 0:
    Calculations at nearly constant pressures; however, pressures may
    change isentropically due to sinusoidal temperature oscillations
    as described above. Pressures are calculated as above from H and
    HSCALE with corrections
                    delP = (cp/R) (P/T) delT
    where delT are the temperature oscillations. Value of THETA is ignored
    (except for the sign of THETA).
If H < 0 and THETA > 0:
    Calculations at constant potential temperature. Pressure
    is calculated from the potential temperature as
                     P = P0*(T/THETA)**(1/kappa).
    Value of H is ignored (except for the sign of H).
IF H < 0 and THETA < 0:
    Pressure specified together with temperature as function of time
    in (time,temperature,pressure) file. The temperature calculation
    method flag must be set to 2 (two). Values of H and THETA are ignored
    (except for the sign of H and THATA).

Surface pressure P0 and scale height HSCALE are parameters of the
program.

Model structure:
----------------
The initial values of minimum and maximum particle radius (microns) are specified
in the input file.

Initial values:
---------------

Initial values of water vapor (ppmv) is specified in the input file.

Initial values of nitric acid (ppbv) is specified in the input file.
If a positive value is given, this value is used; if zero is specified,
an observed vertical profile of nitric acid from LIMS-data is used,
(cf. JGR 89,5125,1984), either from a northern (positive latitude)
hemisphere or southern (negative latitude) hemisphere data set.

Initial values of the total number density of sulfuric aerosols (1/ccm)
is specified in the input file. If a positive value is given, this
value is used; if zero is specified, a typical observed Antarctic non-
volcanic vertical profile will be used (cf. Hofmann et al., GRL 13,1252,1986).

Median radius and geometric standard deviation of the initial lognormal
distribution is given in the input file.

Optical calculations:
---------------------
Calculation of liquid particle backscatter ratios and extinction coefficients
(Mie scattering) can be specified by a logical flag in the input file.
Wavelengths are specified as parameters in the main program and
must be set before compilation. The number of size bins must be large
to obtain reliable backscatter values (>500). Further details are given
in the description of SUBROUTINE SAOPT. IF(OPTICS)-ENDIF blocks in the main
```

```
program should also be inspected and changed according to the actual optical
parameters required.


Header:
-------
The first line in the input file is used for header information about
the actual simulation. The information contained in the input file
is stored in the output directory with the same file name as the output
file with extension '.INF'.

All calculations are performed internally in SI units.

Output on files:
----------------
Four data output files are created by the program. All output files
are column ASCII files with data as function of time (time in first
column with units as specified in the input file).
The output file names are generated from the input file name
(e.g. XXXXX.INP) and stored in the specified output file directory:

    Integrated data file                              (XXXXX.DAT)
    Liquid particle radius file                       (XXXXX-RL.DAT)
    Solid particle radius file                        (XXXXX-RS-DAT)
    Liquid particle nitric acid weight fraction file (XXXXX-WN.DAT)

The output files can be used by independent programs  (e.g. Origin,GRAPHER,
Spreadsheets) to produce graphical presentations of time series.
The integrated data output file hold a number of records; one record for
each output time, as is specified in the input file. Each record holds
19 numbers (columns in the file), giving the following values:

A:  Time (Days, Hours, Minutes, Seconds; as specified in the input file)
B:  Temperature  (K)
C:  Total number density of frozen sulfate particles (1/ccm)
D:  Total number density of PSC 1a (NAT) particles (1/ccm)
E:  Total number density of PSC 2 particles (1/ccm)
F:  Saturation ratio of nitric acid over NAT
G:  Saturation ratio of water vapor over ice
H:  Mixing ratio of water vapor (ppmv)
I:  Mixing ratio of nitric acid vapor (ppbv)
J:  Total (gas phase and condensed phase) mix. ratio, water (ppmv)
K:  Total (gas phase and condensed phase) mix. ratio, nitric acid (ppbv)
L:  Ratio of total to initial mixing ratio of water (%)
M:  Ratio of total to initial mixing ratio of nitric acid (%)
N:  Total volume of frozen sulfate particles (micron**3/ccm)
O:  Total volume of PSC 1a particles (micron**3/ccm)
P:  Total volume of PSC 2 particles (micron**3/ccm)
Q:  Total volume of all particles (micron**3/ccm)
R:  Total number density of PSC 1b (STS) particles (1/ccm)
S:  Total volume of PSC 1b (STS) particles (micron**3/ccm)
T:  Sulfuric acid weight fraction liquid PSC 1b aerosols [0;1]
U:  Mean radius liquid PSC 1b aerosols (micron)
V:  Mean radius frozen sulfate aerosols (micron)
X:  Mean radius PSC 1a (micron)
Y:  Mean radius PSC 2 (micron)
Z:  Nitric acid weight fraction liquid PSC 1b aerosols [0;1]
AA: NAT condensation temperature (K)
AB: Ice frost point temperature (K)
AC: Air pressure (hPa)
AD: Total mixing ration of sulfuric acid (ppb)
AE: Optical parameter 1
AF: Optical parameter 2
AG: Optical parameter 3

The radius and nitric acid weight fraction files hold between 39 and
75 columns, giving time and radius (weight fraction) in each radius
size class. If the number of size classes is >74 only every 2nd., 3rd, ..
values is stored. The stepping (DI) in radius class index is determined by
     DI=MAX0(1,NINT(REAL(NBINS)/50.0))
Radius is given in microns.

In addition a file is produced, holding records with the number of particles per kg. air
in each size class (XXXXX-ND.DAT).  The same stepping DI is used in file XXXXX-ND.DAT.
```

Example of input file for the Lagrangian PSCMODEL version.

The following input file specifies the simulation shown in Figure 6.1

```
Constant cooling - heating. PSC model L-version. Homogeneous freezing.
0.001,50.0      Minimum and maximum initial particle radii (microns)
10.0            Max. integration time step (seconds)
h               Time units (D/H/M/S) of the following time specifications and I/O
0.0,    .F.     Integration start time  (D/H/M/S), Start for reset dump file
96.0            Integration stop time (D/H/M/S)
0.1             Time interval between plot/print output (D/H/M/S)
0               Temperature calculation (0: ramp; 1: Temp table; 2: Temp/Press table)
                Temperature table file name
0.0 ,225.0      Ramp time 1 (D/H/M/S), temperature 1 (K)
48.0,180.0      Ramp time 2 (D/H/M/S), temperature 2 (K)
60.0,180.0      Ramp time 3 (D/H/M/S), temperature 3 (K)
96.0,225.0      Ramp time 4 (D/H/M/S), temperature 4 (K)
0.0, 0.0        Temperature sine oscillation period (D/H/M/S); amplitude (K)
5.0             Mixing ratio water vapor, initial value (ppmv)
10.0            Mixing ratio nitric acid, initial value (ppbv);  (IF 0: LIMS-data)
10.0            Number density sulf.aerosols (1/ccm);   (IF 0: Antarctic profile)
0.0725,1.86     Median radius (microns) and geometric std. dev.,  sulfate aerosols
80.00           Latitude
21.79           Altitude (km)
-427.98         Potential temperature (K)
.t.             Optical calculations
3               Particle surface area (2) or volume (3)
```

Eulerian PSCBOX model version

```
SUBROUTINE PSCBOX(
            DTIME,
            THKNES,
            NBINS,
            TAIR,PAIR,PPWV,PPNA,
            NDSA,RHOTER,WSA,WNA,
            NDPSC,PVOL,
            SDNDSA,SDRHOT,SDWSA,SDWNA,
            SDNAPSC,SDPVOL,
            SA,PSC,SEDMNT_SA,SEDMNT_PSC,
            PTSIZE,WORK)

     INTEGER NBINS
     REAL(KIND=4)
            DTIME,
            THKNES,
            TAIR,PAIR,PPWV,PPNA,
            NDSA(NBINS,2),RHOTER,WSA,WNA,
            NDPSC(NBINS,2),PVOL(NBINS,3),
            SDNDSA(NBINS,2),SDRHOT,SDWSA,SDWNA,
            SDNAPSC(NBINS,2),SDPVOL(NBINS,3),
            PTSIZE(NBINS,8),WORK(NBINS,11)
     LOGICAL SA(2),PSC(2),SEDMNT_SA(2),SEDMNT_PSC(2)


     Input:
         DTIME:   (s)            Integration time step
         THKNES:  (m)            Vertical thickness of layer
         NBINS:                  Number of particle radii bins
         TAIR:    (K)            Ambient air temperature
         PAIR:    (Pa)           Ambient air pressure

     Input/output:
         PPWV:    (Pa)           Ambient partial pressure of water vapor
         PPNA:    (Pa)           Ambient partial pressure of nitric acid
         NDSA:    (par/kg air)   Number density of liquid (1b PSC)/
                                                  frozen (SAT) sulfate aerosols
         RHOTER:  (kg/m**3)      Density of sulfuric-nitric acid liquid solution
         WSA:                    H2SO4 weight fraction of ternary solution
         WNA:                    HNO3 weight fraction of ternary solution
         NDPSC:   (par/kg air)   Number density of type 1a and 2 PSC particles
         PVOL:    (m**3/par)     Volume of condensed substance in solid type PSCs
         SDNDSA:  (par/m**3)     Sedimentation flow of aerosol particles
                                 in time interval DTIME
         SDRHOT:  (kg/m**3)      Density of liquid particles falling in from above
         SDWSA:                  H2SO4 weight fraction of liquid particles
                                 falling in from above
         SDWNA:                  HNO3 weight fraction of liquid particles
                                 falling in from above
         SDNAPSC: (par/m**3)     Sedimentation flow of PSC particles in
                                 time interval DTIME
         SDPVOL:  (m**3/par)     Volume of condensed substance in
                                 sedimenting solid type PSC particles
         SA:      (logical)      Indicator of presence of liquid (1b PSC) or frozen aerosol
         PSC:     (logical)      Indicator of presence of PSCs 1a or 2
         SEDMNT_SA:   (logical)  Indicator of sedimentation of liq/frozen aerosols
         SEDMNT_PSC:  (logical)  Indicator of sedimentation of  PSCs 1a or 2

     Work array:
         PTSIZE:  (m,m**2,m**3)  Particle radii, surface, volume, etc.
                                 (not to be changed)
         WORK:                   Work array (allowed to be changed)

*************************************************************************

     This subroutine calculates the particle size distributions and chemical
     compositions in an ensemble of liquid supercooled ternary solution (STS)
     stratospheric particles (type 1b PSC at low temperatures), frozen stratospheric
     sulfate aerosols, and polar stratospheric clouds (PSC) of type 1a and 2 in a
     SINGLE point in space (box) and time. Individual PSC-box models can be placed in
     grid-points of a larger model, or can be used for air parcel trajectory
     calculations, or can be stacked to form a column model. The placement of the
     box-model within a larger model (geographical/vertical) is referred to as the
     location of the box-model.

     At each location the PSC-box model takes as input the ambient air state
```

```
variables: temperature (TAIR), pressure (PAIR), partial pressure of water
vapor (PPWV), and partial pressure of nitric acid vapor (PPNA).

The particle size distribution of each particle type is divided into a number
of bins (NBINS) on a geometrically increasing volume scale. It is required,
that NBINS > 2. NBINS must be the same for all locations of the PSC-box model.

The number density (ND - particles per unit air mass), i.e. the
the particle size distributions, are stored in the following arrays:
NDSA(i,1) , i=1,...NBINS    Liquid sulfate aerosols which, at low temperatures,
                            take up nitric acid and water, turning into
                            supercooled ternary solution Type 1b PSC
NDSA(i,2) , i=1,...NBINS    Frozen sulfuric acid tetrahydrate particles (SAT)
NDPSC(i,1), i=1,...NBINS    Nitric acid trihydrate (NAT) type 1a PSC
NDPSC(i,2), i=1,...NBINS    Water ice type 2 PSC
ND-array element no. i holds the particles per unit air mass in the particle
radius interval spanned by bin no. i.

The subroutine calculates the differential size distribution NDSA(i,1)
of liquid ternary sulfuric-nitric acid solution aerosol particles, and the
sulfuric and nitric acid weight fractions (WSA, WNA) of the particles,
assuming the ternary aerosols to be in equilibrium with the water and nitric
acid vapor at an arbitrary ambient atmospheric state, specified as input
(TAIR, PPWV, and PPNA).

The density (RHOTER) of the ternary solution (mass per liquid volume)
and the weight fractions (WSA and WNA) of the same particles in
the previous atmospheric state must be given as input to the subroutine.
The values of RHOTER, WSA, and WNA are recalculated on exit to be used
as input to the subroutine in a subsequent call at the same location in
another state (TAIR, PPNA, or PPWV). In order to perform calculations
on different geographical locations and altitudes (grid points), the
variables RHOTER, WSA, and WNA must be defined at each point.

The PSC 1a particles are assumed to be composed of
k:
1:      A core of frozen sulfuric acid tetrahydrate (SAT)
        A surface shell of nitric acid trihydrate (NAT)

The PSC 2 particles are assumed to be composed of
k:
2:      A core of frozen sulfuric acid tetrahydrate (SAT)
3:      An inner shell of nitric acid trihydrate (NAT)
        A surface shell of water ice

The average volumes per particle of each solid substance type in
the cores and inner shells of the PSCs (i.e. SAT in PSC 1a;
SAT, inner shell-NAT in PSC 2) are calculated in each size bin at each
location. These volume values of condensed substance are stored in the
two dimensional array (PVOL(i,k); i=1,NBINS; k=1,3) at each location with
the substance index k as given above.

The model applies homogeneous volume dependent freezing of ice in HNO3/H2O
supercooled solutions  according to Tabazadeh et al. (1997).
Upon freezing of a STS particle all the nitric acid together with water is
deposited as nitric acid trihydrate (NAT) in a shell surrounding a SAT core.
Hereby a type 2 PSC particle is formed, and the core volume PVOL
is recalculated. Upon heating the type 2 PSC may evaporate the outer ice
shell, turning into a type 1a PSC. Upon further heating the NAT shell of
the type 1a PSC particle will evaporate, whereby the frozen sulfate aerosol
core is released (SAT particle).

Any frozen SAT particles are assumed to melt when the air temperature
is above the SAT melting temperature. SAT melting (deliquescence) upon cooling
(Koop and Carslaw, 1996) can also be simulated if the logical parameter SAT_DELI
is be set to .TRUE. When melting a SAT particle the number density is transferred
from the frozen to the liquid particle category and the equilibrium composition
and ternary density is recalculated.

The logical input/output variables SA(1), SA(2), PSC(1) and PSC(2) can be used
in the calling program to test whether STS, frozen aerosol particles,
type 1a, or type 2 PSCs are present.

The number density of particles (NDSA; NDPSC), the density of STS particles,
(RHOTER), the H2SO4 and HNO3 weight fractions of STS (WSA and WNA), and the
volumes of condensed substances (PVOL) constitute the integration variables
of the model. When the subroutine is called, these variables must hold the
values, calculated by the routine in the previous time step (or the initial
values, cf. below). Upon exit these variables will hold the new values at a
time DTIME later. The new values are calculated by a first order explicit
Euler expression within the routine. The ambient air state variables (TAIR,
PAIR) are assumed to be constant during the time interval DTIME. In order to
```

```
perform calculations on different geographical locations and altitudes (grid
points), these variables must be defined at each point.

Nitric acid and water are taken up or released from/to the air during
condensation/evaporation. On exit new values of gas phase partial pressures
of nitric acid (PPNA) and water (PPWV) are recalculated.

The balance calculations of particle number density and volumes of condensed
substance use as input the sedimentation flow of particles (SDNASA, SDNAPSC).
The variables SDRHOT, SDWSA, and SDWNA hold the values of density, H2SO4, and
HNO3 weight fractions of the liquid particles falling in from the layer above,
and SDPVOL condensed volume of solid particles from the layer above. The
routine will return as output, in the same variables, the flow to be used in
the box-calculations in the layer below.
The logical array SEDMNT_SA(j), SEDMNT_PSC(j) indicate, if there is a
sedimentation flow of particles of type j from the layer above on entry,
and indicate, in the same variable, if there is a sedimentation
flow to the layer below on exit.

Thus, for the calculations in a column, the subroutine should be called
in a sequence from the top-layer to the bottom-layer. At the top layer,
the sedimentation input variables should be set equal to zero; the logical
sedimentation indicator (SEDMNT_SA, SEDMNT_PSC) should be set
to .FALSE., and the calling program should not change the values of
these variables between calls in the column sequence. The sedimentation
variables will hold the fall out of particles in the bottom layer after
the last call of the subroutine in the column sequence. The same array
for storing the sedimentation flows and indicators can be used at
different locations, if the calculations are performed column-wise.

A positive vertical extent (THKNES) of the PSC-box (vertical distance
between layers) must be given as input to the subroutine. This extent
need not be the same, neither at all locations, nor at all times.

The subroutine uses adjustable array dimensions of all arrays.
The parameter NBINS and the arrays in the argument list of the
subroutine must be set and dimensioned (cf. above) in the calling
program.

The minimum and maximum particle radius are given as parameters to
SUBROUTINE SETBIN, which must be called once before any call to PSCBOX
(cf. below). Subroutine SETBIN will store the values of the particle radius,
surface area, and volume of each bin in the array PTSIZE. This array PTSIZE
must be used at all locations, and the array must not be changed between the
calls of subroutine PSCBOX.

The SUBROUTINE INITSP can be used to calculate initial values of particle
number density of a liquid stratospheric sulfuric acid particle ensemble with
an initial log-normal size distribution (parameters given to the subroutine).
Under warmer stratospheric conditions with no PSCs this distribution could
normally be used as initial values of the PSC-box model. The variables RHOTER,
WSA, and WNA can be initialized using SUBROUTINE MTAINI. The arrays NDPSC, PVOL,
NDSA(i,2), and logical flags SA(2) and PSC should initially be set equal to
zero/.false. in this case.

The total particle surface area density of a given particle type can
be calculated by SUBROUTINE SURFCE. The condensed phase mixing ratios
of nitric acid and water can be calculated by SUBROUTINE MIXCON. Para-
meters of log-normal distribution fits to individual particle
distributions can be calculated by SUBROUTINE LGNPAR (cf. below).

The array WORK can be used by the calling program unit between calls
of the subroutine, and the same array WORK can be used at all locations.

All calculations are performed in SI units.

The entire PSC-box model is written in ANSI fortran 90.
```

Eulerian PSCMODEL version

```
MAIN PROGRAM PSCMODEL_E (PSCMODEL_E.FOR)
     Program used to drive the PSC-box model (Eulerian version).

     Main program used to run the PSCBOX model in the Eulerian-radius-space
     version, i.e. using fixed size bins.
     The program file PSCMODEL.FOR must be linked to PSCBOX.FOR holding the
     microphysical, thermodynamical, and optical subroutines of the PSC box
     model.

     A few lines of code in this program must be changed, depending on
     the computer (operative system) to be used and where input/output files
     are stored. The statements of the program, which have to be changed, are
     preceded by a comment line, starting with 'CMP'.  All instructions in
     comment lines, starting with 'CMP', should be invoked, before compiling
     and running the program. Comment lines starting with 'CMP' are only found
     in this main program file.

     Input/Output files:
     -------------------

     The program uses a simple self-explaining ASCII input file, stored in
     the associated input file directory. The input file can have any name
     with extension '.INP'. Output file names are generated from the applied
     input file name, all with extension .DAT and stored in the associated
     output file directory. The input/output directories must be specified
     in the main program before compiling (cf. CMP comment lines).

     Time units.
     -----------
     The model performs all calculations internally in SI units, i.e. time in
     seconds. However, other units for input/output can be required.
     The units (Days, Hours, Minutes, Seconds) of the time specifications in
     the input file and the temperature table file can be set in the input file.
     These units are also used for output.

     Computing control:
     ------------------

     Two numbers can be set in the input file to control the integration
     of the PSC-model:
         Maximum integration step size (s)

         Integration start and stop time (Days, Hours, Minutes, Seconds);
             when the integration has reached the stop time, the program
             is terminated (in batch mode), or control is transferred to
             the interactive routine (using the interactive mode on PC).

     Output control:
     ---------------

     A number can be set in the input file to control the frequency
     of output from the PSC-model (Days, Hours, Minutes, Seconds).

     Simulation control:
     -------------------

     By changing the input parameters in the input file, various numerical
     experiments regarding the PSC formation can be set up:

     Temperature:
     ------------

     The temperature is calculated from a function of time as

         TAIR(time) = RAMP-function(time)

     The RAMP-function is a continuous piece-wise linear function, specified
     by 4 coordinate pairs: { (ramp time i, temperature i); i=1..4 };
     i.e. the graph of this function is made up of 3 straight line segments
     between the 4 coordinate points. For time values less than ramp time 1,
     the function is constant equal to temperature 1, and for time values
     greater than ramp time 4, the function is constant equal to
     temperature 4. The 4 coordinate pairs are specified in the input file.
     If the RAMP temperature function is to be used, the temperature calculation
     method flag in the input file must be specified as 0 (zero).

     Alternatively, the temperature history may be specified from a
```

```
time table of the temperature. The table must be stored in the input directory
as an ASCII file with two columns (time,temperature (K)).
Cubic spline interpolation will be used between the table entries.
Time values in the table must be strictly increasing.
The name of this table file is specified in the input file, residing
in the input directory. If the temperature table is to be used,
the temperature calculation method flag in the input file must be
specified as 1 (one). An input table giving three columns
(time,temperature(K), pressure (hPa)) can also be used, specified by the
temperature calculation method flag set to 2 (two).

If a temperature input file is used the ramp temperature information in the
input file is ignored. If a ramp temperature function is used the
specification of a temperature table file name is ignored.

The temperature calculations as described above may be overlayed
by adding a sinusoidal temperature oscillation. Amplitude and period
specified in the input file. If no oscillations are to  be used,
specify amplitude AND period equal to zero. To apply a constant temperature
correction, specify the amplitude, and set the period equal to zero.


Initial values:
---------------

Initial values of water vapor (ppmv) (same for all layers) is specified
in the input file.

Initial values of nitric acid (ppbv) is specified in the input file.
If a positive value is given, this value is used for all levels; if
zero is specified, an observed vertical profile of nitric acid from
LIMS-data is used, (cf. JGR 89,5125,1984), either from
a northern (positive latitude) hemisphere or southern (negative
latitude) hemisphere data set.

Initial values of the total number density of sulfuric aerosols (1/ccm)
is specified in the input file. If a positive value is given, this
value is used for all levels; if zero is specified, a typical observed
Antarctic vertical profile will be used (cf. Hofmann et al.,
GRL 13,1252,1986).

Median radius and geometric standard deviation of the initial
lognormal distribution is given in the input file (same for all
altitudes).

Model structure:
----------------

The number of layers in the vertical direction is specified in the
input file. A maximum of MAXLAY layers can be used. If a negative
number is specified, the absolute value is used as the number of
layers, but no sedimentation of particles between the layers is
calculated. The layers are numbered from the top to the bottom,
and the top layer is no. 1.

The altitude H (km) and/or potential temperature THETA (K) together with
the layer thickness DL (km or K) are specified in the input file with the
following influence:

If H > 0  and  THETA < 0:
    Calculations at constant pressures; pressures are calculated
    using a constant scale height, HSCALE, of 6.5 km, i.e
                          P = P0 exp(-H/HSCALE),
    where P0 is the surface pressure, and H is the altitude of the
    layer. Value of THETA is ignored (except for the sign of THETA).
If H > 0 and THETA > 0:
    Calculations at nearly constant pressures; however, pressures may
    change isentropically due to sinusoidal temperature oscillations
    as described above. Pressures are calculated as above from H and
    HSCALE with corrections
                    delP = (cp/R) (P/T) delT
    where delT are the temperature oscillations. Value of THETA is ignored
    (except for the sign of THETA).
If H < 0 and THETA > 0:
    Calculations at constant potential temperature. Pressure
    is calculated from the potential temperature as
                     P = P0*(T/THETA)**(1/kappa).
    Value of H is ignored (except for the sign of H).
IF H < 0 and THETA < 0:
    Pressure specified together with temperature as function of time
    in (time,temperature,pressure) file. The temperature calculation
    method flag must be set to 2 (two). Values of H and THETA are ignored
```

```
    (except for the sign of H and THATA).

Surface pressure P0 and scale height HSCALE are parameters of the
program.


Optical calculations:
---------------------
Calculation of liquid particle backscatter ratios and extinction coefficients
(Mie scattering) can be specified by a logical flag in the input file.
Wavelengths are specified as parameters in the main program and
must be set before compilation. The number of size bins must be large
to obtain reliable backscatter values (>500). Further details are given
in the description of SUBROUTINE SAOPT. IF(OPTICS)-ENDIF blocks in the main
program should also be inspected and changed according to the actual optical
parameters required.


Output on files:
----------------

Three types of ASCII output files can be created by the program:

    1:    Historical output files
    2:    Distribution output file
    3:    Vertical profile output file

The output file names are generated from the input file name (e.g.
XXXXX.INP) and stored in the specified output file directory:

HISTORICAL OUTPUT FILE is always created for each layer, named
XXXXX-Hyy.DAT, where yy is the layer number. The historical output files
hold a number of records; one record for each output time, as
specified in the input file. Each record holds the following values:

A:  Time (Days, Hours, Minutes, Seconds; as specified in the input file)
B:  Temperature  (K)
C:  Total number density of frozen sulfate particles (1/ccm)
D:  Total number density of PSC 1 particles (1/ccm)
E:  Total number density of PSC 2 particles (1/ccm)
F:  Saturation ratio of nitric acid over NAT
G:  Saturation ratio of water vapor over ice
H:  Mixing ratio of water vapor (ppmv)
I:  Mixing ratio of nitric acid vapor (ppbv)
J:  Total (gas phase and condensed phase) mix. ratio, water (ppmv)
K:  Total (gas phase and condensed phase) mix. ratio, nitric acid (ppbv)
L:  Ratio of total to initial mixing ratio of water (%)
M:  Ratio of total to initial mixing ratio of nitric acid (%)
N:  Total volume of frozen sulfate particles (micron**3/ccm)
O:  Total volume of PSC 1a particles (micron**3/ccm)
P:  Total volume of PSC 2 particles (micron**3/ccm)
Q:  Total volume of all particles (micron**3/ccm)
R:  Total number density of PSC 1b (STS) particles (1/ccm)
S:  Total volume of PSC 1b (STS) particles (micron**3/ccm)
T:  Sulfuric acid weight fraction liquid PSC 1b aerosols [0;1]
U:  Mean radius liquid PSC 1b aerosols (micron)
V:  Median radius frozen sulfate aerosols (micron)
X:  Median radius PSC 1 (micron)
Y:  Median radius PSC 2 (micron)
Z:  Nitric acid weight fraction LIQUID stratospheric aerosols [0;1]
Z:  Nitric acid weight fraction liquid PSC 1b aerosols [0;1]
AA: NAT condensation temperature (K)
AB: Ice frost point temperature (K)
AC: Air pressure (hPa)
AD: Total mixing ration of sulfuric acid (ppb)
AE: Optical parameter 1
AF: Optical parameter 2
AG: Optical parameter 3
AI: Moleratio


DISTRIBUTION OUTPUT FILES are created, if a non-zero distribution-
dump-frequency is specified in the input file, or if a command
is given interactively for this (PC). The names of the distribution
output files are XXXXX-Dyy.DAT, where yy is the layer number.
The distribution output files holds a number of blocks of records.
A block is written to each distribution output file at each distribution
output time. The first record in a block holds the time (Seconds, Days or
Hours as specified in the input file). Then follows a number of records;
one record for each size bin giving the following values:

A:  Particle radius (micron)
```

```
B:  Differential concentration of liquid sulfate particles (1/micron ccm)
C:  Differential concentration of frozen sulfate particles (1/micron ccm)
D:  Differential concentration of PSC 1 particles (1/micron ccm)
E:  Differential concentration of PSC 2 particles (1/micron ccm)
F:  Differential concentration of all particles (1/icronm ccm)


A VERTICAL PROFILE OUTPUT FILE is created, if a non-zero vertical-dump-
frequency is specified in the input file, or if a command is given
interactively for this (PC). The name of the vertical profile output
files is XXXXX-V.DAT. The vertical profile output file holds a number of
blocks of records. A block is written to the vertical output
file at each vertical output time. The first record in a block holds
the time (Days or Hours; as specified in the input file). Then follows
a number of records; one record for each layer, starting from the
BOTTOM layer. Each record holds the following values:

A:  Altitude (km)
B:  Pressure (hPa)
C:  Temperature  (K)
D:  Total number density of frozen sulfate particles (1/ccm)
E:  Total number density of PSC 1 particles (1/ccm)
F:  Total number density of PSC 2 particles (1/ccm)
G:  Saturation ratio of nitric acid over NAT
H:  Saturation ratio of water vapor over ice
I:  Mixing ratio of water vapor (ppmv)
J:  Mixing ratio of nitric acid vapor (ppbv)
K:  Total (gas phase and condensed phase) mix. ratio, water (ppmv)
L:  Total (gas phase and condensed phase) mix. ratio, nitric acid (ppbv)
M:  Ratio of total to initial mixing ratio of water (%)
N:  Ratio of total to initial mixing ratio of nitric acid (%)
O:  Total surface area density of frozen sulfate particles (æm**2/ccm)
P:  Total surface area density of PSC 1 particles (æm**2/ccm)
Q:  Total surface area density of PSC 2 particles (æm**2/ccm)
R:  Total surface area density of all particles (æm**2/ccm)
S:  Total number density of liquid sulfate particles (1/ccm)
T:  Total surface area density of liquid sulfate particles (æm**2/ccm)
U:  Sulfuric acid weight fraction in LIQUID sulfate aerosols [0;1]
V:  Median radius liquid sulfate aerosols (æm)
X:  Median radius frozen sulfate aerosols (æm)
Y:  Median radius PSC 1 (æm)
Z:  Median radius PSC 2 (æm)
AA: Nitric acid weight fraction in LIQUID sulfate aerosols [0;1]
AB: NAT condensation temperature (K)
AC: Ice frost point temperature (K)
AD: Air pressure (hPa)
AE: Total mixing ration of sulfuric acid (ppb)
AF: Optical parameter 1
AG: Optical parameter 2
AH: Optical parameter 3
AI: Moleratio
```

Example of input file for the Eulerian PSCMODEL version.

The following input file specifies the simulation shown in Figure 6.2

```
Constant cooling - heating, PSC model E version, Homogeneous freezing
0.001, 50.0      Min. max. radius
10.0             Max. integration time step (seconds)
h                Time units (H/D) of the following time specifications and I/O
0.0              Integration start time
96.00            Integration stop time (H/D)
0.1, 0.0, 0.0    Time interval between plot/print output (H/D)
0                Temperature calculation (0: ramp; 1: Temp table; 2: Temp/Press table)
                 Temperature table file name
0.0,225.0        Ramp time 1 (H/D), temperature 1 (K); (IF time 1 < 0: Temp. table)
48.0,180.0       Ramp time 2 (H/D), temperature 2 (K)
60.0,180.0       Ramp time 3 (H/D), temperature 3 (K)
96.0,225.0       Ramp time 4 (H/D), temperature 4 (K)
0.0, 0.0         Temperature sine oscillation period (H/D); amplitude (K)
5.0              Mixing ratio water vapor, initial value (ppmv)
10.0             Mixing ratio nitric acid, initial value (ppbv);  (IF 0: LIMS-data)
10.0             Number density sulf.aerosols (1/ccm);    (IF 0: Antarctic profile)
0.0725,1.86      Median radius (microns) and geometric std. dev.,  sulfate aerosols
80.00, -1        Latitude;  Number of layers (IF < 0: no sedimentation calculations)
21.79, 1.0       Top layer altitude and layer thickness (km)
-575.0, 10.0     Potential temperature and potential temperature decrement (K)
.t.              Optical calculations
```

Optical model.

```
SUBROUTINE SAOPT(OPTICAL_PAR,NBINS,PND,PTSIZE,PAIR,TAIR,
                     WAVEL,REF,OPT,RAY)

     CHARACTER*1 OPTICAL_PAR
     INTEGER NBINS
     REAL    PND(NBINS),PTSIZE(NBINS,3),
             PAIR,TAIR,WAVEL,REFRE(NBINS),BKP,RAY

     Input:
         OPTICAL_PAR             Character flag, indicating calculation of
                                 Molecular volume backscatter coefficient ('B') or
                                 Aerosol extinction coefficient ('E')
         NBINS:                  Number of particle radii bins
         PND:      (par/kg air)  Number density of aerosol particles
         PTSIZE:   (m,m**2,m**3) Particle radii, surface, volume,
                                 (not to be changed)
         PAIR:     (Pa)          Air pressure
         TAIR:     (K)           Ambient air temperature
         WAVEL:    (m)           Incident wavelength
         REF:                    Real part of refractive index

     Output:
         OPT:      (1/m sr)      Particle volume backscatter coefficient OR
                   (1/m)         aerosol extinction coefficient
         RAY:      (1/m sr)      Molecular volume backscatter coefficient


     Subroutine used to calculate the particle volume backscatter coefficient
     OR extinction coefficient of an ensemble of spherical particles, characterized
     by a differential size distribution PND (calculated by SUBROUTINE PSCBOX),
     at a specified incident wavelength (WAVEL). The particles are assumed to be
     characterized by the refractive index (real part) (REF), whereas the imaginary
     part is given as a parameter in the subroutine.
     Depending on the value of the character flag OPTICAL_PAR the backscatter
     coefficient or extinction coefficient is calculated.

     Also the Rayleigh (molecular) volume backscatter coefficient (RAY) is
     calculated at the same wavelength at the specified ambient atmospheric
     state, given by the air pressure (PAIR) and temperature (TAIR).

     The subroutine is intended to be used together with SUBROUTINE PSCBOX
     which calculates the size distribution of liquid stratospheric aerosols.
     Subroutine SETBIN from the PSCBOX package must be called once prior to
     any call to SUBROUTINE SAOPT.

     An angel distribution of the backscattered light is assumed,
     corresponding to the sensitivity angel distribution of the University
     of Wyoming backscatter sonde. Alternatively, the subroutine can easily
     be changed by logical parameter SINGLE_ANGEL to calculate the backscatter
     at a single specific angle.
```

References.

Beyerle, G., H. Deckelmann, R. Neuber, E. Reimer, N.N., Occurrence of frozen sulfuric acid aerosols in the winter polar stratosphere inferred from ground-based polarization lidar observations at Ny-Ålesund, Spitsbergen, paper in preparation for *J. Geophys Res*., 1999.

Biermann, U.M., J.N. Crowley, T. Huthwelker, G.K. Moortgat, P.J. Crutzen, and T. Peter, FTIR studies on lifetime prolongation of stratospheric ice particles due to NAT coating, *Geophys Res. Lett.* 25, 3939-3942, 1998.

Bohren, C.F. and D.R. Huffman, *Absorption and Scattering of Light by Small Particles*, J. Wiley & Sons, New York, 530 pp, 1983.

Carslaw, K.S., B.P. Luo, S.L. Clegg, T. Peter, P. Brimblecombe, and P.J. Crutzen, Stratospheric aerosol growth and HNO3 gas phase depletion from coupled HNO3 and water uptake by liquid particles, *Geophys. Res. Lett., 21*, 2479-2482, 1994.

Carslaw, K.S., B. Luo, and T. Peter, An analytic expression for the composition of aqueous HNO_3-H_2SO_4 stratospheric aerosols including gas phase removal of HNO_3, *Geophys Res. Lett. 22*, 1877-1880, 1995

Carslaw, K.S., T. Peter and S.L. Clegg, Modeling the composition of liquid stratospheric aerosols, *Rev. Geophys. 35*, 125-154, 1997.

Carslaw, K.S., M. Wirth, A. Tsias, B.P. Luo, A. Dörnbrack, M. Leutbecher, H. Volkert, W. Renger, J.T. Bacmeister, and T. Peter, Particle microphysics and chemistry in remotely observed mountain polar stratospheric clouds, *J. Geophys. Res. 103*, 5785-5796, 1998.

Carslaw, K.S., T. Peter, J.T. Bacmeister, and S.D. Eckermann, Widespread solid particle formation by mountain waves in the Arctic stratosphere, *J. Geophys. Res. 104*, 1827-1836, 1999a.

Carslaw, K.S., H. Volkert, P. Haynes, N.R.P. Harris, N. Larsen, G. Amanatidis, Th. Peter, The European Workshop on Mesoscale Processes in the Stratosphere – Overview and outcomes, in K.S Carslaw and G.T. Amanatidis (ed), *Mesoscale processes in the stratosphere, Their effect on stratospheric chemistry and microphysics*, Proceedings of the European workshop 8 to 11 November 1998, Bad Tölz, Bavaria, Germany, Air Pollution Research Report no. 69, European Commission, pp. 1-6, 1999b.

Chang, H-Y. A., T. Koop, L.T. Molina, and M.J. Molina, Phase transitions in emulsified $HNO_3/H_2SO_4/H_2O$ solutions, *J. Phys. Chem. 103*, 2673-2679, 1999

Dahlback, A., P. Rairoux, B. Stein, M. Del Guasta, E. Kyrö, L. Stefanutti, N. Larsen, and G. Braathen: Effects of Stratospheric Aerosols from the Mt. Pinatubo on SAOZ, Brewer and TOMS Measurements at Sodankylä, Finland 1991/92, *Geophys. Res. Lett.,* ***21***, 1399-1402, 1994.

De Rudder, A., N. Larsen, X. X. Tie, G. P. Brasseur and C. Granier, Model study of polar stratospheric clouds and their effects on stratospheric ozone: Part I -Model description, *J. Geophysical Research, 101*, 12567-12574, 1996.

Deshler, T., D.J. Hofmann, B.J. Johnson, and W.R. Rozier, Balloonborne Measurements of the Pinatubo Aerosol Size Distribution and Volatility at Laramie, Wyoming During the Summer of 1991, *Geophys. Res. Lett. 19*, 199-202, 1992.

Deshler, T., B. Nardi, A. Adriani, F. Cairo, G. Hansen, and F. Fierli, Determining the index of refraction of polar stratospheric clouds above Andoya (69°N) by combining size resolved concentration and optical scattering measurements, *J. Geophys Res.*, in press 2000.

Drdla, K., and R.P. Turco, Denitrification through PSC Formation: A 1-D Model Incorporating Temperature Oscillations, *J. Atmos. Chem*., *12,* 319-366, 1991

Drdla, K., *Applications of a Model of Polar Stratospheric Clouds and Heterogeneous Chemistry*, PhD. dissertation, University of California, Los Angeles, 1996.

Fiocco, G., N. Larsen, S. Bekki, C. David, A.R. MacKenzie, T. Peter, A. di Sarra, and S. Spreng: Particles in the stratosphere, cp. 3, in *European Research in the Stratosphere: The contribution of EASOE and SESAME to our current understanding of the ozone layer*, European Commission, 1997.

Fløisand, i., F. Stordal, B. Rognerud, I.S.A. Isaksen, N. Larsen, B.M. Knudsen: Modelled chemical change over Europe during winters 1992-1995, Proceedings of the XVIII Quadrennial Ozone Symposium, 12-21 September 1996, l'Aquila, Italy, p. 711-714, 1996.

Fonteyn, D. and N. Larsen, Detailed PSC Formation in a Two Dimensional Chemical Transport Model of the Stratosphere, *Annales Geophysicae, 14*, 315-328, 1996.

Fuchs, N.A., 1964, *The Mechanics of Aerosols*, Pergamon Press, New York, 408 pp.

Fuchs, N.A., and A.G. Sutugin, Highly dispersed aerosols, in *Topics in Current Aerosol Research*, vol.2, edited by G.M. Hidy and J.R. Brock, Pergamon Press, New York, 157 pp., 1971

Granzhan, V.A. and S.K. Laktionova, The densities, viscosities, and surface tensions of aqueous nitric acid solutions*, Russian J. Phys. Chem. 49*, 1448, 1975.

Goodman, J., O.B. Toon, R.F. Pueschel, K.G. Snetsinger, and S. Verma, Antarctic Stratospheric Ice Crystals, *J. Geophys. Res. 94*, 16449-16457, 1989.

Goodman, J., S. Verma, R.F. Pueschel, P. Hamill, G.V. Ferry, and D. Webster, New evidences of size and composition of polar stratospheric cloud particles, *Geophys. Res. Lett. 24*, 615-618, 1997.

Hamill, P., O.B. Toon, and C.S. Kiang, Microphysical Processes Affecting Stratospheric Aerosol Particles, *J. Atmos. Sci. 34*, 1104-1119, 1977.

Hamill, P., R.P. Turco, and O.B. Toon, 1988, On the Growth of Nitric and Sulfuric Acid Aerosol Particles Under Stratospheric Conditions, *J. Atmos. Chem. 7*, 287-315.

Hamill, P., A. Tabazadeh, S. Kinne, O.B. Toon, and R.P. Turco, On the growth of ternary system $HNO_3/H_2SO_4/H_2O$ aerosol particles in the stratosphere, *Geophys. Res. Lett. 23*, 753-756, 1996.

Hanson, D., and K. Mauersberger, Laboratory Studies of the Nitric Acid Trihydrate: Implications for the South Polar Stratosphere, *Geophys. Res. Lett. 15*, 855-858, 1988.

Hofmann, D.J. and J.M. Rosen, Sulfuric Acid Droplet Formation and Growth in the Stratosphere After the 1982 Eruption of El Chichón, *Science 222*, 325-327, 1983.

Hofmann, D.J., J.M. Rosen, R. Reiter, and H. Jäger, Lidar- and Balloon-Borne Particle Counter Comparisons Following Recent Volcanic Eruptions, *J. Geophys. Res. 88*, 3777-3782, 1983.

Iraci, L.T., A.M. Middlebrook, and M.A. Tolbert, Laboratory studies of the formation of polar stratospheric clouds: Nitric acid condensation on thin sulfuric acid films*, J. Geophys. Res., 100*, 20969-20977, 1995.

Iraci, L.T., T.J. Fortin, and M.A. Tolbert, Dissolution of sulfuric acid tetrahydrate at low temperatures and subsequent growth of nitric acid trihydrate, *J. Geophys. Res. 103*, 8491-8498, 1998.

Jancso, G., J. Pupezin, and W.A. Van Hook, The Vapor Pressure of Ice between $+10^{-2\circ}$ and $-10^{2\circ}$, *J. Phys. Chem. 74*, 2984-2989, 1970.

Jäger, H. and D. Hofmann, Midlatitude lidar backscatter to mass, area, and extinction conversion model based on *in situ* aerosol measurements from 1980 to 1987, *Appl. Opt. 30*, 127-138, 1991.

Kjällman, T., and I. Olovsson, Hydrogen-bond studies. LVIII. The crystal structures of normal and deuterated sulphuric acid tetrahydrate, $(H_5O_2^+)_2SO_4^{2-}$, *Acta Cryst. B28*, 1692-1697, 1972.

Koop, T. and K.S. Carslaw, Melting of $H_2SO_4 \bullet 4H_2O$ Particles upon cooling: Implications for Polar Stratospheric Clouds, *Science 272*, 1638-1641, 1996.

Koop, T., B. Luo, U.M. Biermann, P.J. Crutzen, and T. Peter, Freezing of $HNO_3/H_2SO_4/H_2O$ solutions at stratospheric temperatures: Nucleation statistics and experiments*, J. Phys. Chem. 101,* 1117-1133, 1997a.

Koop, T. K.S. Carslaw, and T. Peter, Thermodynamic stability and phase transitions of PSC particles, *Geophys. Res. Lett. 24*, 2199-2202, 1997b.

Koop, T. H. P. Ng, L.T. Molina, and M.J. Molina, A new optical technique to study aerosol phase transitions: The nucleation of ice from H_2SO_4 aerosols, *J. Phys. Chem. 102*, 8924-8931, 1998.

Krieger, U.K., J.C. Mössinger, B. Luo, U. Weers, and T. Peter, Measurements of the refractive indices of $H_2SO_4/HNO_3/H_2O$ solutions to stratospheric temperatures, *Appl. Optics, submitted,* 2000.

Larsen, N., *Polar Stratospheric Clouds: A Microphysical Simulation Model*, Scientific Report 91-2, Danish Meteorological Institute, Copenhagen, 83 pp., 1991.

Larsen, N. The Impact of Freezing of Sulfate Aerosols on the Formation of Polar Stratospheric Clouds, *Geophys. Res. Lett., 21*, 425-428, 1994.

Larsen, N., B. Knudsen, T.S. Jørgensen, A. di Sarra, D. Fuà, P. Di Girolamo, G. Fiocco, M. Cacciani, J.M. Rosen, and N. Kjome: Backscatter Measurements of Stratospheric Aerosols at Thule During January-February 1992, *Geophys. Res. Lett., 21*, 1303-1306, 1994.

Larsen, N., B.M. Knudsen, J.M. Rosen, N.T. Kjome, R. Neuber, and E. Kyrö: Temperature histories in liquid and solid polar stratospheric cloud formation, *J. Geophys. Res., 102*, 23505-23517, 1997.

Larsen, N., I.S. Mikkelsen, B.M. Knudsen, J. Schreiner, C. Voigt, K. Mauersberger, J.M. Rosen, and N.T. Kjome, Comparison of chemical and optical in-situ measurements of polar stratospheric clouds, *J. Geophys. Res*., 105, 1491-1502, 2000.

List, R.J, *Smithsonian Meteorological Tables*, 6th ed., Smithsonian Institution Press, Washington, D.C., 527 pp., 1951

Luo, B., K.S. Carslaw, T. Peter, and S.L. Clegg, Vapor pressures of H_2SO_4/HNO3/HCl/HBr/H_2O solutions to low stratospheric temperatures, *Geophys. Res. Lett. 22*, 247-250, 1995.

Luo, B., U.K. Krieger, and T. Peter, Densities and refractive indices of $H_2SO_4/HNO_3/H_2O$ solutions to stratospheric temperatures, *Geophys. Res. Lett. 23*, 3707-3710, 1996.

Lutman, E.R., J.A. Pyle, R.L. Jones, D.L. Lary, A.R. MacKenzie, I. Kilbane-Dawe, N. Larsen, and B. Knudsen: Trajectory Model Studies of Cl_x Activation During the 1991/92 Northern Hemispheric Winter, *Geophys. Res. Lett*., 21, 1419-1422, 1994

Lutman, E.R., J.A. Pyle, M.P. Chipperfield, D.J. Lary, I. Kilbane-Dawe, J.W. Waters, and N.Larsen, Three Dimensional Studies of the 1991/92 Northern Hemisphere Winter Using Domain-Filling Trajectories with Chemistry, *J. Geophys. Res.,102*, 1479-1488, 1997.

MacKenzie, A.R., M. Kulmala, A. Laaksonen, and T. Vesala, On the theories of type 1 polar stratospheric cloud formation, *J. Geophys. Res., 100*, 11275-11288, 1995.

MacKenzie, A.R., A. Laaksonen, E. Batris, and M. Kulmala, The Turnbull correlation and the freezing of stratospheric aerosol droplets, *J. Geophys. Res. 103*, 10875-10884, 1998.

Middlebrook, A.M., L.T. Iraci, L.S. McNeill, B.G. Koehler, M.A. Wilson, O.W. Saastad, M.A. Tolbert, and D.R. Hanson, Fourier Transform-Infrared Studies of Thin H_2SO_4/H_2O Films: Formation, Water Uptake, and Solid-Liquid Phase Changes, *J. Geophys. Res. 98*, 20473-20481, 1993.

Meilinger, S., T. Koop, B.P. Luo, T. Huthwelker, K.S. Carslaw, U. Krieger, P.J. Crutzen, and T. Peter, Size-dependent stratospheric droplet composition in mesoscale temperature fluctuations and their potential role in PSC freezing, *Geophys. Res. Lett., 22*, 3031-3034, 1995.

Myhre, C.E.L., C.J. Nielsen, and O.W. Saastad, Density and surface tension of aqueous H_2SO_4 at low temperature, *J. Chem Eng. Data 43*, 617-622, 1998.

Nicolet, M., R.R. Meier, and D.E. Anderson, Radiation fields in the troposphere and stratosphere - II. Numerical analysis, *Planet. Space Sci. 30*, 935-983, 1982.

Palmer, K.F. and D. Williams, Optical Constants of Sulfuric Acid; Application to the Clouds of Venus?, *Appl. Opt. 14*, 208-219, 1975.

Panegrossi, G. D. Fua, and G. Fiocco, A 1-D Model of the Formation and Evolution of Polar Stratospheric Clouds, *J. Atmos. Chem. 23*, 5-35, 1996.

Perry, J.H. (ed.), *Chemical Engineers' Handbook*, McGraw-Hill, New York, 1963.

Peter, Th, C. Brühl and P.J. Crutzen, Increase in the PSC-formation Probability Caused by High-flying Aircraft, *Geophys. Res. Lett. 18*, 1465-1468, 1991.

Peter, T., R. Müller, P.J. Crutzen, and T. Deshler, The lifetime of leewave-induced ice particles in the Arctic stratosphere, 2, Stabilization due to NAT-coating, *Geophys. Res. Lett., 21*, 1331-1334, 1994.

Peter, Th., Microphysics and heterogeneous chemistry of polar stratospheric clouds, Annu. *Rev. Phys. Chem. 48*, 779-816, 1997.

Pinnick, R.G., J.M. Rosen, and D.J. Hofmann, Stratospheric aerosol measurements III: Optical model calculations, *J. Atmos. Sc. 33*, 304-314, 1976.

Poole, L.R, *Airborne Lidar Studies of Arctic Polar Stratospheric Clouds*, Ph.D. dissertation, University of Arizona, 217 pp., 1987.

Poole, L.R. and M. P. McCormick, Airborne lidar observations of arctic stratospheric: Indications of two distinct growth stages, *Geophys. Res. Lett. 15*, 21-23, 1988.

Prenni, A.J., T.B. Onasch, R.T. Tisdale, R.L.Siefert, and M.A. Tolbert, Composition-dependent freezing nucleation rates for HNO_3/H_2O aerosols resembling gravity-wave-perturbed stratospheric particles, *J. Geophys. Res. 103*, 28439-28450, 1998.

Pruppacher, H.R., and J.D. Klett, *Microphysics of Clouds and Precipitation*, 2.ed., Kluwer Academic Publishers, Dordrecht, Boston, London, 954 pp., 1997.

Rivière, E., N. Huret, F.G. Taupin, J.B. Renard, M. Pirre, S. Eckerman, N. Larsen, T. Deshler, F. Lefèvre, S. Payan and C. Camy-Peyret, Role of leewave in the formation of solid PSCs: case studies from February 1997, *J. Geophys Res*., in press, 2000.

Rizi, V., G. Radaelli, G. Visconti, F. Masci, C. Wedekind, B. Stein, F. Immler, B. Mielke, P. Rairoux, L. Woste, M. Del Guasta, M. Morandi, F. Castagnoli, S. Balastri, L. Stefanutti, R. Matthey, V. Mitev, M. Douard, J.P. Wolf, E. Kyrö, M. Rummukainen, and R. Kivi, Trajectory Studies of Polar Stratospheric Cloud lidar Observations at Sodankylä (Finland) during SESAME: Comparison with Box Model Results of Particle Evolution, *J. Atmos. Chem. 32,* 165-181, 1999.

Russel, P.B., T.J. Swissler, M.P. McCormick, W.P. Chu, J.M. Livingston, and T.J. Pepin, Satellite and Correlative Measurements of the Stratospheric Aerosol. I: An Optical Model for Data Conversions, *J. Atmos. Sci. 38*, 1279-1294, 1981.

Schreiner, J., C. Voigt, A. Kohlmann, F. Arnold, K. Mauersberger, and N. Larsen, Chemical analysis of polar stratospheric cloud particles, *Science 283*, 968-970, 1999.

Shibata, T. et al., Polar stratospheric clouds observed by lidar over Spitsbergen in the winter 1994/95: Liquid particles and vertical "Sandwich" structure, *J. Geophys. Res. 102*, 10829-10840, 1997.

Shindell, D.T., D.Rind, and P. Lonergan, Increased polar stratospheric ozone losses and delayed eventual recovery owing to increasing greenhouse-gas concentrations, *Nature 392*, 589-592, 1998.

Solomon, S., Stratospheric ozone depletion: A review of concepts and history, *Rev. Geophysics 37*, 275-316, 1999.

Steele, H.M., and P. Hamill, Effects of Temperature and Humidity on the Growth and Optical Properties of Sulfuric Acid-Water Droplets in the Stratosphere, *J. Aerosol Sc. 12*, 517-528, 1981.

Steele, H.M., and P. Hamill, Effects of Temperature and Humidity on the Growth and Optical Properties of Sulfuric Acid-Water Droplets in the Stratosphere, *J. Aerosol Sc. 12*, 517-528, 1981.

Tabazadeh, A. R.P. Turco, K. Drdla, and M.Z. Jacobson, A study of Type I polar stratospheric cloud formation, *Geophys. Res. Lett. 21*, 1619-1622, 1994.

Tabazadeh, A. and O.B. Toon, The presence of metastable HNO_3/H_2O solid phases in the stratosphere inferred from ER2 data, *J. Geophys. Res*. *101*, 9071-9078, 1996.

Tabazadeh, A., E. J. Jensen, and O.B. Toon, A model description for cirrus cloud nucleation from homogeneous freezing of sulfate aerosols, *J. Geophys. Res. 102*, 23845-23859, 1997a.

Tabazadeh, A., O.B. Toon, and E. J. Jensen, Formation and implications of ice particle nucleation in the stratosphere, *Geophys. Res. Lett. 24*, 2007-2010, 1997b.

Tabazadeh, A., O.B. Toon, S.L. Clegg, and P. Hamill, A new parameterization of H_2SO_4/H_2O aerosol composition: Atmospheric implications, *Geophys. Res. Lett. 24,* 1931-1934, 1997c.

Tabazadeh, A., S.T. Martin, and J.S. Lin, The effect of particle size and nitric acid uptake on homogeneous freezing of sulfate aerosols, *Geophys. Res. Lett*. , submitted, 2000.

Taesler, I., R.G. Delaplane, and I. Olovsson, Hydrogen Bond Studies. XCIV. Diaquaoxonium Ion in Nitric Acid Trihydrate, *Acta Cryst. B 31*, 1489-1492, 1975.

Tie, X.X. G. P. Brasseur, C. Granier, A. De Rudder, N. Larsen, Model study of polar stratospheric clouds and their effects on stratospheric ozone: Part II -Model results, *J. Geophysical Research, 101*, 12575-12584, 1996.

Tie, X. X., C. Granier, W. Randel, and G.P. Brasseur, Effects of interannual variation of temperature on heterogeneous reactions and stratospheric ozone, *J. Geophys.Res. 102*, 23519-23527, 1997.

Toon, O.B., R.P. Turco, D. Westphal, R. Malone, and M.S. Liu, A multidimensional Model for Aerosols: Description of Computational Analogs, *J. Atmos. Sci. 45*, 2123-2143, 1988.

Toon, O.B., R.P. Turco, J. Jordan, J. Goodman, and G. Ferry, Physical Processes in Polar Stratospheric Ice Clouds, *J.Geophys. Res., 94*, 11359-11380, 1989.

Tourpali, K, X.X. Tie, C.S. Zerefos, and G. Brasseur, Decadal evolution of total ozone decline: Observations and model results, *J. Geophys.Res. 102*, 23955-23962, 1997.

Tsias, A., A.J. Prenni, K.S. Carslaw, T.P. Onasch, B.P. Luo, M.A. Tolbert, and T. Peter, Freezing of polar stratospheric clouds in orographically induced strong warming events, *Geophys. Res. Lett. 24*, 2303-2306, 1997.

Tsias, A., K.S Carslaw, T. Peter, M. Wirth, W. Renger, J. Biele, R. Neuber, H. Mehrtens, U. von Zahn, J. Reichardt, C. Wedekind, B. Stein, V. Santacesaria, L. Stefanutti, and J. Bacmeister, Aircraft6 lidar observations of an unusual PSC during APE-POLECAT, *J. Geophys. Res*, *104,* 23961-23969, 1999.

Turco, R.P., P. Hamill, O.B. Toon, R.C. Whitten, and C.S. Kiang, The NASA-Ames Research Center Stratospheric Aerosol Model, I. Physical Processes and Computational Analogs, *NASA Technical Paper 1362*, NASA, April 1979.

Turco, R.P., O.B. Toon, and P. Hamill, Heterogeneous Physicochemistry of the Polar Ozone Hole, *J.Geophys. Res.*, *94*, 16493-16510, 1989.

Waibel, A.E., Th. Peter, K.S. Carslaw, H. Oelhaf, G. Wetzel, P.J. Crutzen, U. Pöschl, A. Tsias, E. Reimer, and H. Fischer, Arctic ozone loss due to denitrification, *Science 283*, 2064-2069, 1999.

Warshawsky, M.S., M. Zondlo, and M.A. Tolbert, Impact of nitric acid on ice evaporation rates, *Geophys. Resl. Lett. 26,* 823-826, 1999.

Wirth, M., V. Weiβ, W. Renger, A. Dörnbrack, M. Leutbecher, H. Volkert, A. Tsias, K.S. Carslaw, and T. Peter, Model guided lagrangian observation and simulation of mountain polar stratospheric clouds, *J. Geophys. Res. 104*, 23971-23981, 1999.

Wofsy, S.C., R.J. Salawitch, J.H. Yatteau, M.B. McElroy, B.W. Gandrud, J.E. Dye, and D. Baumgardner, Condensation of HNO_3 on Falling Ice Particles: Mechanism for Denitrification of the Polar Stratosphere, *Geophys. Res. Lett. 17*, 449-452, 1990a.

Wofsy, S.C., G.P. Gobbi, R.J. Salawitch, and M.B. McElroy, Nucleation and Growth of HNO_3 Ÿ 3 H_2O Particles in the Polar Stratosphere, *J. Atmos. Sci.*, *47*, 2004-2012, 1990b.

World Meteorological Organization (WMO), *Scientific assessment of ozone depletion: 1994*, Rep. 37, Global Ozone Res. and Monit. Proj., Geneva, 1995.

World Meteorological Organization (WMO), *Scientific assessment of ozone depletion: 1998*, Rep. 44, Global Ozone Res. and Monit. Proj., Geneva, 1999.

Vaughan, G., D.P. Wareing, S.B. Jones, L. Thomas, N. Larsen: Lidar Measurements of Mt. Pinatubo Aerosols at Aberystwyth from August 1991 Through March 1992, *Geophys. Res. Lett. 21*, 1315-1318, 1994.

Zhang, R., M.-T. Leu, and M.J. Molina, Formation of polar stratospheric clouds on preactivated background aerosols, *Geophys. Res. Lett., 23*, 1669-1672, 1996.

Appendix.

Principal symbols and physical constants.

a_w	Water activity (relative humidity with respect to pure water)
A	Refractivity of solution
$A_{j,i}$	Volume corrected coagulation kernel
A_t	Total surface area density of particles in an ensemble (m^2/unit air mass)
B_{Ray}	Rayleigh volume backscattering coefficient
B	Total volume backscattering coefficient from particles
C	"Capacity" of particle (hexagonal particles), $C=C_c$ r
C_c	"Capacity" factor, $C_c=1$ for liquid particles, assumed $C_c=1.61$ for solid particles
C_m	Prefactor for nucleation rate
$C_{p,a}$	Specific (molar) heat capacity of air, $C_{p,a}=7/2$ R
D	Vapor diffusion coefficient
$d\sigma_b/d\Omega$	Differential backscatter cross section
$d\sigma/d\Omega_{Ray}$	Rayleigh differential scattering cross section
d	Molecular diameter
E	Aerosol extinction coefficient
e	Natural logarithm base (e≈2.7)
ΔF	Free energy for germ formation during nucleation by vapor deposition
ΔF_g	Free energy (per molecule) for ice germ formation
ΔF_{act}	Diffusion activation energy of water molecules across the ice/solution phase boundary (per molecule)
f	Particle volume ratio of adjacent bins, $f=V_{i+1}/V_i$
f_v	Ventilation factor for vapor diffusion
f_h	Ventilation factor for heat conduction
G_i	Average particle velocity in bin *i*, $(8kT/\pi m_i)^{1/2}$
g	Gravitational acceleration (9.8 ms^{-2})
h	Planck's constant (6.626176 10^{-34} J s)
J	Nucleation rate by vapor deposition
J_f	Nucleation rate by ice homogeneous freezing in supercooled liquid
$K_{j,i}$	Coagulation kernel
k	Boltzmann's constant (1.3800662 10^{-23} J K^{-1})
k_a	Thermal conductivity of air
L	Specific latent heat of sublimation
L_m	Molar latent heat of ice melting
M	Molar mass
M_a	Molar mass of air (28.9644 10^{-3} kg $mole^{-1}$)
M_n	Molar mass of nitric of HNO_3 (63.01 10^{-3} kg $mole^{-1}$)
M_s	Molar mass of nitric of H_2SO_4 (98.08 10^{-3} kg $mole^{-1}$)
M_w	Molar mass of H_2O (18.0153 10^{-3} kg $mole^{-1}$)
M	Compatibility (contact) nucleation parameter
m_i	Particle mass in bin *i*
m_R	Real part of refractive index
m_I	Imaginary part of refractive index

N	Number of particle size distribution bins
N_{Be}	Best (or Davies) number
N_c	number of water molecules in water (solution) in contact with a unit area of the ice surface ($5.85 \cdot 10^{18}$ m^{-2}),
N_{Re}	Reynolds number, ($U2r\rho_a/\eta$)
N_t	Total number density of particles in an ensemble, (#/unit air mass)
$N(>r_i)$	Integral particle distribution
$n(r_i)$	Differential particle distribution
n_i	Number density of particles in bin *i,* (#/unit air mass)
n	Molecular number density in gas phase, (P_p/kT)
n_{sat}	Molecular number density in gas phase at saturation, (P_{sat}/kT)
P_a	Air pressure
P_p	Partial pressure
P_{sat}	Saturation pressure over flat surface
$P_{sat,r}$	Saturation pressure over curved surface of radius r
Q_b	Mie backscatter efficiency factor
Q_e	Mie extinction efficiency factor
q	Latent heat of sublimation
R	Universal gas constant (8.31441 J $mole^{-1}$ K^{-1})
$\Re$	Backscatter ratio $(B_p+B_{Ray})/B_{Ray}$
r	Particle radius
r_i	Central particle radius in bin *i*
Δr_i	Particle radius bin width in bin *i*
r_g	Germ radius
r_m	Lognormal median (mode) radius of particles in an ensemble
S	Saturation ratio, P_p/P_{sat}
S_r	Saturation ratio over a curved surface of radius r, $P_p/P_{sat,r}$
T	Temperature
T_r	Temperature at surface of particle of radius r
T_f	Temperature for homogeneous freezing
T_0	Ice melting temperature (273.15 K)
t	Time
Δt	Integration time step size
U	Particle terminal fall velocity
V_i	Particle volume in bin *i*
ΛV_i	Particle volume bin width in bin *i*
V_i^u	Upper particle volume bin border in bin *i*
V_i^l	Lower particle volume bin border in bin *i*
W_i	Internal bin-volume in bin *i*
w_n	HNO_3 weight fraction
w_s	H_2SO_4 weight fraction
v	Mean thermal speed of molecules in gas phase, $(8RT/\pi M)^{1/2}$
w	Flux of molecules ($P_p v/4kT$)
X	Molar fraction in solution
A	Aspect ratio of solid particles, (ratio between length and diameter of particle)
α_d	Sticking coefficient
α_t	Thermal accommodation coefficient

γ	Number of moles in the condensed phase per particle
Θ	Correction factor for mean free path of condensing molecules, $\Lambda = \Theta\Lambda_a$
θ	Backscatter angle
η	Dynamic viscosity of air
κ	Dynamic shape factor of particles
Λ	Mean free path of condensing/evaporating molecules
Λ_a	Mean free path of air molecules
λ	Wavelength of light
μ	Mixing ratio
ν	Nucleation bin flow
φ	Condensation/evaporation bin flow
Ψ	Sedimentation bin flow
ω	Core return bin flow
ρ_p	Partial gas phase density of condensing molecules
ρ_{sat}	Saturation gas phase density of condensing molecules over flat surface
$\rho_{sat,r}$	Saturation gas phase density of condensing molecules over curved surface of radius r
ρ_a	Air density, (PM_a/RT)
ρ	Bulk condensed phase density
σ	Bulk surface tension of condensed phase
σ_e	Extinction cross section
ζ	Lognormal geometric standard deviation of particles in an ensemble
τ	Time constant of a microphysical process

Indices.

a	Air molecules
i (or *j*)	Geometric volume scale bin index, ($1 \le i \le N$), increasing with particle size
k	Layer index, increasing vertically downward
in	Ingoing bin flow
out	Outgoing bin flow
sol	liquid phase solution
n	Nitric acid molecules
s	Sulfuric acid molecules
w	Water molecules

Abbreviations.

NAT	Nitric acid trihydrate ($HNO_3 \cdot 3\ H_2O$)
ppbv	parts per billion by volume (10^{-9})
ppmv	parts per million by volume (10^{-6})
PSC	polar stratospheric cloud
SAT	sulfuric acid trihydrate ($H_2SO_4 \cdot 4\ H_2O$)
STS	supercooled ternary solution ($H_2SO_4/HNO_3/H_2O$)

DANISH METEOROLOGICAL INSTITUTE

Scientific Reports

Scientific reports from the Danish Meteorological Institute cover a variety of geophysical fields, i.e. meteorology (including climatology), oceanography, subjects on air and sea pollution, geomagnetism, solar-terrestrial physics, and physics of the middle and upper atmosphere.

Reports in the series within the last five years:

No. 95-1
Peter Stauning and T.J. Rosenberg: High-Latitude, day-time absorption spike events 1. morphology and occurrence statistics
Not published

No. 95-2
Niels Larsen: Modelling of changes in stratospheric ozone and other trace gases due to the emission changes : CEC Environment Program Contract No. EV5V-CT92-0079. Contribution to the final report

No. 95-3
Niels Larsen, Bjørn Knudsen, Paul Eriksen, Ib Steen Mikkelsen, Signe Bech Andersen and Torben Stockflet Jørgensen: Investigations of ozone, aerosols, and clouds in the arctic stratosphere : CEC Environment Program Contract No. EV5V-CT92-0074. Contribution to the final report

No. 95-4
Per Høeg and Stig Syndergaard: Study of the derivation of atmospheric properties using radio-occultation technique

No. 95-5
Xiao-Ding Yu, **Xiang-Yu Huang** and **Leif Laursen** and Erik Rasmussen: Application of the HIRLAM system in China: heavy rain forecast experiments in Yangtze River Region

No. 95-6
Bent Hansen Sass: A numerical forecasting system for the prediction of slippery roads

No. 95-7
Per Høeg: Proceeding of URSI International Conference, Working Group AFG1 Copenhagen, June 1995. Atmospheric research and applications using observations based on the GPS/GLONASS System. Not published

No. 95-8
Julie D. Pietrzak: A comparison of advection schemes for ocean modelling

No. 96-1
Poul Frich (co-ordinator), H. Alexandersson, J. Ashcroft, B. Dahlström, G.R. Demarée, A. Drebs, A.F.V. van Engelen, E.J. Førland, I. Hanssen-Bauer, R. Heino, T. Jónsson, K. Jonasson, L. Keegan, P.Ø. Nordli, **T. Schmith**, **P. Steffensen**, H. Tuomenvirta, O.E. Tveito: North Atlantic Climatological Dataset (NACD Version 1) - Final report

No. 96-2
Georg Kjærgaard Andreasen: Daily response of high-latitude current systems to solar wind variations: application of robust multiple regression. Methods on Godhavn magnetometer data

No. 96-3
Jacob Woge Nielsen, Karsten Bolding Kristensen, Lonny Hansen: Extreme sea level highs: a statistical tide gauge data study

No. 96-4
Jens Hesselbjerg Christensen, Ole Bøssing Christensen, Philippe Lopez, Erik van Meijgaard, Michael Botzet: The HIRLAM4 Regional Atmospheric Climate Model

No. 96-5
Xiang-Yu Huang: Horizontal diffusion and filtering in a mesoscale numerical weather prediction model

No. 96-6
Henrik Svensmark and Eigil Friis-Christensen: Variation of cosmic ray flux and global cloud coverage - a missing link in solar-climate relationships

No. 96-7
Jens Havskov Sørensen and Christian Ødum Jensen: A computer system for the management of epidemiological data and prediction of risk and economic consequences during outbreaks of foot-and-mouth disease. CEC AIR Programme. Contract No. AIR3 - CT92-0652

No. 96-8
Jens Havskov Sørensen: Quasi-automatic of input for LINCOM and RIMPUFF, and output conversion. CEC AIR Programme. Contract No. AIR3 - CT92-0652

No. 96-9
Rashpal S. Gill and Hans H. Valeur:
Evaluation of the radarsat imagery for the operational mapping of sea ice around Greenland

No. 96-10
Jens Hesselbjerg Christensen, Bennert Machenhauer, Richard G. Jones, Christoph Schär, Paolo Michele Ruti, Manuel Castro and Guido Visconti: Validation of present-day regional climate simulations over Europe: LAM simulations with observed boundary conditions

No. 96-11
Niels Larsen, Bjørn Knudsen, Paul Eriksen, Ib Steen Mikkelsen, Signe Bech Andersen and Torben Stockflet Jørgensen: European Stratospheric Monitoring Stations in the Arctic: An European contribution to the Network for Detection of Stratospheric Change (NDSC): CEC Environment Programme Contract EV5V-CT93-0333: DMI contribution to the final report

No. 96-12
Niels Larsen: Effects of heterogeneous chemistry on the composition of the stratosphere: CEC Environment Programme Contract EV5V-CT93-0349: DMI contribution to the final report

No. 97-1
E. Friis-Christensen og C. Skøtt: Contributions from the International Science Team. The Ørsted Mission - a pre-launch compendium

No. 97-2
Alix Rasmussen, Sissi Kiilsholm, Jens Havskov Sørensen, Ib Steen Mikkelsen: Analysis of tropospheric ozone measurements in Greenland: Contract No. EV5V-CT93-0318 (DG 12 DTEE): DMI's contribution to CEC Final Report Arctic tropospheric Ozone Chemistry ARCTOC

No. 97-3
Peter Thejll: A search for effects of external events on terrestrial atmospheric pressure: cosmic rays

No. 97-4
Peter Thejll: A search for effects of external events on terrestrial atmospheric pressure: sector boundary crossings

No. 97-5
Knud Lassen: Twentieth century retreat of sea-ice in the Greenland Sea

No. 98-1
Niels Woetman Nielsen, Bjarne Amstrup, Jess U. Jørgensen: HIRLAM 2.5 parallel tests at DMI: sensitivity to type of schemes for turbulence, moist processes and advection

No. 98-2
Per Høeg, Georg Bergeton Larsen, Hans-Henrik Benzon, Stig Syndergaard, Mette Dahl Mortensen: The GPSOS project
Algorithm functional design and analysis of ionosphere, stratosphere and troposphere observations

No. 98-3
Mette Dahl Mortensen, Per Høeg: Satellite atmosphere profiling retrieval in a non-linear troposphere. Previously entitled: Limitations induced by Multipath

No. 98-4
Mette Dahl Mortensen, Per Høeg: Resolution properties in atmospheric profiling with GPS

No. 98-5
R.S. Gill and M. K. Rosengren
Evaluation of the Radarsat imagery for the operational mapping of sea ice around Greenland in 1997

No. 98-6
R.S. Gill, H.H. Valeur, P. Nielsen and K.Q. Hansen: Using ERS SAR images in the operational mapping of sea ice in the Greenland waters: final report for ESA-ESRIN's: pilot projekt no. PP2.PP2.DK2 and 2nd announcement of opportunity for the exploitation of ERS data projekt No. AO2..DK 102

No. 98-7
Per Høeg et al.: GPS Atmosphere profiling methods and error assessments

No. 98-8
H. Svensmark, N. Woetmann Nielsen and A.M. Sempreviva: Large scale soft and hard turbulent states of the atmosphere

No. 98-9
Philippe Lopez, Eigil Kaas and Annette Guldberg: The full particle-in-cell advection scheme in spherical geometry

No. 98-10
H. Svensmark: Influence of cosmic rays on earth's climate

No. 98-11
Peter Thejll and Henrik Svensmark: Notes on the method of normalized multivariate regression

No. 98-12
K. Lassen: Extent of sea ice in the Greenland Sea 1877-1997: an extension of DMI Scientific Report 97-5

No. 98-13
Niels Larsen, Alberto Adriani and Guido DiDonfrancesco: Microphysical analysis of polar stratospheric clouds observed by lidar at McMurdo, Antarctica

No.98-14
Mette Dahl Mortensen: The back-propagation method for inversion of radio occultation data

No. 98-15
Xiang-Yu Huang: Variational analysis using spatial filters

No. 99-1
Henrik Feddersen: Project on prediction of climate variations on seasonel to interannual timescales (PROVOST) EU contract ENVA4-CT95-0109: DMI contribution to the final report:Statistical analysis and post-processing of uncoupled PROVOST simulations

No. 99-2
Wilhelm May: A time-slice experiment with the ECHAM4 A-GCM at high resolution: the experimental design and the assessment of climate change as compared to a greenhouse gas experiment with ECHAM4/OPYC at low resolution

No. 99-3
Niels Larsen et al.: European stratospheric monitoring stations in the Arctic II: CEC Environment and Climate Programme Contract ENV4-CT95-0136. DMI Contributions to the project

No. 99-4
Alexander Baklanov: Parameterisation of the deposition processes and radioactive decay: a review and some preliminary results with the DERMA model

No. 99-5
Mette Dahl Mortensen: Non-linear high resolution inversion of radio occultation data

No. 99-6
Stig Syndergaard: Retrieval analysis and methodologies in atmospheric limb sounding using the GNSS radio occultation technique

No. 99-7
Jun She, Jacob Woge Nielsen: Operational wave forecasts over the Baltic and North Sea

No. 99-8
Henrik Feddersen: Monthly temperature forecasts for Denmark - statistical or dynamical?

No. 99-9
P. Thejll, K. Lassen: Solar forcing of the Northern hemisphere air temperature: new data

No. 99-10
Torben Stockflet Jørgensen, Aksel Walløe Hansen: Comment on "Variation of cosmic ray flux and global coverage - a missing link in solar-climate relationships" by Henrik Svensmark and Eigil Friis-Christensen

No. 99-11
Mette Dahl Meincke: Inversion methods for atmospheric profiling with GPS occultations

No. 99-12
Benzon, Hans-Henrik; Olsen, Laust: Simulations of current density measure-

ments with a Faraday Current Meter and a magnetometer

No. 00-01
Høeg, P.; Leppelmeier, G: ACE: Atmosphere Climate Experiment: proposers of the mission

No. 00-02
Høeg, P.: FACE-IT: Field-Aligned Current Experiment in the Ionosphere and Thermosphere

No. 00-03
Allan Gross: Surface ozone and tropospheric chemistry with applications to regional air quality modeling. PhD thesis

No. 00-04
Henrik Vedel: Conversion of WGS84 geometric heights to NWP model HIRLAM geopotential heights

No. 00-05
Jérôme Chenevez: Advection experiments with DMI-Hirlam-Tracer

No. 00-06
Niels Larsen: Polar stratospheric clouds micro-physical and optical models